Florian Brumbauer, BSc

Effects of Grain Refinement on the Degradation of Bioresorbable Mg-Ca-Zn Alloy studied by Positron Annihilation and Impedance Spectroscopy

MASTER'S THESIS

to achieve the university degree of

Diplom-Ingenieur

Master's degree programme: Technical Physics

submitted to

Graz University of Technology

Supervisor

Univ.-Prof. Dipl.-Phys. Dr.rer.nat. Roland Würschum

Co-Supervisor

Dipl.-Ing. Dr.techn. Eva-Maria Steyskal

Institute of Materials Physics

Graz, September 2020

Affidavit

I declare that I have authored this thesis independently, that I have not used other than the declared sources/resources, and that I have explicitly indicated all material which has been quoted either literally or by content from the sources used. The text document uploaded to TUGRAZonline is identical to the present master‘s thesis.

Date

Signature

Abstract

Modern traumatology and orthopaedics demand for tailored biomedical implants which support osteogenesis and effectively reduce the risk of complications for patients of all ages. Magnesium alloys have gained increasing attention in the research field of bio-inert implant materials due to their excellent biocompatibility and elastic moduli close to human bone. Their low corrosion resistance and mechanical strength are urgent issues limiting their application in today's surgery, which both can be influenced by grain refinement. Therefore, monitoring the mechanical properties and degradation rates of the potential implant material is crucial in order to fulfill the demanded properties for a healthy bone healing process. In the present thesis, the complementary techniques of Positron Annihilation (PALS) and Electrochemical Impedance Spectroscopy (EIS) were used to study the effects of grain refinement on the degradation behaviour of a bioresorbable Mg-Ca-Zn alloy. Thereby, the positron lifetime in the alloy is sensitive to open-volume defects in the material developing during corrosion in physiological environments. On the contrary, electrochemical impedance spectra give detailed insight in the predominant reactions occurring at the alloy surface and the forming corrosion product layers.

The studied as-received Mg-based alloy (Mg-0.45 wt%Zn-0.45 wt%Ca, ZX00) was prepared by indirect extrusion and its fine-grained counterpart by subsequent high pressure torsion (HPT). The immersion tests in Simulated Body Fluid (SBF) indicated that the HPT-deformation of the Mg-based alloy highly weakened the corrosion resistance, resulting in a high corrosion damage. The preferential dissolution of the present intermetallic Mg_2Ca phase as well as the dissolution at susceptible grain boundaries introduced at a high density caused the formation of local deep pits during the first hours of immersion. The formed corrosion product bilayer, consisting of MgO and $Mg(OH)_2$, progressively disrupted and peeled off the alloy surface. These uncovered areas together with the severe corrosion pits probably acted as quick paths for hydrogen to diffuse into the alloy, forming MgH_2. The weakened corrosion resistance is associated with an unstable and permeable corrosion product bilayer, which insufficiently protected the underlying Mg-based alloy surface. In the later stages of immersion, a hydroxyapatite (HA) layer presumably coated most of the alloy surface. The more stable HA layer probably reduced the peeling off effects, which increased the corrosion resistance and slowed down the dissolution activity of the HPT-deformed

Mg-based alloy.

These results show that the combination of the complementary techniques of PALS and EIS is a very powerful tool for the investigation of the complex corrosion behaviour of Mg-based alloys. Insights in the progressing defect structure and the predominate surface reactions during corrosion could provide a versatile base for the development of tailored bioresorbable Mg-based implants.

Kurzfassung

Die moderne Traumatologie und Orthopädie benötigen maßgeschneiderte biomedizinische Implantate, welche die Osteogenese fördern und gleichzeitig effektiv das Risiko für Komplikationen für Patienten allen Alters reduzieren. Magnesiumlegierungen haben im Forschungsfeld der bioinerten Implantatmaterialien, aufgrund ihrer exzellenten Biokompatibilität und ihrem Elastizitätsmodul ähnlich dem des Knochens, zunehmend an Beachtung gewonnen. Ihr geringer Korrosionswiderstand als auch ihre geringe Festigkeit stellen wesentliche Probleme dar, welche den bisherigen Einsatz in der heutigen Chirurgie bisweilen verhinderten.Der Korrosionswiderstand als auch die Festigkeit können durch Kornfeinung beeinflusst werden. Deshalb ist es unumgänglich, die mechanischen Eigenschaften und das Auflösungsverhalten der potenziellen Implantatmaterialien genauestens zu überwachen, um die benötigten Anforderungen für einen gesunden Knochenheilungsprozess bestmöglich zu erfüllen. Im Rahmen dieser Arbeit wird der Einfluss der Kornfeinung auf das Auflösungsverhalten einer bioresorbierbaren Mg-Ca-Zn-Legierung mithilfe der komplementären Methoden der Positronenlebensdauer- (PALS) und der elektrochemischen Impendanzspektroskopie (EIS) untersucht. Dabei ist die Positronenlebensdauer sehr sensitiv für freie Volumen im Material, die sich während der Korrosion in physiologischen Umgebungen ausbilden. Die elektrochemischen Impedanzspektren hingegen geben einen detaillierten Einblick sowohl in die vorherrschenden Reaktionen, welche auf der Legierungsoberfläche ablaufen, als auch in die sich ausbildenden Korrosionsschichten.

Der Ausgangszustand der untersuchten Mg-Legierung (Mg-0.45 wt%Zn-0.45 wt%Ca, ZX00) wurde durch indirekte Extrusion und ihr feinkörniges Pendant durch anschließende Hochdruck-Torsion (HPT) hergestellt. Die Immersionsversuche in simulierter Körperflüssigkeit (SBF) zeigten, dass sich der Korrosionswiderstand durch die HPT-Verformung der Mg-Legierung sehr deutlich verringerte und zu einem hohen Korrosionsschaden führte. Die bevorzugte Auflösung sowohl der auftretenden intermetallischen Mg_2Ca Phase als auch an den in hoher Dichte eingebrachten anfälligen Korngrenzen führte zur lokalen Ausbildung von tiefen Löchern während der ersten Stunden des Eintauchens. Die ausgebildete Korrosionsdoppelschicht, bestehend aus MgO und $Mg(OH)_2$, brach mit zunehmender Eintauchzeit vermehrt auf und löste sich dabei von der Oberfläche. Diese freigelegten Regionen bildeten womöglich, zusammen mit den tiefen

Korrosionslöchern, schnelle Wege für den Wasserstoff in die Mg-Legierung, was zur Ausbildung von MgH_2 führte. Der verringerte Korrosionswiderstand der HPT-verformten Mg-Legierung ist verbunden mit einer instabilen und durchlässigen Korrosionsdoppelschicht, welche die darunterliegende
Oberfläche der Mg-Legierung nur unzureichend schützte. In der späteren Phase der Korrosion wurde die Legierungsoberfläche vermutlich mit einer Schicht aus Hydroxyapatite (HA) bedeckt. Die stabilere HA-Schicht reduzierte mutmaßlich die Ablösungseffekte, was zu einer Erhöhung des Korrosionswiderstandes führte und die Auflösungsaktivität der HPT-verformten Mg-Legierung verlangsamte.

Diese Ergebnisse zeigen, dass die Kombination der komplementären Methoden der PALS und der EIS ein sehr leistungsfähiges Werkzeug zur Untersuchung des komplexen Korrosionsverhaltens von Mg-basierten Legierungen ist. Einblicke in die gebildete Defektstruktur und in die vorherrschenden Oberflächenreaktionen könnten eine vielseitige Basis für die Entwicklung von maßgeschneiderten, bioresorbierbaren auf Mg-basierten Implantaten darstellen.

Abbreviations and physical quantities

AHE	Anodic hydrogen evolution
CE	Counter electrode
CHE	Cathodic hydrogen evolution
CPE	Constant phase element
EC1	Equivalent Circuit 1
EC2	Equivalent Circuit 2
EIS	Electrochemical Impedance Spectroscopy
EL	Electrolyte
HA	Hydroxyapatite
HPT	High-pressure torsion
NDE	Negative difference effect
NHE	Normal hydrogen evolution
OCP	Open circuit potential
PALS	Positron Annihilation Lifetime Spectroscopy
RE	Reference electrode
SBF	Simulated body fluid
SHE	Standard hydrogen evolution
WE	Working electrode

$\boldsymbol{A}$	Area of the sample
$\boldsymbol{\alpha}$	Specific positron trapping rate
$\boldsymbol{C_{dl}}$	Double layer capacity
$\boldsymbol{C_{l}}$	Overall corrosion product layer capacity

$\boldsymbol{C_{l,1}}$	MgO layer capacity
$\boldsymbol{C_{l,2}}$	$Mg(OH)_2$ layer capacity
$\boldsymbol{C_2}$	Capacity associated with a diffusional impedance for a stagnant or convective diffusion layer (coupled to R_2)
$\boldsymbol{D}$	Positron bulk diffusivity
$\boldsymbol{d_i}$	Thickness of the corrosion product bilayer on sample i ($i = 1, 2$)
$\boldsymbol{d_{mean}}$	Mean thickness of the corrosion product bilayer on sample pair
$\boldsymbol{d_{MgO}}$	MgO layer thickness
$\boldsymbol{d_{Mg(OH)_2}}$	$Mg(OH)_2$ layer thickness
$\boldsymbol{E_{pt}}$	Pitting potential
$\boldsymbol{\epsilon}$	Dielectric constant of the MgO layer
$\boldsymbol{f}$	Frequency
$\boldsymbol{I_b}$	Positron annihilation intensity at grain boundaries
$\boldsymbol{I_{d_i}}$	Fraction of positrons annihilating in the surface bilayer (thickness d_i) on sample i ($i = 1, 2$)
$\boldsymbol{I_i}$	Positron annihilation intensity associated with positron lifetime component i ($i = 1 - 3$)
$\boldsymbol{I_{d_{mean}}}$	Mean fraction of positrons annihilating in the surface bilayer (thickness d_{mean}) on sample pair
$\boldsymbol{I_t}$	Positron annihilation intensity at the precipitate/matrix interface
$\boldsymbol{\kappa}$	Coating conductivity of the $Mg(OH)_2$ layer
$\boldsymbol{L}$	Inductance associated with relaxation processes at the surface (coupled to R_3)
$\boldsymbol{m_i}$	Mass of sample i ($i = 1, 2$)
$\boldsymbol{m_{ges}}$	Total mass of sample pair
$\boldsymbol{m_{Mg}}$	Mass of the magnesium matrix

$\boldsymbol{m_{Mg(OH)_2}}$	Mass of the $Mg(OH)_2$ layer
$\boldsymbol{m_0}$	Initial mass of the sample used in the approximation
$\boldsymbol{M_{Mg}}$	Molar mass of magnesium
$\boldsymbol{M_H}$	Molar mass of hydrogen
$\boldsymbol{M_O}$	Molar mass of oxygen
$\boldsymbol{n_{C_{dl}}}$	Parameter associated with the constant phase element describing the deviation from the ideal capacitive behaviour of C_{dl}
$\boldsymbol{n_L}$	Parameter associated with the constant phase element describing the deviation from the ideal inductive behaviour of L
$\boldsymbol{\phi}$	Bode phase of the impedance
$\boldsymbol{r}$	Radius of spherical grains
$\boldsymbol{R}$	Average spacing between spherical Mg_2Ca particles
$\boldsymbol{r_0}$	Radius of the spherical Mg_2Ca particles
$\boldsymbol{R_A}$	Zero-frequency resistance associated with anodic corrosion behaviour
$\boldsymbol{R_C}$	Zero-frequency resistance associated with cathodic corrosion behaviour
$\boldsymbol{R_e}$	Electrolyte resistance
$\boldsymbol{R_{l,1}}$	Electrolyte resistance in the pores of the MgO layer
$\boldsymbol{R_{l,2}}$	Electrolyte resistance in the pores of the $Mg(OH)_2$ layer
$\boldsymbol{R_{ZF}}$	Zero-frequency resistance associated with overall corrosion behaviour
$\boldsymbol{R_1}$	Charge transfer resistance
$\boldsymbol{R_2}$	Resistance associated with a diffusional impedance for a stagnant or convective diffusion layer (coupled to C_2)
$\boldsymbol{R_3}$	Resistance associated with relaxation processes at the surface (coupled to L)
$\boldsymbol{\rho_{Mg(OH)_2}}$	Density of $Mg(OH)_2$
$\boldsymbol{\tau_f}$	Bulk (free) positron lifetime

$\boldsymbol{\tau_i}$	Positron annihilation lifetime component i ($i = 1 - 3$)
$\boldsymbol{\tau_t}$	Positron lifetime in open-volume defect (voids)
$\boldsymbol{\tau_{mean}, \tau_m}$	Mean positron annihilation lifetime
$\boldsymbol{V_{Mg(OH)_2}}$	Volume of the $Mg(OH)_2$ layer
$\boldsymbol{x_i}$	Number of moles of corroded magnesium
$\boldsymbol{x_{PB}}$	Pilling-Bedworth ratio of MgO
$\boldsymbol{Y_{C_{dl}}}$	Parameter associated with the constant phase element (numerical value of the admittance) replacing C_{dl}
$\boldsymbol{Y_L}$	Parameter associated with the constant phase element (numerical value of the admittance) replacing L
$\boldsymbol{Z_F}$	Faradaic impedance
$\boldsymbol{Z'}$	Real part of the electrochemical impedance
$\boldsymbol{Z''}$	Imaginary part of the electrochemical impedance

Contents

1 Introduction 1

2 Fundamentals 5

2.1 Fundamentals of Electrochemistry . . . 5

2.2 Electrochemical corrosion mechanisms of magnesium and its alloys . . . 7

2.3 Electrochemical Impedance Spectroscopy (EIS) . . . 23

2.4 Positron Annihilation Lifetime Spectroscopy (PALS) . . . 31

3 Experimental 43

3.1 Materials: MgCaZn alloys . . . 43

3.2 PALS for ex-situ corrosion measurements . . . 43

3.3 EIS for in-situ corrosion measurements . . . 45

4 Results 49

4.1 PALS on as-received Mg-alloy . . . 49

4.2 PALS on HPT-deformed Mg-alloy . . . 58

4.3 EIS on as-received Mg-alloy . . . 69

4.4 EIS on HPT-deformed Mg-alloy . . . 82

5 Discussion 95

5.1 Development of structural defects . . . 95

5.2 Predominant surface reactions . . . 103

6 Conclusion 111

1 Introduction

Biomedical implants play a crucial role in society, since osteosynthesis is the procedure of choice for bone fracture treatment in orthopedics.[1,2] To date, the most widely used implant materials for fracture fixation are based on titanium or stainless steel due to their high strength, durability (wear resistance), and their complete acceptance by the human body termed as biocompatibility.[1,3] However, these permanent bio-inert metallic implants encounter significant problems for the patient such as the risk for local inflammatory reactions, infections due to bacterial biofilms, stress concentrations leading to cracks, and stress shielding accompanied by bone instability and/or loss.[1–3] According to Wolff‘s law, load is mostly taken by the implant, since it exhibits larger elastic moduli compared to the human bone and, consequently, the bone reduces its density due to reduced bone remodelling.[3,4] Subsequently, the risk for re-fractures increases.[2] In younger patients, the permanent implants are not able to integrate with the bone during growth, and the removal of the implant is inevitably in order to avoid the risk of irritations in the bone growth.[1,2] In elderly patients, osteoporosis increases the risk of bone fractures and complicates the subsequent fixation of the damaged bone.[5–7] Bacterial films formed during the surgery represent a particular threat for the elderly patients with suppressed immunity.[8] The described physiological and material physics aspects underline the demand for tailored biomedical implants.

The ideal biomedical implant should be resorbable, restore the bone by transferring load-bearing capacity to the bone, and induce or support fracture healing.[2,3] Thus, as shown in Fig. 1, the yield stress (volume) of the ideal bioresorbable implant should decrease linearly with implantation time and be completely degraded after 1-2 years. After the osteogenesis (bone healing) time of 16 weeks, the yield stress should be higher as, or at least equal, for the pure Ti-based implant.[9] This means, that the implant provides reliable fixation during the osteogenesis time and resorbs afterwards.[3]

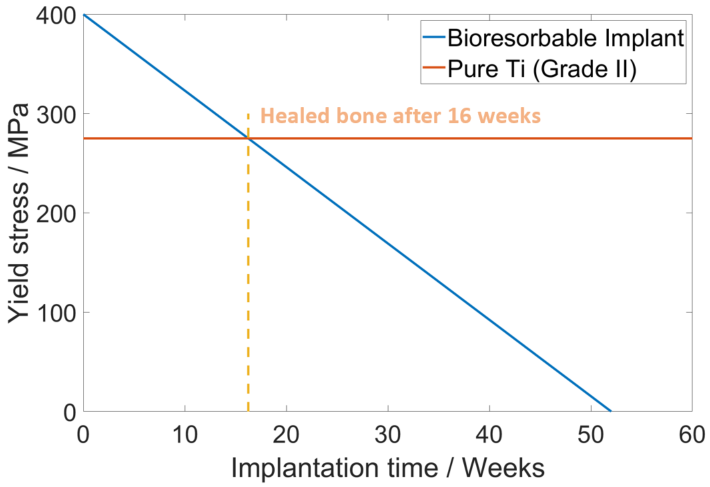

Figure 1: Yield stress of the ideal bioresorbable implant depending on implantation time. Redrawn after Ikeo et al.[9]

Magnesium (Mg) has been given particular attention for the use as bioresorbable material for bone fixation, since it is biocompatible, nontoxic and exhibits a low specific density as well as elastic moduli close to that of a human bone.[1,10] Magnesium is the fourth most abundant element in the human body, where most of it stored in the bones and excess concentrations can be easily excreted.[1,11,12] Additionally, the released Mg^{2+} during dissolution supports osteogenesis, which leads to a healthy bone near the implant/bone tissue interface.[13] However, pure magnesium exhibits a too low strength for load-bearing implants and rapidly dissolves in physiological environments (accompanied by loss of mechanical integrity).[3,11] The rapid dissolution of pure magnesium is accompanied by hydrogen-gas evolution.[2,3,11] The formed hydrogen can delay the healing process, cause necrosis of the surrounding tissue, or can lead to encapsulated gas cavities.[1,11]

To slow down the degradation rate and to strengthen the pure Mg biomedical implants, alloying as well as grain refinement by plastic deformation has been applied.[3] The potential alloying elements have to be carefully chosen, since biocompatibility and toxicity are major concerns. Thus, Mg-Ca- and Mg-Ca-Zn-alloys have turned out to be the most promising implant materials.[3,10] Calcium is as well a major component of the human bone, whereby Mg is essential for its incorporation into the bone. The release of Mg and Ca ions during degradation and the subsequent integration into the bone is expected to support osteogenesis. Calcium as alloying element additionally influences the microstructure, since it is beneficial for grain refinement. Zinc can be found in all human body tissues and is an essential trace element needed in the human body.[10] Apart from their good biocompatibility, the mechanical as well as the electrochemical behaviour of these Mg-Ca-Zn-alloys can be tuned by changing the Zn/Ca atomic ratio and/or by additional mechanical deformation and heat treatment.[3] The effects of alloying as well as plastic deformation (acceleration or retardation) are controversially discussed, since the corrosion performance of Mg-alloys is strongly dependent on the test conditions (e.g. temperature, electrolyte, surface/volume ratio)[1], and microstructural features (e.g. intermetallic particles)[14].

In the present work, the in-vitro corrosion performance of a bioresorbable Mg-0.45 wt%Zn-0.45 wt%Ca-alloy (ZX00) immersed in Simulated Body Fluid (SBF) is investigated and compared to its plastically deformed counterpart. For this purpose, Positron Annihilation Lifetime Spectroscopy (PALS) was applied, to obtain a deeper understanding of the influence of severe plastic deformation on the microstructure and on the development of the structural defects arising from corrosion. Since microstructure has a major impact on the corrosion resistance, Electrochemical Impedance Spectroscopy (EIS) was used in order to get an in-situ insight on predominant surface reactions occurring and the accompanied formation of corrosion products on the surface during corrosion. The results obtained from these complementary characterization techniques are then used to propose a fundamental dissolution model for the investigated Mg-alloy.

2 Fundamentals

2.1 Fundamentals of Electrochemistry

In electrochemistry, structures and processes at the interface of an (liquid) electrolyte and an immersed (solid metal) electrode are studied. Both adjoining phases not only differ considerably in their properties, but also represent a boundary between two different conduction mechanisms, namely electronic and ionic conduction.[15] In the electrolyte, charge is carried by dissolved ions with different signs, whereas in the metal electrode fixed ionic cores are surrounded by freely moving electrons.

After immersion, several alignments and reactions take place depending on the metal-solution system. Redox reactions, where charge is transferred through the phase boundary and current is flowing in order to reach the equilibrium, are called *electrochemical reactions.* In equilibrium the electrochemical potentials for both phases are equal and no current is flowing. These compensatory processes to engage an equilibrium involve metal deposition and metal dissolution. During metal deposition, a metal ion from the solution is discharged and deposited on the surface by taking up electrons from the metal surface, whereas during metal dissolution a metal atom is oxidized and detached from the surface into the electrolyte by giving up electrons. The interface between the immersed electrode and the electrolyte will be charged resulting from the excessive charge accumulation on the metal surface, which is compensated by the cations or anions in the electrolyte.[15,16] Depending on the electrochemical potentials μ_i of both phases, the metal surface will be positively ($\mu_{Electrode} < \mu_{Electrolyte}$) or negatively ($\mu_{Electrode} > \mu_{Electrolyte}$) charged and an electrochemical double layer resulting from the charge distribution will form until the dissolution or deposition is stopped by electrostatic restraining forces. Both will result in a potential difference influencing the electrochemical equilibrium condition.[16]

The potential difference between electrode and electrolyte is called *equilibrium Galvani potential* $\Delta\phi_0$ and is given by the Nernst equation

$$\Delta\phi_0 = \phi_{Me} - \phi_L = \Delta\phi_{00} + \frac{RT}{nF} \ln \frac{a_{ox}}{a_{red}} \ , \tag{1}$$

where $\Delta\phi_{00}$ is the standard Galvani potential difference, R the gas constant, T the temperature, n the number of electrons, F the Faraday constant, and a_{ox} and a_{red} are the activities of the oxidized and reduced species in the electrolyte, respectively. The Nernst equation describes the dependency of the equilibrium potential on the concentration of the electrolytic components since the activities a_i of the components can be approximated by the respective concentrations.[16] Since the equilibrium Galvani potential cannot be measured directly, but indeed a potential difference between two redox couples, the standard electrode potential of an electrochemical reaction is measured with respect to a well defined reference point. The electrochemical series is defined with respect to the standard hydrogen electrode (SHE) with the redox system

$$\mathrm{H_2 + H_2O \longleftrightarrow H_3O^+ + 2\,e^-} \ , \tag{2}$$

which is then associated with an arbitrary chosen potential of 0 V.[15–17]

Since metals are excellent conductors due to their high concentration of mobile charge carriers, the excess charge in the electrode is confined in a surface layer of approximately 1 Å. The electrolyte exhibits a much lower carrier concentration extending the excess charge in a more widely spread area of approximately 5 up to 20 Å with electrolyte concentrations of 0.1 - 1 M.[15] In the electrochemical double layer region, no charge is transferred across the interface and the electrode-electrolyte system can be considered as capacitor with a small electrode separation and the known linear relationship between potential and charge stored. This electrochemical double layer can be described with the simplified *Helmholtz model.* In the model, the electrode is considered to be coated with a rigid ionic layer, the *outer Helmholtz layer*, whereby the anions and cations, respectively, are not in contact with the metal electrode as they are separated by their solvation sheaths from the surface. Most of the electrochemical reactions, where charge is transferred across the interface, proceed with an intermediate adsorption step, where the ions have to break up their surrounding solvation sheaths to adsorb on specific sites at the metal surface. Usually, anions are more often specifically adsorbed and chemically held on metal surfaces since their solvation sheaths are less strongly bond due to their larger atomic radii. The resulting layer of adsorbed ions on the metal surface is then called the *inner Helmholtz layer.*[15,16]

Typically, electrochemical measurements are performed in a three-electrode configuration, consisting of an working electrode (WE), a reference electrode (RE), and a counter electrode (CE). The specimen to be measured is used and controlled as WE. As RE, the commercially available Ag/AgCl system in saturated KCl is often used (electrodes of second type). Without external manipulation, the potential between WE and RE is called open circuit potential (OCP). During measurements, it is often desired to adjust the potential other than OCP on the WE, which is usually referred to as polarization or overpotential. Therefore, a CE is needed to take up the flowing current since currents between WE and RE are unwanted (constant RE potential).[15]

2.2 Electrochemical corrosion mechanisms of magnesium and its alloys

This chapter is mainly based on the in-book article from Song[18], *Corrosion electrochemistry of magnesium (Mg) and its alloys* in *Corrosion of Magnesium Alloys*.

Magnesium offers unique physical and chemical properties attractive for various applications, especially in the medical field as biodegradable implant as described in 1. Its rapid corrosion in aqueous environments and the accompanied hydrogen evolution phenomena associated with the Mg dissolution are major drawbacks, which show the urge of a deeper understanding of the corrosion mechanisms in magnesium in order to develop prevention solutions and tailored Mg alloys.[19] In the following sections, the corrosion mechanisms of magnesium and the influence of alloying elements are described in detail.

Magnesium is thermodynamically very active and can corrode (oxidation process) in natural environments containing oxygen or water, spontaneously forming an oxide or hydroxide surface layer. This tendency is manifested by the more negative chemical potentials μ_0 of the formed magnesium compounds (Mg^{2+}, MgO or $Mg(OH)_2$) compared to the metallic magnesium.

At 25 °C magnesium exhibits a standard electrode potential of $-2.37\,V/SHE$ when in contact with its divalent ions in solution, which is the lowest standard potential compared to other engineering metals. The actual corrosion potential of Mg in chloride containing solutions is approximately $-1.7\,V/SHE$, due to the formation of a $Mg(OH)_2$ layer on the surface. The formed corrosion product layer provides some protection over a wide range of pH, as described by the Pourbaix diagram.[20,21] This potential-pH diagram describes the thermodynamics governing the film formation and can be used to estimate the stability of Mg immersed in water. Below a pH of approximately 10.5, Mg oxidizes into ions, oxides and hydroxides when immersed in water. At a high pH (> 10.5), the metallic Mg is most likely passivated by a formed $Mg(OH)_2$ layer. Unfortunately, a thermodynamic equilibrium for Mg immersed in an aqueous solution does not exist, since different reactions might occur concurrently depending on the surface state of the Mg.[18,20,21] The nature of the formed corrosion products on the surface affects the electrochemical behaviour of magnesium significantly and is influenced by various factors, since kinetics and detailed reaction steps play an essential role.

2.2.1 Surface film

Composition and Microstructure A surface film consisting of corrosion products will be formed on magnesium and its alloys during the corrosion process. This film will vary in composition and microstructure depending on the material composition, environment and formation conditions. In air, the film is mainly composed of MgO and is relatively thin and compact. The MgO film will additionally exhibit some amorphous charateristics allowing water to reach into the film. Moisture in the air will cause the formation of an additional hydrated layer, which is more porous and amorphous. CO_2 in air can also combine with moisture in air and form carbon compounds in the surface film. After magnesium is immersed in aqueous environments, the outer air-formed film will react with water and transform mainly into $Mg(OH)_2$. Chlorides or passivating reagents present in the solution can also be included into the resulting film. Oxides or hydroxides of the alloying elements may as well be incorporated into the surface film, whereby the contribution depends on the affinity for oxygen and hydroxyls, and the mobility within the surface film. The microstructure of the film most probably consists of multiple layers, as illustrated in Fig. 2. The morphology of the film is assumed to consist of a thin, compact MgO layer on the magnesium surface and an outer layer mainly consisting of $Mg(OH)_2$, which is thicker and more porous.

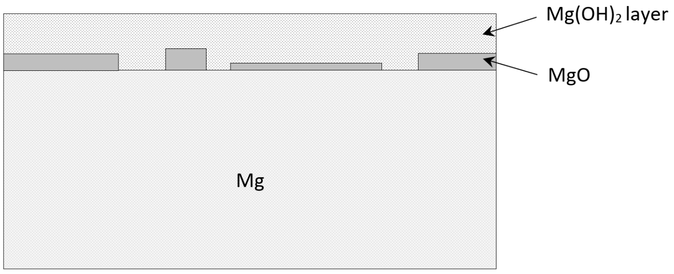

Figure 2: Platelet-like microstructure of surface film. Redrawn after Song[18].

Protectiveness The MgO film does not fully cover the surface, since the Pilling-Bedworth ratio (volume ratio of metal oxide to metal) of MgO/Mg is smaller than 1, namely 0.8. This means, that the MgO is not sufficient to protect the underlying magnesium. In aqueous solution, the main constituent of the corrosion product film is $Mg(OH)_2$, which exhibits a Pilling-Bedworth ratio higher than 1, but is still unstable in an acidic, neutral or weak alkaline solution and therefore, does not offer sufficient protection either. The limited protection stemming from the developing corrosion product film is one of the reasons for the weak corrosion resistance of magnesium and its alloys, but also the kinetics of film formation and dissolution are crucial for the corrosion performance. The transformation of the air-formed MgO to $Mg(OH)_2$ on the surface, when immersed in aqueous environments, can take place either by direct hydration of magnesium or by dissolution of MgO on the surface. When the hydration takes place immediately after immersion, the cubic MgO lattice is converted into a hexagonal $Mg(OH)_2$ and can lead to a disruption of the surface film since the volume of the hexagonal $Mg(OH)_2$ is twice as high as the cubic MgO lattice. When MgO or the metallic magnesium is dissolved, $Mg(OH)_2$ will deposit loosely on the surface and the discontinuous MgO may be also converted or dissolved into porous $Mg(OH)_2$. This discontinuities in the corrosion product film are the sites, where corrosion of the underlying magnesium is initiated and which have a direct effect on the reactions on the surface. In the disrupted regions, local corrosion is initiated resulting in the formation of loose $Mg(OH)_2$ on the surface. The generated hydrogen in the corroding area may break up the deposited $Mg(OH)_2$, preventing the corroded area from passivating, which may hinder the self-inhibition of the local corrosion regions. If there are passivating reagents like fluorides and phosphates present in the solution, they can react with magnesium forming a very thin, nearly insoluble surface film, which effectively protects the magnesium.

The stability of magnesium in natural environments and the formed surface film crucially influence the occurring reactions. In the following, possible anodic and cathodic processes and reactions taking place on the immersed magnesium or magnesium alloy will be described.

2.2.2 Anodic process

The anodic process on magnesium exhibits an unique behaviour, which is closely related to the anodic hydrogen evolution (AHE) and the onset of localized corrosion. After introducing these effects, a dissolution model will be used in order to describe the anodic process on magnesium.

Negative Difference Effect (NDE) The negative difference effect is an unusual hydrogen evolution phenomenon that occurs in magnesium and its alloys at polarization potentials more positive than a certain potential. For most metals, a more positive polarization potential increases the anodic dissolution rate and concurrently decreases the cathodic hydrogen evolution (CHE), which means an accelerated anodic reaction and a decelerated cathodic reaction. In magnesium, the hydrogen evolution rate to some extent increases drastically for an anodic increase in applied potential. This unusual hydrogen evolution can set in already at a cathodic potential, meaning that the NDE is not strictly an anodic polarization phenomena, but can also start at cathodic polarization in some electrochemical systems of magnesium and its alloys. This unusual anodic hydrogen evolution (AHE) is illustrated in Fig. 3. The hydrogen evolution decreases (cathodic hydrogen evolution H_2^c) for negative polarization potentials approaching the corrosion potential, and suddenly increases as the polarization potential changes from negative to positive at the E_{pt} (anodic hydrogen evolution H_2^a), meaning that in magnesium there are two hydrogen evolution processes taking place other than for other common metals (only H_2^c). The cathodic hydrogen evolution still has an equilibrium potential much more positive than the corrosion potential of magnesium. Therefore, the normal hydrogen evolution is still strongly cathodically polarized in the anodic region (more positive than E_{pt}) and likely to take place, whereby the cathodic hydrogen evolution (CHE) rate decreases with increasing potential, as shown in Fig. 3 (along H_2^c).

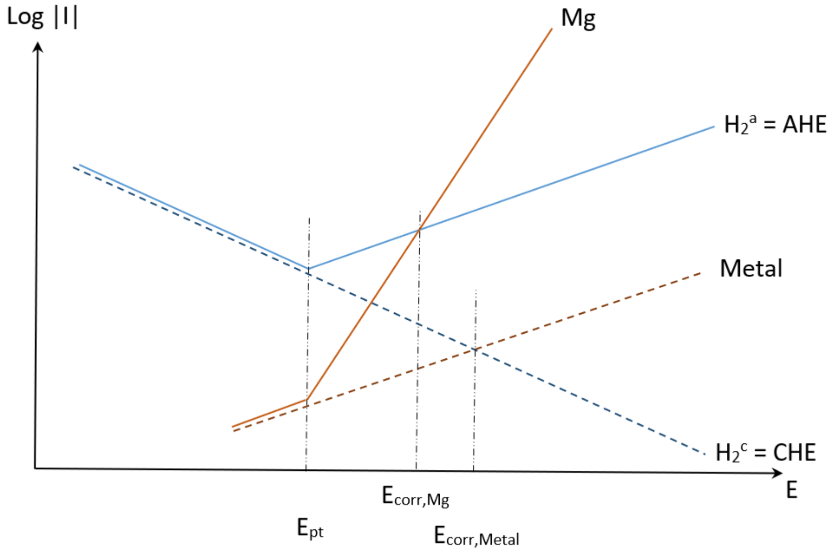

Figure 3: Dissolution and hydrogen evolution in magnesium compared to other common metal. Redrawn after Song[18].

The CHE mainly takes place at non-corroded areas of the magnesium or magnesium alloy, whereas the anodic dissolution of magnesium and its alloys is related to the anodic hydrogen evolution (AHE) from corroding areas. Both CHE and AHE are responsible for the cathodic and anodic polarization response of the magnesium or magnesium alloy.

Lower apparent valence and low anodic dissolution efficiency During the dissolution of Mg, electrons are generated resulting in a current proportional to the number of generated electrons n. The anodic dissolution of Mg is a two (Mg^{2+}, $n = 2$) or single Mg^{+} ($n = 1$) electron transfer electrochemical reaction. If the AHE is assumed to be an electrochemical process involving Mg^{+} ($n = 1$), it will consume electrons generated from the anodic dissolution of magnesium and the apparent number of electrons n contributing to the current will decrease to a value lower than two. Apparently, n lies between 1.26 and 1.90 in many electrolytes, which reduces the anodic dissolution efficiency (down to 60 % dependent on the electrolyte solution). This means, that only a fraction of the electrons generated during the dissolution of magnesium contribute to the current, and the remaining electrons are consumed in further processes involved in the dissolution.

Low anodic polarization resistance and passivity If the AHE from corroding areas is a normal hydrogen evolution process, it will consume current from the anodic dissolution and thereby reduce the theoretically expected anodic current density. Here in contrast, the anodic current densities dramatically increase with increasing anodic polarization. This onset of the increase of anodic current density can be assigned to E_{pt}, the pitting potential, and is associated with an increase of dissolution in local areas and a sudden increase of hydrogen evolution due to the NHE. Since E_{pt} is usually more negative than the corrosion potential E_{corr} of magnesium and its alloys, the measured anodic polarization curves already describe an intense pitting process taking place at the surface. Therefore, the drastic increase in anodic current density with potential usually exhibits a low anodic polarization resistance. The potential region between E_{pt} and E_{corr} exhibits a relatively high polarization resistance and is regarded as "passive" region, but only shows a tendency to passivity since the anodic processes are insufficiently retarded by the corrosion product film. The width of the region strongly depends on the alloying elements (passivating elements) and environmental conditions (pH). Surface films, as mentioned above, strongly influence the passivity of magnesium and its alloys, and the compactness and stability of the film determines the AHE process to a greater extent.

Anodic dissolution model The unique anodic polarization behaviour of magnesium described above is strongly related to the AHE process and to the onset of localized corrosion. The normal anodic dissolution of magnesium in aqueous environments can be described as

$$\mathrm{Mg} \longrightarrow \mathrm{Mg}^{2+} + 2\,\mathrm{e}^{-} \tag{3}$$

and most likely involves intermediate steps involving mono-valence Mg

$$\mathrm{Mg} \longrightarrow \mathrm{Mg}^{+} + \mathrm{e}^{-}\ , \tag{4}$$

whereas Mg^{+} is unstable and rapidly transforms to the more stable Mg^{2+} in three possible steps: Further anodic oxidation, a disproportionation reaction or direct hydration.

Immediately on the surface, Mg^{+} can be directly anodized into Mg^{2+}

$$Mg^{+} \longrightarrow Mg^{2+} + e^{-} \tag{5}$$

and the overall reaction is again Eq. (3), i.e., the normal anodic dissolution reaction.

In the disproportionation reaction, due to the high instability in solution, Mg^{+} may transform into other intermediates.

$$2\,Mg^{+} \longrightarrow Mg + Mg^{2+} \longrightarrow Mg \cdot Mg^{2+}\ . \tag{6}$$

The generated intermediate may stay on the surface as fine particles which are more active than the magnesium surface. The intermediates will further react in neutral or alkaline solution as

$$Mg \cdot Mg^{2+} + 2\,H_2O \longrightarrow 2\,Mg(OH)_2 + Mg^{2+} + H_2\ . \tag{7}$$

The overall anodic reaction in neutral or alkaline solution will be

$$Mg + H_2O \longrightarrow \frac{1}{2}Mg(OH)_2 + \frac{1}{2}Mg^{2+} + \frac{1}{2}H_2 + e^{-}\ . \tag{8}$$

Mg^{+} can also react with water in neutral or alkaline solution generating hydrogen

$$2\,Mg^{+} + H_2O \longrightarrow {}_2OH^{-} + 2\,Mg^{2+} + H_2 \tag{9}$$

with an overall anodic dissolution reaction as

$$Mg + H_2O \longrightarrow OH^{-} + Mg^{2+} + \frac{1}{2}H_2 + e^{-}\ . \tag{10}$$

The processes stated above will only take place at film-free areas on the bare magnesium, since Mg^+ is unlikely to survive at coated areas. The further anodic oxidation does not produce hydrogen, whereas both the disproportionation reaction and the direct hydration lead to hydrogen evolution with the same overall anodic dissolution reaction. The processes described above are illustrated schematically in Fig. 4.

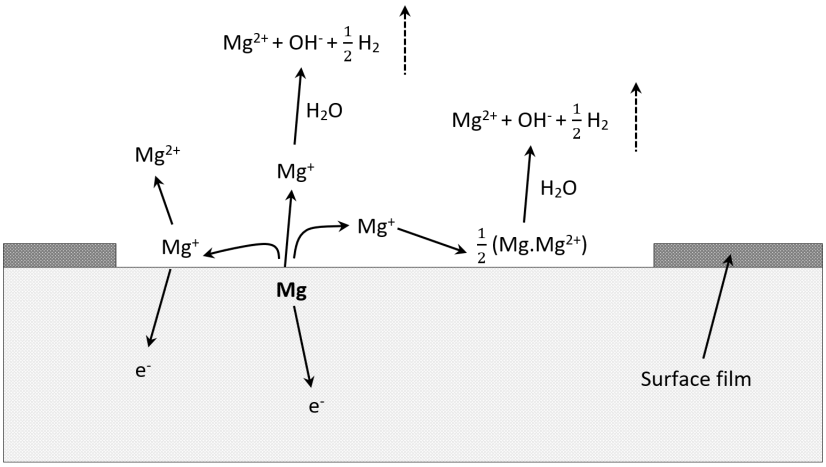

Figure 4: Anodic dissolution processes. Redrawn after Song[18].

The total anodic dissolution can be written as

$$Mg + [1/(1+y)]H_2O \longrightarrow Mg^{2+} + [1/(1+y)]OH^- + [1/(2+2y)]H_2 + [(1+2y)/(1+y)]e^- \quad (11)$$

in neutral or alkaline solution, where y is the ratio of dissolution reaction and hydrogen evolution reactions.

The anodic hydrogen evolution is a process that occurs under various conditions of potential polarization and is not limited to the corrosion potential. As the NDE occurs at potentials more positive than the pitting potential, the surface film breakdown at E_{pt} plays an important role in the corrosion process. The area of film-free sites is potential dependent and increases for more positive polarization potentials. For potentials more negative than E_{pt}, the surface is fully covered and to some extent protected by the film. Therefore, the anodic dissolution reactions are negligible. For increasing potential more positive than E_{pt}, the film is disrupted in some areas and the dissolution reactions become dominant accompanied with a sudden increase in the anodic dissolution current and hydrogen evolution. The anodic oxidation of Mg^+ is a potential-dependent process, which accelerates at more positive polarization potential and increases the dissolution efficiency, as the number of electrons n contributing to the faradaic current reaches nearly two. This means, that the dissolution dominates the hydrogen evolution processes. The low anodic polarization resistance is caused by the film breakdown around E_{pt}. As the surface exhibits film-free areas, the surface intermediate Mg^+ is generated and subsequently reacts in this anodic process. Alloying can influence E_{pt} and with that the film breakdown. The alloying elements can accelerate or decelerate the dissolution process due to galvanic coupling in the alloy, which is described later on.

2.2.3 Cathodic process

Usually, oxygen reduction is one of the key cathodic processes of corroding metals, but this is not the case for magnesium and its alloys. In magnesium, cathodic hydrogen evolution dominates the cathodic process during corrosion. The equilibrium potential of magnesium is more negative than the hydrogen evolution potential, meaning that the reaction is cathodically polarized. Oxygen reduction in neutral or alkaline solution can still occur, but does not play such a major role as in other conventional metals.

Normal cathodic hydrogen evolution (NHE) In the NHE, water from the neutral or alkaline solution is adsorbed on the surface

$$\mathrm{H_2O} + \mathrm{e^-} \longrightarrow \mathrm{H_{ad}} + \mathrm{OH^-}\,, \tag{12}$$

which then combines to form hydrogen

$$2\,\mathrm{H_{ad}} \longrightarrow \mathrm{H_2} \tag{13}$$

or gaseous H_2

$$\mathrm{H_{ad}} + \mathrm{H^+} + \mathrm{e^-} \longrightarrow \mathrm{H_2}\,. \tag{14}$$

The overall cathodic reaction can then be written as

$$2\,H_2O + 2\,e^- \longrightarrow H_2 + 2\,OH^- \,. \tag{15}$$

The NHE can occur as long as the potential is still negative, whereas the hydrogen overpotential significantly affects the hydrogen evolution rate.

Intermediate Mg^+-catalyzed hydrogen evolution Another possible reaction taking place at cathodically strongly polarized potentials is a Mg^+-catalyzed hydrogen evolution. There, Mg^{2+} is reduced into an intermediate Mg^+

$$Mg^{2+} + e^- \longrightarrow Mg^+ \,, \tag{16}$$

which then reacts with water to generate hydrogen

$$Mg^+ + 2\,H_2O \longrightarrow 2\,Mg^{2+} + 2\,OH^- + H_2 \,. \tag{17}$$

The overall cathodic reaction can be written as

$$2\,H_2O + 2\,e^- \longrightarrow 2\,OH^- + H_2 \,. \tag{18}$$

This process is only likely when the magnesium is strongly cathodically polarized and when dissolved Mg^{2+} is present in the solution. Another possible reaction includes the presence of $Mg(OH)_2$ to generate Mg^+

$$Mg(OH)_2 + e^- \longrightarrow Mg^+ + 2\,OH^- \tag{19}$$

whereby this reaction takes place at potentials much more negative than Eq. (16) and will end as the $Mg(OH)_2$ is fully consumed.

Intermediate MgH_2-catalyzed hydrogen evolution Similar to the process above, a MgH_2-catalyzed hydrogen evolution can occur, where Mg^{2+} or $Mg(OH)_2$ is reduced together with protons at the surface

$$\mathrm{Mg^{2+} + 2\,H^{+} + 4\,e^{-} \longrightarrow MgH_2} \tag{20}$$

or

$$\mathrm{Mg(OH)_2 + 2\,H^{+} + 4\,e^{-} \longrightarrow MgH_2 + 2\,OH^{-}}\ . \tag{21}$$

The formed MgH_2 on the magnesium surface further oxidizes particularly to generate hydrogen gas and Mg^{2+}

$$\mathrm{MgH_2 + 2\,H_2O \longrightarrow Mg^{2+} + 2\,OH^{-} + 2\,H_2 \longleftrightarrow Mg(OH)_2 + 2\,H_2}\ . \tag{22}$$

The overall cathodic reaction then is

$$\mathrm{2\,H_2O + 2\,e^{-} \longrightarrow 2\,OH^{-} + H_2} \tag{23}$$

in neutral or alkaline solutions. If the polarization potential is not too negative, the cathodic hydrogen evolution may follow the catalyzed process in addition to the NHE, but is less likely in practice due to the four electrons involved.

Possible hydrogen ingress and $\mathbf{MgH_2}$ formation The most probable magnesium hydride formation on magnesium occurs due to hydrogen adsorption or hydrogen storage. In the NHE, hydrogen adsorbes on the magnesium surface due to reduction of water

$$\mathrm{H_2O + e^{-} \longrightarrow H_{ad} + OH^{-}}\ . \tag{24}$$

The adsorbed hydrogen can react with magnesium, before it combines to H_2, forming MgH_2, which stays on the surface. Another possibility is that the hydrogen diffuses into the bulk magnesium and then combines to form MgH_2

$$2\,H_{ad} + Mg \longrightarrow MgH_2 \tag{25}$$

or

$$H_{ad} \longrightarrow H_{Mg} \ , \tag{26}$$

$$2\,H_{Mg} + Mg \longrightarrow MgH_2 \ . \tag{27}$$

In pure magnesium, defects such as dislocation and grain boundaries could act as quick diffusion paths into the matrix. This possible ingress could have a critical impact for magnesium with stress corrosion cracking (SCC). The MgH_2 on the magnesium surface can further react with water to produce hydrogen

$$MgH_2 + 2\,H_2O \longrightarrow Mg^{2+} + 2\,OH^- + 2\,H_2 \longrightarrow Mg(OH^-)_2 + 2\,H_2 \tag{28}$$

and the overall cathodic reaction can be written as

$$Mg + 4\,H_2O + 2\,e^- {=} Mg(OH)_2 + 2\,OH^- + 2\,H_2 \ , \tag{29}$$

meaning that MgH_2 mainly stays inside the magnesium matrix and is not stable in contact with the aqueous solution.

All possible cathodic reactions are illustrated in Fig. 5. The different processes taking place are dependent on the conditions, whereby mainly one at a time dominates the cathodic process on magnesium. The MgH_2 formation is the least significant cathodic mechanism together with the hydrogen ingress, which can have a higher impact under some conditions. The other reactions follow the same cathodic hydrogen evolution process. Practically, the NHE is the dominant process occuring, since the other involve four electrons which rarely occur. Alloying does not influence the cathodic reactions per se, but influence the film on the surface and, therefore, the cathodic current density.

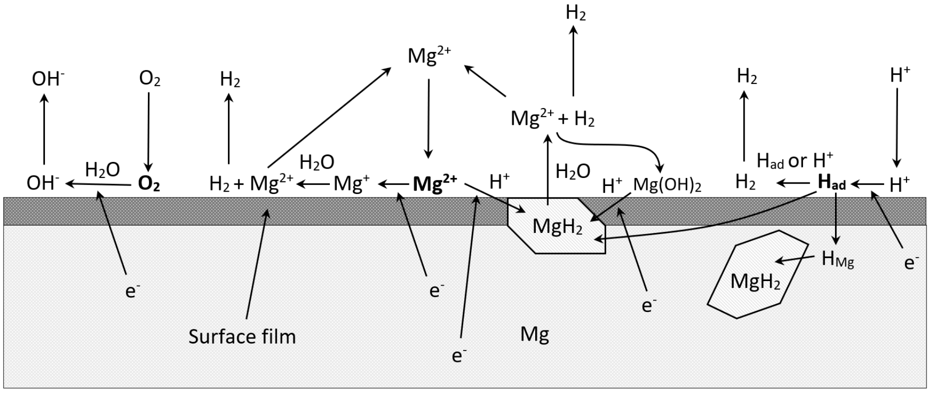

Figure 5: Cathodic processes. Redrawn after Song[18].

2.2.4 Self-corrosion of Magnesium

With the gathered anodic and cathodic processes stated above, the characteristic corrosion mechanisms and phenomena can be described as illustrated in Fig. 6.

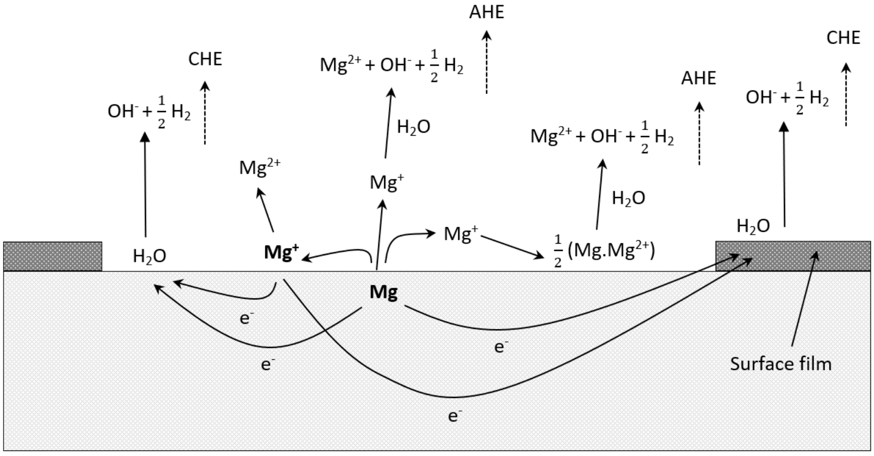

Figure 6: Self Corrosion. Redrawn after Song[18].

Under self-corrosion of magnesium, cathodic and anodic processes go hand in hand, since all electrons generated in anodic reaction are consumed by the cathodic reactions having the same rate. The overall corrosion reaction of magnesium can therefore be written with Eq. (11) and (15) as

$$Mg + 2\,H_2O \longrightarrow Mg^{2+} + 2\,OH^- + H_2 \tag{30}$$

in neutral or alkaline aqueous solutions. Essentially, the anodic reactions take place mainly at film-free surface areas and the cathodic reaction takes place at film-free and covered surface areas, whereby the rate on covered areas is much slower. This self-corrosion process is also valid for typical Mg-based implant alloys, since the matrix mainly consists of magnesium and has a similar crystalline structure. The corrosion behaviour will occur with the same processes and reactions taking place, whereas other phases present in the alloy will act as galvanic couples. Estimating the self-corrosion rate is one of the main goals when developing new types of magnesium materials for applications. Since hydrogen evolution is one of the most fundamental and distinct phenomena during the corrosion of magnesium, the generated hydrogen is collected and used to determine the characteristic corrosion rate of magnesium alloys since tafel plots often underestimate these rates. The corrosion of magnesium is accompanied by an increased pH of the solution near the surface. This alkalization process is caused by the generated hydroxyls, which take time to diffuse away from the surface into the bulk solution. The increased pH stabilizes at ≈ 10.5, since the deposition of $Mg(OH)_2$ dominates in that pH region and stabilizes the pH level. The alkalization process depends on the magnesium specimen surface to solution volume ratio and can, therefore, vary for different systems.

2.2.5 Corrosion of magnesium alloys

Since magnesium exhibits such a negative corrosion potential, it will always act as anode in the corrosion processes in contact with other metals. This galvanic effect causes the main damage for the magnesium alloy, if micro-anodes and cathodes form within the alloy. The corrosion potential difference between the electrodes determines significantly the galvanic corrosion rate I_g, and can drastically accelerate the corrosion of the magnesium matrix. The electrochemical activity within the alloy can vary, since the composition, microstructure and crystalline orientation is not uniform throughout the material and generate differently active micro-galvanic couples as illustrated in Fig. 7.

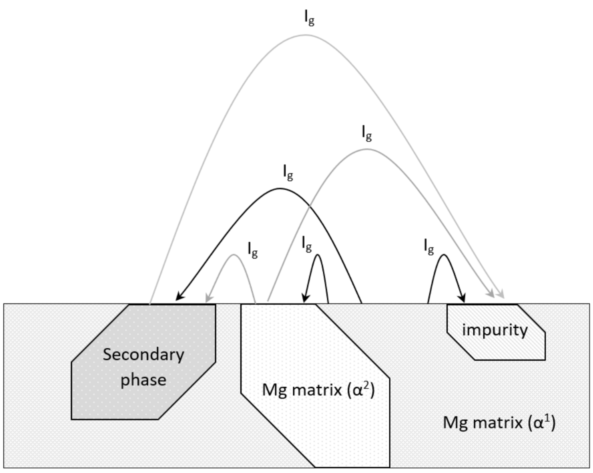

Figure 7: Micro-galvanic coupling. Redrawn after Song[18].

Grain orientation Different grain orientations exhibit different corrosion rates, which can be related to the atomic density of the particular crystal planes. Planes with a lower atomic density are dissolved much faster than planes with a higher atomic density.

Secondary phases Secondary phases can accelerate or decelerate the corrosion of the alloy, depending on the electrochemical potential, amount, distribution and continuity.

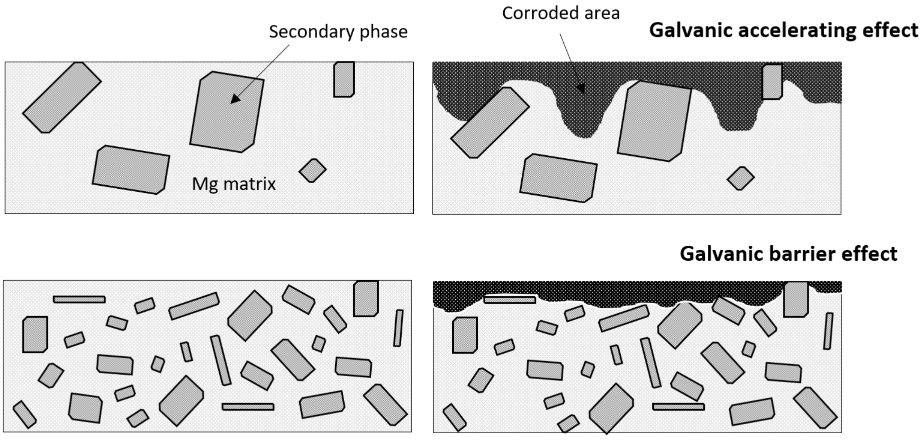

Figure 8: Secondary phase corrosion effects. Redrawn after Song[18].

Finely and continuously distributed secondary phases may act as corrosion barriers, confining the corrosion front, as illustrated in Fig. 8. Larger and less distributed secondary phases in contrast may accelerate the dissolution of the magnesium matrix and the corrosion front reaching deeper in the matrix.

Impurities Impurities can accelerate the dissolution of the magnesium alloy due to the galvanic coupling effect. The influence of impurities on the corrosion resistance is dependent on their concentration. Their detrimental effect is insignificant below a tolerance limit, whereas, when the tolerance limit is exceeded, the corrosion rate is considerably increased. This tolerance limit of impurities is often related to their solubility in the alloy matrix phase.[18,21]

The corrosion behaviour of magnesium alloys is inevitable dependent on the formed micro-galvanic couples in the alloy. Due to this non-uniformity in the magnesium alloys, the corrosion will be strongly localized with different corrosion rates on different sites in contact with the solution. Initiated small pits will spread over the surface without penetrating deep into the matrix, due to the alkalization effect which decelerates the dissolution in these areas. This results in a relatively widespread corrosion front in the early stages of corrosion, in contrast to commonly known pitting processes.[18,22] In the later stages, locally deep pits can form.[22] Often, secondary phases are more corrosion resistant than the surrounding matrix. In such cases, the magnesium matrix surrounding the intermetallic phases is more corroded along the phase boundaries, which can result in undermining of these particles, as shown in Fig. 9.

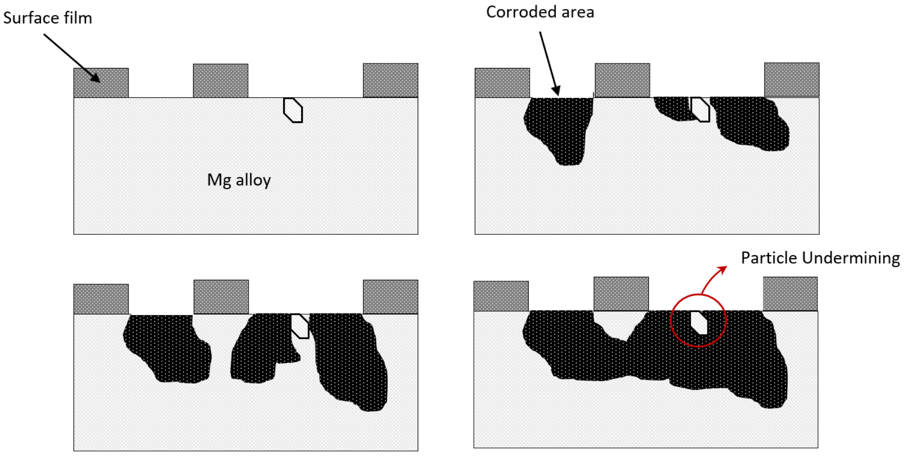

Figure 9: Localized pitting corrosion. Redrawn after Song[18].

2.3 Electrochemical Impedance Spectroscopy (EIS)

This chapter is mainly based on the book by Orazem and Tribollet, *Electrochemical Impedance Spectroscopy*, chapters *A Brief Introduction to Impedance Spectroscopy*[23] and *Equivalent Circuit Analogs*[24].

Electrochemical Impedance Spectroscopy (EIS) is a versatile tool in electrochemistry, which can give insight in kinetic processes, the influence of stored charge and the presence of adsorbed intermediates on electrode-electrolyte interfaces. This can be used to study the corrosion properties of magnesium and its alloys as described in 2.3.1.

The basic approach in EIS measurements is to apply a modulated electrical potential and observe the resulting current. For a linear time-invariant system (LTI), the relationship between input and output is called *transfer function* and, in case of electrochemical sytems, is the inverse impedance called admittance Y. The dependence of the transfer function on frequency contains the information on the behaviour of the system.

If the imposed input signal is sinusodial, it can be described by

$$V(t) = \overline{V} + |\Delta V| \cos(\omega t) = \overline{V} + Re\left(\widetilde{V} \exp(j\omega t)\right) \ , \tag{31}$$

where $\overline{V}$ is the time-invariant part, ΔV is the magnitude of the oscillating part of the input signal, and $\widetilde{V}$ is a complex quantity which is a function of frequency, but independent of time. For a linear response, the output will have the same form and frequency as the input signal

$$i(t) = \overline{i} + |\Delta i| \cos(\omega t + \phi) = \overline{i} + Re\left(\widetilde{i} \exp(j\omega t)\right) \ , \tag{32}$$

where ϕ is the phase lag between input and output signal.

The admittance $Y(\omega)$ is solely dependent on frequency and can be described by its magnitude $|Y(\omega)|$ and the phase lag $\phi(\omega)$ at a given frequency ω. $|Y(\omega)|$ is defined as ratio of the amplitudes of the output $\left|\widetilde{i}(\omega)\right|$ and the input signal $\left|\widetilde{V}(\omega)\right|$, and can be written as

$$|Y(\omega)| = \frac{|i|}{|V|} = \frac{\left|\widetilde{i}(\omega)\right|}{\left|\widetilde{V}(\omega)\right|} \ . \tag{33}$$

$\phi(\omega)$ between input and output signal can be written as

$$\phi(\omega) = 2\pi\frac{\Delta t}{T} \ , \tag{34}$$

where Δt is the time lag, and T is the period of the two signals. When considering the input signal as reference for the phase, the input signal is real and the output signal is a complex number with magnitude $\left|\widetilde{i}(\omega)\right|$ and phase $\phi(\omega)$. Therefore, the admittance can be written as

$$Y(\omega) = \frac{\widetilde{i}(\omega)}{\widetilde{V}(\omega)} = \frac{\left|\widetilde{i}(\omega)\right|}{\left|\widetilde{V}(\omega)\right|}(\cos\phi(\omega) + j\sin\phi(\omega)) \ . \tag{35}$$

The impedance $Z(\omega)$ is the inverse of the admittance $Y(\omega)$ and, thus, defined as

$$Z(\omega) = \frac{1}{Y(\omega)} = \frac{\widetilde{V}(\omega)}{\widetilde{i}(\omega)} \ . \tag{36}$$

Although the admittance is measured in electrochemical systems, the impedance is used to describe the transfer function through physical models using e.g. equivalent circuit analogs. Processes in electrochemical systems are distinguishable due to their timeline when they take place. For example, charging of the electrode-electrolyte interface happens rapidly, whereas diffusion is a slower process. Hence, the time constants differ significantly, which manifests in their characteristic frequencies. The impedance will be determined by subsequent analysis in a given frequency window.[23]

2.3.1 Physical model for the corrosion behaviour of magnesium

Proposing a physical model to the measured electrochemical impedance spectrum can be quite challenging, since reaction sequence, mass transfer and physical phenomena have to be considered. Therefore, a framework according to the corrosion behaviour of the studied magnesium alloy has to be constructed according to the mechanisms stated in 2.2 and the resulting electrode development shown in Fig. 10.

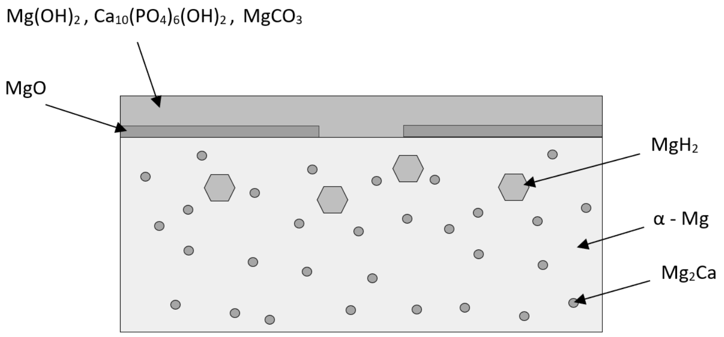

Figure 10: Scheme of the MgCaZn alloy surface structure.

The first step in proposing an equivalent circuit is to define the current paths and potential drops in the system. The simplest model to start with is the bare Mg alloy-electrolyte interface, as illustrated in Fig. 11. The potential drop is a sum of the contributions from the interfacial impedance Z_0 and the electrolyte resistance R_e, resulting in an impedance Z consisting of the electrolyte resistance in series with the interfacial impedance

$$Z = R_e + Z_0 \ . \tag{37}$$

At the interface of the Mg-alloy, the overall current is a sum of the charging current i_{dl} through a double-layer capacitor and a faradaic current i_F. Thus, the resulting interfacial impedance consists of a double-layer capacitor C_{dl} and a faradaic impedance Z_F in parallel

$$Z_0 = \frac{Z_F}{1 + j\omega C_{dl} Z_F} \ . \tag{38}$$

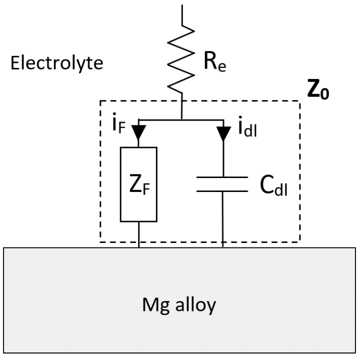

Figure 11: Equivalent circuit for Mg alloy-electrolyte interface. Redrawn after Orazem[24].

The faradaic impedance is used to describe more complicated interfacial responses of the alloy surface caused by coupled reactions, adsorbed intermediates and from the nonuniform corrosion behaviour. The surface of the Mg-alloy may be partially covered by an oxide layer formed on air, as shown in Fig. 12. The formed layer may block the flow of faradaic current in the coated regions. The insulating MgO surface layer does not fully cover the surface and, therefore, has a fractional coverage γ and is considered as layer capacitance C_l. The uncovered, active surface has a remaining fraction of $1-\gamma$. The impedance can be expressed as

$$Z = R_e + \frac{\frac{Z_F}{(1-\gamma)}}{1 + j\omega(\gamma C_l + (1-\gamma)C_{dl})\frac{Z_F}{(1-\gamma)}} \tag{39}$$

or

$$Z = R_e + \frac{Z_{F,\gamma}}{1 + j\omega(C_{l,\gamma} + C_{dl,\gamma})Z_{F,\gamma}} \tag{40}$$

with

$$Z_{F,\gamma} = \frac{Z_F}{1-\gamma} \ , \tag{41}$$

$$C_{l,\gamma} = \gamma C_l \ , \tag{42}$$

$$C_{dl,\gamma} = (1-\gamma)C_{dl} \ , \tag{43}$$

where $Z_{F,\gamma}$, $C_{l,\gamma}$, $C_{l,\gamma}$ and $C_{dl,\gamma}$ are the parameter obtained by fitting with an equivalent circuit and which depend on the fractional coverage.

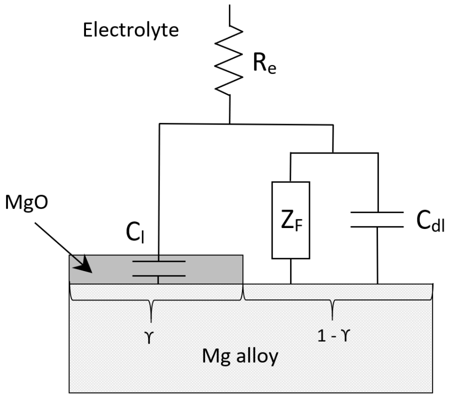

Figure 12: Equivalent circuit for a partially blocked Mg-alloy surface. Redrawn after Orazem[24].

As γ approaches 0, the impedance will be that of the uncoated surface above. As it approaches unity, the impedance will be defined by the capacity of the fully blocked electrode as

$$Z = R_e + \frac{1}{j\omega C_l} \ . \tag{44}$$

The MgO surface film will not be very dense during the ongoing corrosion in aqueous environments as it is not the most stable product. In a more advanced model, the surface layer is considered to be more porous with a surface coverage approaching 100 %. The electrochemical reactions occur now solely at the ends of the pores nearby the surface. Thus, the impedance associated with the MgO layer in Fig. 12 is expanded by the introduction of an additional electrolyte resistance R_l within a pore length, which is parallel to the coating capacitance C_l as shown in Fig. 13. The impedance can be written as

$$Z = R_e + \frac{R_l + \frac{Z_F}{1+j\omega C_{dl} Z_F}}{1-\gamma + j\omega\gamma C_l\left(R_l + \frac{Z_F}{1+j\omega C_{dl} Z_F}\right)} \tag{45}$$

or

$$Z = R_e + \frac{R_{l,\gamma} + \frac{Z_{F,\gamma}}{1+j\omega C_{dl,\gamma} Z_{F,\gamma}}}{1 + j\omega C_{l,\gamma}\left(R_{l,\gamma} + \frac{Z_{F,\gamma}}{1+j\omega C_{dl,\gamma} Z_{F,\gamma}}\right)} \tag{46}$$

with

$$R_{l,\gamma} = \frac{R_l}{1-\gamma} \ , \tag{47}$$

where $Z_{F,\gamma}$, $C_{l,\gamma}$, $C_{l,\gamma}$, $C_{dl,\gamma}$ and $R_{l,\gamma}$ are again the parameter obtained by fitting with an equivalent circuit. To determine the fractional coverage γ, a value for C_{dl} must be assumed. From the coating capacity C_l, the thickness of the MgO surface layer δ can be calculated using

$$\delta = \frac{\epsilon\epsilon_0 A}{C_l} \ , \tag{48}$$

where ϵ and ϵ_0 are the dielectric constant and the permittivity of vacuum, respectively, and A is the area of the coating.

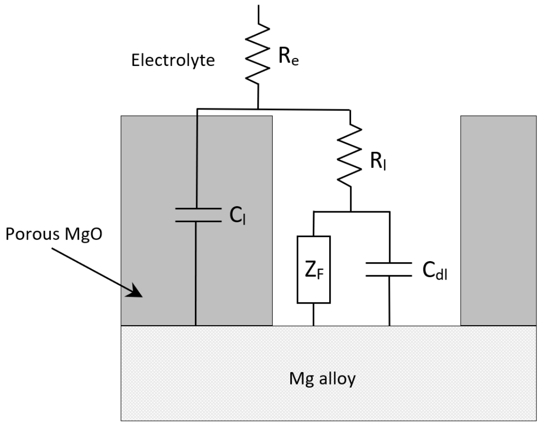

Figure 13: Equivalent circuit for a porous MgO surface layer on Mg-alloy. Redrawn after Orazem[24].

Since MgO is less stable in aqueous solutions than $Mg(OH)_2$, a second film will cover the Mg-alloy surface. The less dense $Mg(OH)_2$ layer will cover the MgO layer as well as the surface active area in between. Therefore, the equivalent circuit can be described similarly as above with an additional capacitance $C_{l,2}$ accounting for the charge transfer and $R_{l,2}$ for the electrolyte resistance in the pores of the second layer. The equivalent circuit is a rough approximation, since it assumes an abrupt transition between the first and the second layer on an equipotential plane and neglects irregularities along the layers. It provides a good model for the corrosion product layer system of Mg and its alloys, since the outer $Mg(OH)_2$ layer is assumed to be thicker than the more dense inner MgO layer. The corresponding equivalent circuit is shown in Fig. 14 and can be described by

$$Z = R_e + \frac{R_{l,2}}{1 + j\omega R_{l,2} C_{l,2}} + \frac{R_{l,1,\gamma} + \frac{Z_{F,\gamma}}{1+j\omega C_{dl,\gamma} Z_{F,\gamma}}}{1 + j\omega C_{l,\gamma} \left(R_{l,1,\gamma} + \frac{Z_{F,\gamma}}{1+j\omega C_{dl,\gamma} Z_{F,\gamma}} \right)} \,. \tag{49}$$

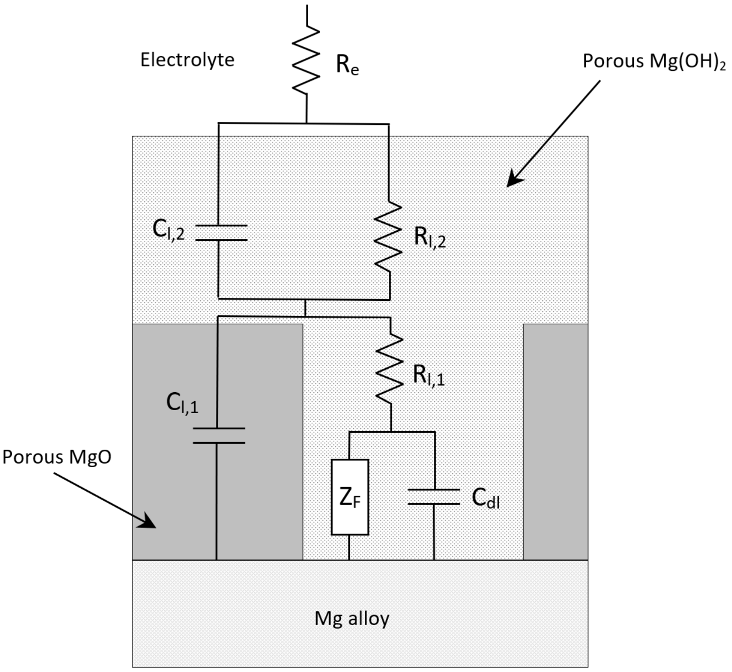

Figure 14: Equivalent circuit for corrosion product surface layers on Mg-alloy impedance. Redrawn after Orazem[24].

The growth of the $Mg(OH)_2$ layer will be observable in the increase of $R_{l,2}$ since the characteristic frequency of the layer is experimentally not observable.

The layer thickness can be estimated using

$$R_{l,2} = \frac{\delta_{l,2}}{\kappa_{l,2} A} = \frac{\rho_{l,2}\delta_{l,2}}{A} \ , \tag{50}$$

where $\kappa_{l,2}$ is the effective coating conductivity, $\rho_{l,2} = \frac{1}{\kappa_{l,2}}$ is the effective coating resistivity, and A is the area of the coating.[24]

To describe the complex faradaic impedance Z_F, a kinetic model accounting for the interfacial electrochemical reactions is needed. The reactions describing the corrosion of Mg are not only dependent on potential, but also on the surface coverage of intermediate adsorbed species Mg^+ involved in the two-step dissolution reaction, and on the mass transport of reactants to the Mg surface.[25] During corrosion, the dissolved ionic Mg^{2+} diffuse away from the surface within a finite diffusion length and react via a backward reaction with intermediate Mg^+ adsorbed on the surface, resulting in the unique hydrogen evolution characteristic for Mg caused by the NDE.[25,26]

Therefore, a proposed equivalent circuit describing the corrosion behaviour of Mg is shown in Fig. 15, which is similar to proposed equivalent circuits by King, Baril and Liu[26–28]. The circuit consists of two parallel impedances, Z_A and Z_C, describing the anodic and cathodic processes on the Mg surface. The cathodic impedance Z_C accounts for the potential dependence in form of a charge transfer resistance R_1, associated with the cathodic hydrogen evolution at cathodic sites. Additionally, a finite-length diffusional impedance consisting of of a capacity C_2 in parallel with a resistance R_2 is proposed, accounting for the diffusion of Mg^{2+} through the porous $\mathrm{Mg(OH)_2}$ layer and the accompanied variation of concentration of reacting Mg^{2+} nearby the alloy surface.[25–28] The diffusional impedance is strongly dependent on the surface condition and, therefore, on the porosity of the forming corrosion product film.[29] The anodic impedance Z_A accounts for the adsorbed intermediates Mg^+ during the dissolution of Mg associated with a fractional surface coverage, and is accompanied by a local anodic hydrogen evolution described by an inductance L in series with a resistance R_3.[25–28] The occurrence of an inductance L is typically associated with relaxation processes of adsorbed species on surfaces.[26–28]

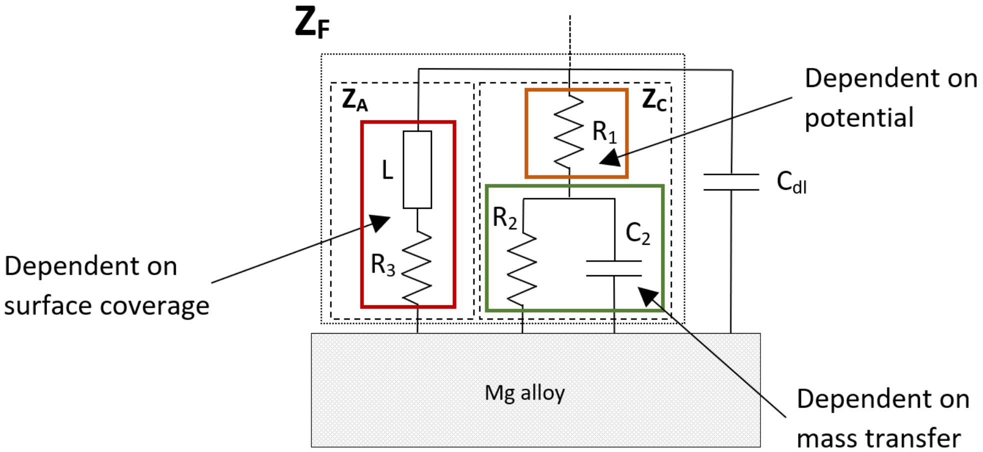

Figure 15: Equivalent circuit for faradaic impedance of Mg-alloy corrosion mechanisms. Redrawn after Liu, King and Baril[26–28]

2.4 Positron Annihilation Lifetime Spectroscopy (PALS)

The existence of antimatter was theoretically predicted by Dirac (1928) as interpretation of negative electron energy levels and verified by Anderson‘s experimental proof (1932) of the existence of positrons (e^+), the antiparticle of the electron.[30,31] Since the 1960s, positron physics gained increased attention due to the unique information which can be obtained from the interaction and annihilation of positrons in condensed matter.[30,32] One of the developed positron techniques is called Positron Annihilation Lifetime Spectroscopy (PALS). PALS is a non-destructive method to investigate structural defects and the formation of new phases in solids, since the average lifetime of the positrons entering matter is dependent on the electron density at the site of annihilation.[32] In the following sections, the interaction and annihilation of positrons in solids and the used positron technique PALS to investigate the evolution of open-volume defects during ex-vitro corrosion of magnesium are described in detail.

2.4.1 Positron and Positronium

The *positron* e^+ is the antiparticle of the electron, hence it resembles the properties of the electron. The positron has the same spin ($\frac{1}{2}$) and mass as the electron, while charge and magnetic momentum are opposite. While it is stable in vacuum, in contact with matter it looses its kinetic energy in a series of interactions down to thermal energies and will annihilate with electrons, as described in 2.4.2. The positron has a typical mean lifetime of a few hundred picoseconds and will mainly annihilate with an electron into 2 emitted γ-rays (annihilation into higher number can be neglected), each carrying an energy of 511 keV.

$$\mathrm{e}^+ + \mathrm{e}^- \longrightarrow 2\,\gamma \ . \tag{51}$$

The *positronium* (Ps) is a quasi-stable bound state of an electron and a positron. This state is held together by electromagnetic interactions until the antiparticle pair annihilates. The Ps has two ground states, dependent on the spin orientations of electron and positron, called para-positronium (*p*-Ps) and ortho-positronium (*o*-Ps).[30,31,33]

2.4.2 Positron interactions in solids

The interactions of positrons with solids are shown in Fig. 16. Incident positrons can either enter the solid or be reflected back out. Positrons that enter the solid show high kinetic energies dependent on the positron source and slow down rapidly to thermal energies ($\approx 25\,\mathrm{meV}$) within a few ps. This process is called *thermalization.* Some of the penetrating positrons will channel through the solid, whereas the probability decreases with increasing thickness of the solid. Penetrating positrons will loose part of their kinetic energy due to ionization and excitation of core electrons, whereby secondary electrons may leave the solid. While attaining equilibrium, positrons continuously slow down due to excitation of plasmons and electron-hole pairs above the Fermi energy and scattering and excitation of phonons below. Some of the nonthermal positrons will diffuse back to the surface, where they leave the solid or pick up an electron in the bulk and leave as fast Ps in its ground or excited state. Once the positrons are thermalized, they diffuse through the solid and will then either annihilate with an electron in the bulk or get trapped in defects before they annihilate. The mean diffusion length for positrons in metals lies in the range of $L_+ = \sqrt{D_+\tau_B} \approx 100 - 200\,\mathrm{nm}$ with typical positron bulk lifetimes of $\tau_B \approx 100 - 200\,\mathrm{ps}$. A part of the positrons will diffuse back to the surface and leave the solid as thermalized positrons, provided the solid has a negative positron work function, or energetic surface-formed Ps. Some positrons will get trapped at the surface, where they annihilate or thermally adsorb as Ps. Formed *o*-Ps outside the solid will decay emitting 3 γ-rays.[30,31,33]

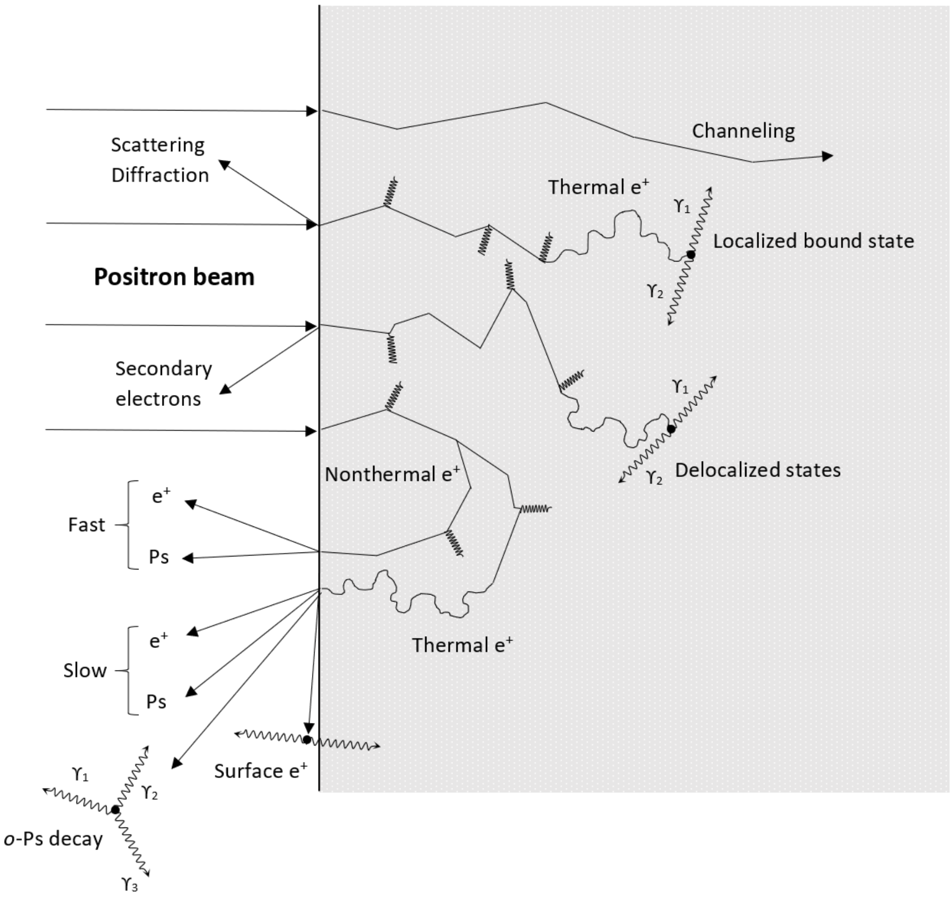

Figure 16: Interactions of positrons with solids and their surfaces. Redrawn after Szeles and Lynn[30].

The *annihilation* rate λ of the antimatter pair is given by the overlap of the positron $n^+(r)$ and electron density function $n^-(r)$ in the solid, i.e. the probability to find an electron at the position of a positron. Therefore, λ, which is inverse proportional to the positron lifetime τ, can be written as

$$\lambda = \frac{1}{\tau} = \pi r_0^2 c \iiint n^+(r) n^-(r) \epsilon(n^-(r)) \; \mathrm{d}^3 r \ , \tag{52}$$

where r_0 is the classical electron radius, c is the speed of light, and $\epsilon(n^-(r))$ denotes the enhancement of electron density in the vicinity of the positron. Due to the Coulomb attraction of electron and positron, the electron density is higher in the surrounding of positrons, which increases the annihilation probability and in turn decreases the positron lifetime. In metals, approximated as homogeneous (free) electron gas, this reduces to

$$\lambda = \pi r_0^2 c n^- \ . \tag{53}$$

Consequently, the annihilation probability and, therefore, the inverse of the positron lifetime is proportional to the electron density $n^-(r)$ in the solid. For annihilation in delocalized states, the positron lifetime represents the average electron density between lattice sites. For annihilation in defect states, it gives information on the local electron density at the trapping site. This direct relationship between electron density and positron lifetime is used in *Positron Annihilation Lifetime Spectroscopy* as described in 2.4.5.[30]

2.4.3 Positron interactions with lattice defects in metals

Thermalized positrons move in delocalized state as Bloch waves through the crystal. The positron density is much higher in between lattice sites due to the Coulomb repulsion from the core ions of the atoms. The state of the positrons changes significantly close to lattice sites, where the crystal periodicity is changed or broken. If an atom is removed from the lattice, the local electrostatic potential changes, since the strong repulsive, positive potential of the core as well as the core electrons are missing. The delocalized valence electrons at the vacancy site then act as an attractive site for positrons, which is called *positron trap*. If this positron trap is strong enough, localized bound states will form. This transition from a delocalized state, where positrons move in Bloch waves to a localized bound state of the positrons at lattice defects, is called *trapping*.[30]

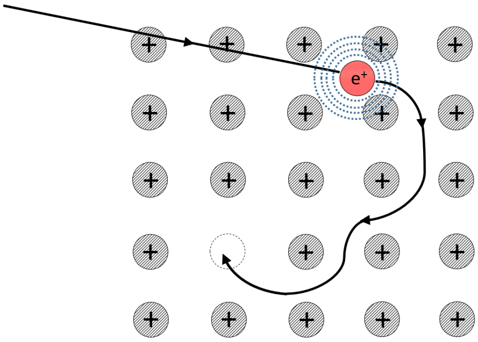

Figure 17: Local potential minimum at defect states caused by missing ions cores. Incident positrons thermalize rapidly and diffuse in the lattice until they get localized at sites of minimum potential energy. Redrawn after Schultz[31].

Positrons get trapped at any defect with attractive potential, whereas most of them are open-volume defects, as shown in Fig. 17. The annihilation properties of positrons in open-volume defects are mostly affected by the decreased electron density due to missing core electrons, which significantly increases the positron lifetime in defects compared to the annihilation from delocalized states in the bulk. This difference in the positron lifetimes provides Positron Annihilation Lifetime Spectroscopy its sensitivity for the detection of lattice defects such as vacancies, vacancy cluster, dislocations, grain boundaries and voids.[30] So various stable or metastable localized positron states may be formed in these lattice defects, whereby the positron lifetimes in these trapping states are dependent on the defect size, their atomic configuration and their charge state. This is used to distinguish between the occurring, competing defects in a solid.[30,34]

2.4.4 Trapping model

The annihilation rate for a positron in a localized state is determined by the local electron density at a defect site attracting the positron, and the decay is simple exponential. Understanding the arising single- or multi-exponent spectra from experimental observations is important for the interpretation of the obtained results.[34] The most simple model to describe the trapping of positrons in defects is the *two-state trapping model* (rate equations). It describes the annihilation process in solids with a single defect type as

$$\begin{aligned} \frac{\mathrm{d}n_b(t)}{\mathrm{d}t} &= -\lambda_b n_b(t) - \kappa_d n_b(t) \\ \frac{\mathrm{d}n_d(t)}{\mathrm{d}t} &= -\lambda_d n_d(t) + \kappa_d n_b(t) \ , \end{aligned} \tag{54}$$

where $n_b(t)$ and $n_d(t)$ are the bulk and the trapped positron densities at time t, λ_b and λ_d are the annihilation probabilities in the two states, and κ_d is the trapping rate. There is a finite probability, that a trapped positron escapes from the localized bound state within their lifetime by thermal excitation, but will be not considered here.[30] Under the assumption, that at $t = 0$ all positrons are delocalized in a Bloch states ($n_b(0) = N_0$ and $n_d(0) = 0$), the solution of the linear differential is the positron decay spectrum $D(t)$[35,36]

$$D(t) = I_1 \exp\left(-\frac{t}{\tau_1}\right) + I_2 \exp\left(-\frac{t}{\tau_2}\right) \tag{55}$$

with

$$I_1 = 1 - I_2 \ , \tag{56}$$

$$I_2 = \frac{\kappa_d}{\lambda_b - \lambda_d + \kappa_d} \ , \tag{57}$$

$$\tau_1 = \frac{1}{\lambda_b + \kappa_d} \ , \tag{58}$$

and

$$\tau_2 = \frac{1}{\lambda_d} \ , \tag{59}$$

where I_1 and I_2 are the intensities of the positron lifetime τ_1 in the free, delocalized state and τ_2 in the bound defect state, respectively. The experimentally obtained free positron lifetime is reduced compared to the bulk positron lifetime (material parameter), due to the rate $\lambda_1 = \lambda_b + \kappa_d$ by which positrons are removed from the free state, as seen in eq. (58). The actual bulk lifetime τ_b of the solid can then be expressed as

$$\tau_b = \frac{1}{\lambda_b} = \left(\frac{I_1}{\tau_1} + \frac{I_2}{\tau_2}\right)^{-1} \ . \tag{60}$$ [35,36]

The mean lifetime of positrons in a solid $\overline{\tau}$ can be calculated as

$$\overline{\tau} = \sum_i I_i \tau_i \ , \tag{61}$$

where τ_i are the positron lifetime components, and I_i are the corresponding intensities.[30]

With the underlying assumption in the Ansatz of the rate equations (average distance between lattice defects is much smaller than the diffusion length L_+ of the positrons), the trapping rate κ_d in the defect is proportional to the defect concentration and can be written as

$$\kappa_d = \mu C_d = I_2 \left(\frac{1}{\tau_1} - \frac{1}{\tau_2} \right) = \frac{I_2}{I_1} \left(\frac{1}{\tau_b} - \frac{1}{\tau_d} \right) \ , \tag{62}$$

where μ is the trapping coefficient or specific trapping rate, and C_d is the defect concentration.[30,35,36] The specific trapping rate is determined by the transition probability from the delocalized to the localized state at the defect site, which is dependent on the depth of the trap. Since the trapping rate is proportional to the defect concentration, *saturated trapping* at a defect with high concentrations is possible. This means, that a majority of positrons that enter the solid are trapped at one dominant defect type.[30]

2.4.5 Positron Annihilation Lifetime Spectroscopy

To study bulk properties of a solid, positrons are emitted from radioactive sources, like ^{22}Na (β^+-decay), and implanted into the solid. The source should provide a high yield of positrons with high kinetic energy.[37] The positrons from these radioactive sources have a continuous energy distribution, resulting in an exponential implantation profile $P(z)$ as

$$P(z) = \alpha_+ \exp(-\alpha_+ z) \ , \tag{63}$$

where $P(z)$ is the propability of penetration to depth z and α_+ is the linear absorption coefficient. This linear absorption coefficient can be approximated by

$$\alpha_+ \ [cm^{-1}] \approx \frac{\alpha_0 \rho \ [gcm^{-3}]}{E_{max}^{1,4} \ [MeV]} \ , \tag{64}$$

where $\alpha_0 = (16 \pm 1)\,\mathrm{cm}^2(\mathrm{keV})^{1.4}/\mathrm{g}$[38] is a numerical coefficient, ρ is the density of the solid, and E_{max} is the maximum energy of the positrons emitted from the source (for ^{22}Na: 544 keV[37]). This results in a mean penetration depth in solids of ≈ 10-100 µm.[30]

The stopping profile $S(z)$ can, therefore, be dervied as

$$S(z) = 1 - P(z)\ . \tag{65}$$

When ^{22}Na is used as source of positrons, a positron is emitted after its decay to an excited state of ^{22}Ne, whereas the excited state decays just a few picoseconds afterwards to the ground state of ^{22}Ne emitting an additional 1.28 MeV γ photon. This is used as birth signal of the positron. In PALS experiments, the time between the birth signal and the annihilation γ photons (stop signal) is measured, as shown in Fig. 18.[32] A detailed description of the signal processing as well as a Block diagramm of the used fast-fast positron lifetime spectrometer can be found in Ref.[35,36].

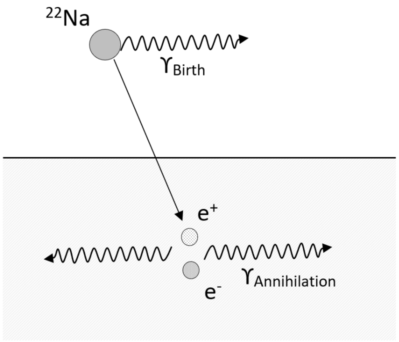

Figure 18: Positron Annihilation Lifetime Spectroscopy. The time delay between the photon γ_{Birth} from the ^{22}Na-decay and the photon $\gamma_{Annihilation}$ is measured. Redrawn after Hautojärvi and Vehanen[32].

The measured positron lifetime spectrum is a convolution of the time-resolution function of the spectrometer $G(t)$ (sum of gaussian components) and a sum of exponentials $N(t)$ corresponding to the various defect states in the solid, which can be written as

$$P(t) = \int_{-\infty}^{\infty} G(\tau) N(t-\tau)\ \mathrm{d}\tau \tag{66}$$

with

$$N(t) = \sum_i \frac{I_i}{\tau_i} \exp\left(-\frac{t}{\tau_i}\right)\ . \tag{67}$$

In order to extract the occurring positron lifetimes and the associated intensities, a model function has to be fitted to the measured spectrum. Since numerical fitting of the experimental lifetime spectra and the decomposition into multiple components can be difficult, especially for similar ranged lifetimes, a more reliable parameter is obtained calculating the mean lifetime $\overline{\tau}$ as given by eq. (61).[30,35,36]

2.4.6 Positron Annihilation Lifetime Spectroscopy in magnesium

Pure magnesium is considered to be a border case concerning the trapping efficiency of positrons in vacancies, since it is located between sodium (Na) and aluminium (Al) in the periodic table, which show no trapping and efficient trapping, respectively. Magnesium exhibits a low positron-vacancy binding energy of 0.3 - 0.4 eV compared to other metals like Al with $\gtrsim 1.5\,\mathrm{eV}$. One consequence of the low positron-vacancy binding energy is a small difference between the positron lifetime of the free positrons in the bulk and the positron lifetime of positrons trapped in vacancies.[39]

The hexagonal close-packed crystal structure of magnesium has multiple slip systems, which can be activated during deformation. For smaller degrees of deformation, dislocation will dominate the annihilation properties. For higher degrees of deformation, a transition takes place with jogs and vacancies being the dominant defect type. This transition was described using a three-stage trapping model postulated from Smedskjaer et al.[40]. In this model, dislocations are associated as preliminary step to trapping in jogs or vacancies along the dislocation, since dislocations exhibit only a weak positron binding energy and the positrons will annihilate in these deeper traps.[41] That may explain why the difference between experimentally deduced positron lifetime in dislocations and free vacancies is only a few ps.

Severe plastic deformation, especially *high-pressure torsion (HPT)*, can significantly enhance the mechanical properties of magnesium by grain-refinement while introducing a higher density of defects. In HPT processing, a disk-shaped sample is strongly compressed by several GPa and simultaneously strained by rotating. In magnesium, the resulting structure exhibits a high volume fraction of grain boundaries and two differently grained regions.[42] One region is ultra-fine grained (UFG, 100 - 300 nm) with a high dislocation density, and the other region has larger grains (1 - 5 µm) and is almost free of dislocations due to a dynamic recovery during deformation. This results in positrons primarily annihilating at jogs and vacancies along dislocations in the UFG region, manifested in a reduced bulk positron lifetime and a defect lifetime characteristic for dislocations.[43]. Voids caused by deformation can give rise to the formation of *o*-Ps and the nucleation of cracks. An overview of experimentally determined and theoretically calculated bulk positron lifetimes τ_b and defect positron lifetimes τ_d of magnesium are listed in Tab. 1 and 2, respectively.

Table 1: Experimentally and theoretically determined bulk positron lifetime τ_b in magnesium.

$\tau_{b,exp}$ [ps]	Author	Reference
225	Hautojärvi et al.	[39]
222	Del Río et al.	[41]
225,3 ± 0.4	Cizek et al.	[44]
226 ± 1	Dryzek et al.	[45]
225	Campillo Robles et al.	[46]
218 ± 2	Macchi et al.	[47]
235	Nieminen and Manninen	[38]
$\tau_{b,theo}$ [ps]	Author	Reference
233,2	Cizek et al.	[44]
237	Puska and Nieminen	[48]
249	Nieminen and Manninen	[38]
203 - 233[1]	Campillo Robles et al.	[46]

[1] depending on the DFT-method used for calculation

Table 2: Experimentally and theoretically determined defect positron lifetime τ_d in magnesium.

$\tau_{d,exp}$ [ps]	Defect type	Author	Reference
237	Grain boundaries	Dryzek et al.	[49]
249 ± 2	Dislocations	Badawi et al.	[50]
244	Dislocations	Del Río et al.	[41]
255 - 257	Dislocations	Cizek et al.	[44]
253	Jogs	Del Río et al.	[41]
255 ± 5	Monovacancies	Hautojärvi et al.	[39]
254	Monovacancies	Campillo Robles et al.	[46]
255	Monovacancies	Nieminen and Manninen	[38]
$\tau_{d,theo}$ [ps]	Defect type	Author	Reference
296,6	Monovacancies	Cizek et al.	[44]
307	Monovacancies	Nieminen and Manninen	[38]
260 - 308[1]	Monovacancies	Campillo Robles et al.	[46]

[1] depending on the DFT-method used for calculation

3 Experimental

3.1 Materials: MgCaZn alloys

In the present study, high purity (Mg) magnesium was alloyed with zinc (Zn) and calcium (Ca) to synthesize an alloy with the composition Mg-0.45 wt%Zn-0.45 wt%Ca (ZX00). The samples were supplied by the group of A. M. Weinberg[11]. After solution and ageing-treatments, the alloy was indirectly extruded at 325 °C. Compared to direct extrusion, where the alloy billet is pushed through a fixed container, in the indirect extrusion process the die is pushed into the container, which holds the fixed alloy billet.[51] Subsequently, disks with diameters of ca. 15 mm and thicknesses between 0.8−1.1 mm were cut. The as-received Mg-alloy discs were subjected to HPT-straining at room temperature with 0.2 revolutions per minute and a total of 10 revolutions with a nominal pressure of approximately 2.6 GPa. HPT-deformation was done at the ESI Leoben. The HPT-deformed Mg-alloy discs exhibited thicknesses between 0.4−0.9 mm. The as-received Mg-alloy discs as well as the HPT-treated alloy discs were cut in 4 pieces and kept in a vacuum-desiccator, with silica gel as desiccant.

3.2 PALS for ex-situ corrosion measurements

3.2.1 Stepwise corrosion procedure

For the in-vitro corrosion of the as-received Mg-alloy as well as for the HPT-deformed Mg-alloy, simulated body fluid (SBF) was used as corrosion medium. For the preparation of the SBF, a phosphate buffered saline tablet (Roti®fair PBS 7.4) was dissolved in 200 ml highly pure water (ROTIPURAN® p.a., ACS). Two samples were immersed in SBF for 12 s up to 48 h in separate beaker glasses, such that the samples were leaned on the side wall of the beaker glass and most of the surface is accessible for the solution. After immersion, the samples were rinsed with distilled water and subsequently dried in a desiccator for 2 − 3 h. After drying, the mass change was determined and ex-situ PALS measurements were performed, as described in the following. After each immersion step, the SBF was renewed for both samples.

3.2.2 PALS setup, spectra pre-processing and analyzation

The PALS investigations were performed using a fast-fast positron lifetime spectrometer as described in 2.4.5. As high power voltage supply, a Canberra 3002D was used to operate the detector unit consisting of Hamatsu H2431-50 photomultipliers and scintillator crystals. For signal processing, ORTEC 583B constant fraction discriminators, ORTEC DB463 delay box, and a ORTEC 566 time-to-amplitude converter were used as well as a multi-channel analyzer with 12.37 ps/channel for a conversion gain of 2048 channels. The connection between these elements was established by $50\,\Omega$ BNC cables.

After drying and weighting of the as-received and corroded as-received Mg-alloy as well as the HPT-deformed Mg-alloy, the samples were mounted in the spectrometer in a sandwich geometry, as illustrated in Fig. 19. As positron source, ^{22}Na (NaCl salt) on a Al carrier foil with thickness of 5 µm was used.

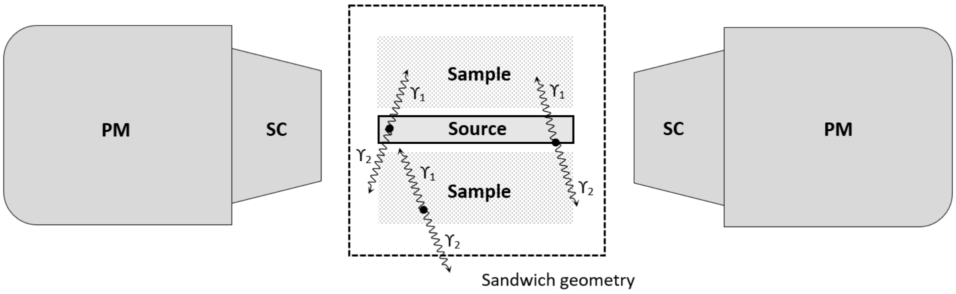

Figure 19: Schematic of the detection setup used for PALS. The sandwich geometry consists of two, at best, identically magnesium alloy samples with the foil ^{22}Na-source in between. The sandwich is placed horizontally, with the detector unit consisting of scintillator crystals and photomultiplier in close proximity. Redrawn after Puff[52].

A series of half hour spectra were measured at room temperature with at least 10^6 annihilation events gathered in total per sample pair. For these short time spectra, the first momentum was calculated. Only spectra with their first momentum within half a channel width were used for further analysis. The half hour spectra were subsequently summed up in a single spectrum, which was then utilized for numerical analysis. The resolution function and occurring source contributions as well as the positron function were obtained using PALS*fit*[53]. To obtain the resolution function of the spectrometer, a well known reference sample (annealed Al) was measured and the occurring positron lifetimes determined. For this purpose, a sum of three Gaussians with intensities 90/5/5 was chosen, as shown in Tab. 3, and a three-component fit conducted. The resulting bulk positron lifetime of Al was determined as $\tau_B = 164.0\,\mathrm{ps}$, which is in good agreement with literature[46]. The source correction resulting from annihilation in the source (NaCl-crystals and Al-foil) was determined using annealed Mg as reference sample. This resulted in a better fit quality in the following component analysis of the extruded and HPT-deformed Mg-alloy. Again, three-component fits were conducted and the source contributions determined, as shown in Tab. 4.

Table 3: Resolution function of the spectrometer (Full Width at Half Maximum $FWHM$, intensity I_G, and shift Δ of the Gaussians) obtained from numerical spectra analysis by *PALSFit*.

$FWHM$ [ps]	I_G [%]	Δ [ps]
167.1	90	0.0
104.2	5	42.4
94.0	5	−34.4

Table 4: Fitted component analysis (τ_i,I_i) of annealed Mg with a fit quality of χ^2 obtained from numerical spectra analysis by *PALSfit* to determine the source correction of the spectrometer.

τ_{Mg} [ps]	I_{Mg} [%]	τ_{Source_1} [ps]	I_{Source_1} [%]	τ_{Source_2} [ps]	I_{Source_2} [ps]
$224,8 \pm 2,8$	$80,5 \pm 3,0$	$408,4 \pm 26,8$	$16,3 \pm 2,8$	$1508,1 \pm 58,5$	$3,2 \pm 0,2$

The contribution from the source consists of two components, a long positronium lifetime stemming from annihilation on the Al-foil surface, and a shorter positron lifetime stemming from annihilation in the NaCl-crystals, as well as the Al-foil of the source. These source contributions were subtracted from the spectra in order to determine positron lifetimes ascribed to the measured samples exclusively. The positron functions and the resulting positron lifetimes and intensities of the extruded as well as the HPT-deformed Mg-alloy were determined using the resolution function and the source correction analyzed from the annealed Mg samples.

3.3 EIS for in-situ corrosion measurements

EIS spectra were recorded using a AUTOLAB AUT85934 potentiostat with a FRA32M EIS module from METROHM. The Mg-alloy samples were prepared by grinding and subsequently washing with ethanol. Afterwards, the samples were contacted to a gold wire with commercial conduct silver. After drying for at least 2 h, the gold wire, wetted with conduct silver, was covered and sealed with two-component epoxy glue (Uhu Plus Schnellfest) in order to ensure a stable contact and avoid exposure of this area to the solution. The subsequent electrochemical measurements were performed utilizing a quasi three-electrode electrochemical cell at room temperature, as schematically illustrated in Fig. 20. Therefore, the magnesium alloy samples were used as working electrode (WE) in such a way, that the capping glue was not in contact with the SBF used as electrolyte (EL); approximately half of the sample was immersed. As reference electrode (RE), an Ag/AgCl in 3M-KCl second order electrode was used with a standard electrochemical potential of 198 mV compared to the standard hydrogen electrode (SHE).[16] Parallel coupled to the Ag/AgCl RE, a 1 µF capacitance was connected in series to a Pt-wire, as recommended by the RE manufacturer. This additional capacitance parallel to the RE reduces artefacts due to the high impedance of the standard reference electrode at high frequencies[54]. As counter electrode (CE), a coiled Pt-wire was used to provide a sufficient area of the electrode. In order to reduce the decrease in SBF-level in the beaker glass and, therefore, of the immersed area of the samples, the beaker glass was sealed with Parafilm and the immersed electrodes were passed through small holes punctured in the film.

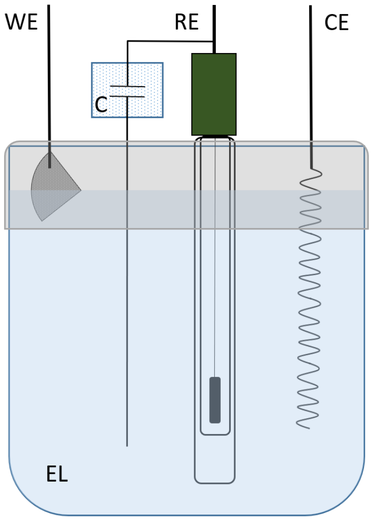

Figure 20: Schematic of the electrochemical cell used for EIS. The test specimen was used as working electrode (WE). The Ag/AgCl reference electrode (RE) was connected to a capacitor with 1 µF and a Pt wire. As counter electrode (CE) a coiled Pt wire was used. The electrodes were immersed in SBF, which was utilized as electrolyte (EL). The beaker glass was capped with Parafilm.

The EIS spectra were measured for various immersion times at the current open circuit potential (OCP) determined before initiating the respective measurement. The first spectrum was recorded with a delay time of 10 min in order to reach a reasonable steady OCP.

All EIS scans were recorded in a frequency range from 100 kHz to 0.001 Hz in 50 logarithmic frequency steps and a 0.01 V single sine amplitude. The measured spectra were analyzed using NOVA 1.11.

4 Results

In the following chapter, PALS spectra of the as-received Mg-alloy and HPT-deformed Mg-alloy are analyzed in the as-received condition and after in-vitro corrosion by immersion in SBF to obtain a deeper understanding of the influence of severe plastic deformation on the microstructure and on the development of the structural defects in both magnesium alloys arising from corrosion. Since microstructure has a major impact on the corrosion behaviour of magnesium alloys, EIS spectra of the two alloys are compared and analyzed using equivalent circuits in order to get an in-situ insight on predominant surface reactions occurring during corrosion.

PALS spectra were recorded in the as-received condition as well as after 12 s, 60 s, 5 min, 25 min, 2 h, 10 h, 24 h, and 48 h of in-vitro corrosion by immersion for the as-received as well as the HPT-deformed Mg-alloy.

The complementary EIS spectra were recorded at the reasonably stable OCP present before initiating each respective measurement. The impedance spectra were conducted after the initial immersion with a delay of 10 min as well as after 2 h, 4 h, 6 h, 8 h, 24 h, 29.5 h/30 h, and 48 h of in-vitro corrosion.

4.1 PALS on as-received Mg-alloy

In Fig. 21, the measured spectrum for the as-received Mg-alloy as well as the spectra after 25 min, 10 h, and 48 h of immersion are shown. The form of the spectra has not changed significantly due to the immersion, meaning that the corrosion was less pronounced and consequently additional structural defects developed only to a small extent with respect to the as-received condition of the alloy.

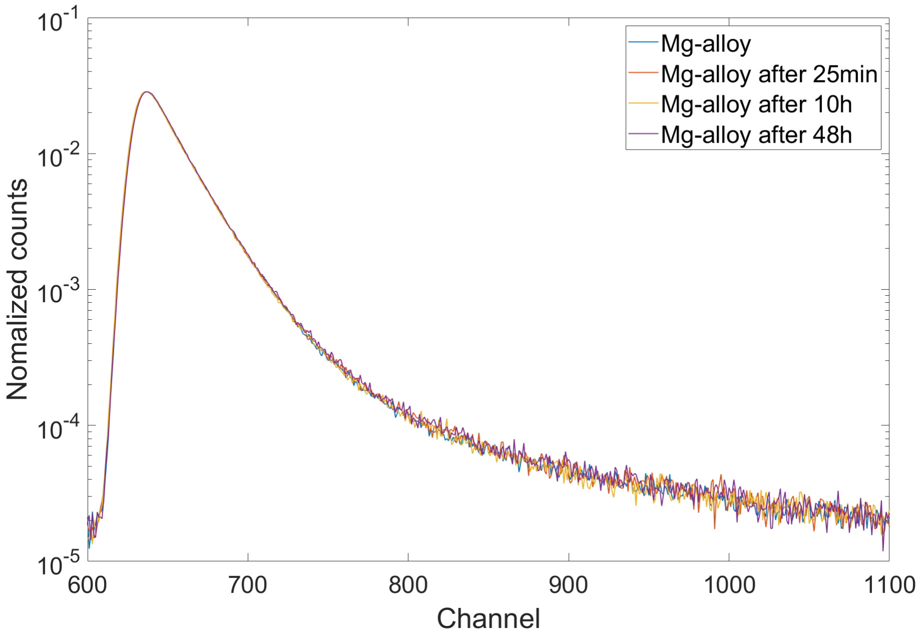

Figure 21: Comparison of PALS spectra of as-received Mg-alloy in as-received condition and after in-vitro corrosion by immersion in SBF for 25 min, 10 h, and 48 h.

The measured spectra were analyzed using two component positron fits. The obtained positron lifetimes τ_i and intensities I_i as well as the mean positron lifetime τ_{mean} and the fit quality χ^2 obtained by *PALSfit* are listed in Tab. 5. The development of the lifetime components and their intensities dependent on the corrosion time is depicted in Fig. 22. For 0 s, 12 s, and 60 s of immersion, the mean lifetime τ_{mean} is plotted for τ_1, since the splitting of the positron lifetimes is inconclusive for these short immersion times. Additionally, τ_1 is strongly reduced for short immersion times up to 60 s and subsequently approaches similar values as τ_{mean} for longer immersion times. Therefore, it is appropriate to plot τ_{mean} up to 60 s of immersion in order to clearly visualize subtle differences in τ_1 for longer immersion times.

Table 5: Mean positron lifetime τ_{mean} and component analysis (τ_i,I_i) for in-vitro corrosion of the as-received Mg-alloy after immersion in SBF with a fit quality of χ^2 obtained from numerical spectra analysis by *PALSfit*. (f) denotes for the fixed positron lifetimes during the analysis.

Corrosion time	τ_1 [ps]	I_1 [%]	τ_2 [ps]	I_2 [%]	τ_{mean} [ps]	χ^2
0 s	201 ± 22	$41,1 \pm 35,8$	254 ± 17	$58,9 \pm 35,8$	231.8 ± 0.3	1.012
12 s	198 ± 4	$40,3 \pm 3,2$	254 (f)	$59,7 \pm 3,2$	$231,4 \pm 0.3$	1.045
60 s	190 ± 4	34.3 ± 2.3	254 (f)	$65,7 \pm 2.2$	231.8 ± 0.3	1.074
5 min	228 ± 1	98.1 ± 0.7	506 ± 67	1.9 ± 0.7	232.8 ± 0.3	0.945
25 min	229 ± 1	98.8 ± 0.2	903 ± 79	1.2 ± 0.2	237.1 ± 0.6	0.998
2 h	229 ± 1	98.8 ± 0.2	890 ± 78	1.2 ± 0.2	237.1 ± 0.6	0.991
10 h	228 ± 1	97.8 ± 0.8	504 ± 70	2.2 ± 0.8	233.5 ± 0.4	1.010
24 h	229 ± 1	98.6 ± 0.3	673 ± 69	1.4 ± 0.3	234.6 ± 0.4	1.100
48 h	229 ± 1	98.5 ± 0.2	886 ± 65	1.5 ± 0.2	239.4 ± 0.6	1.097

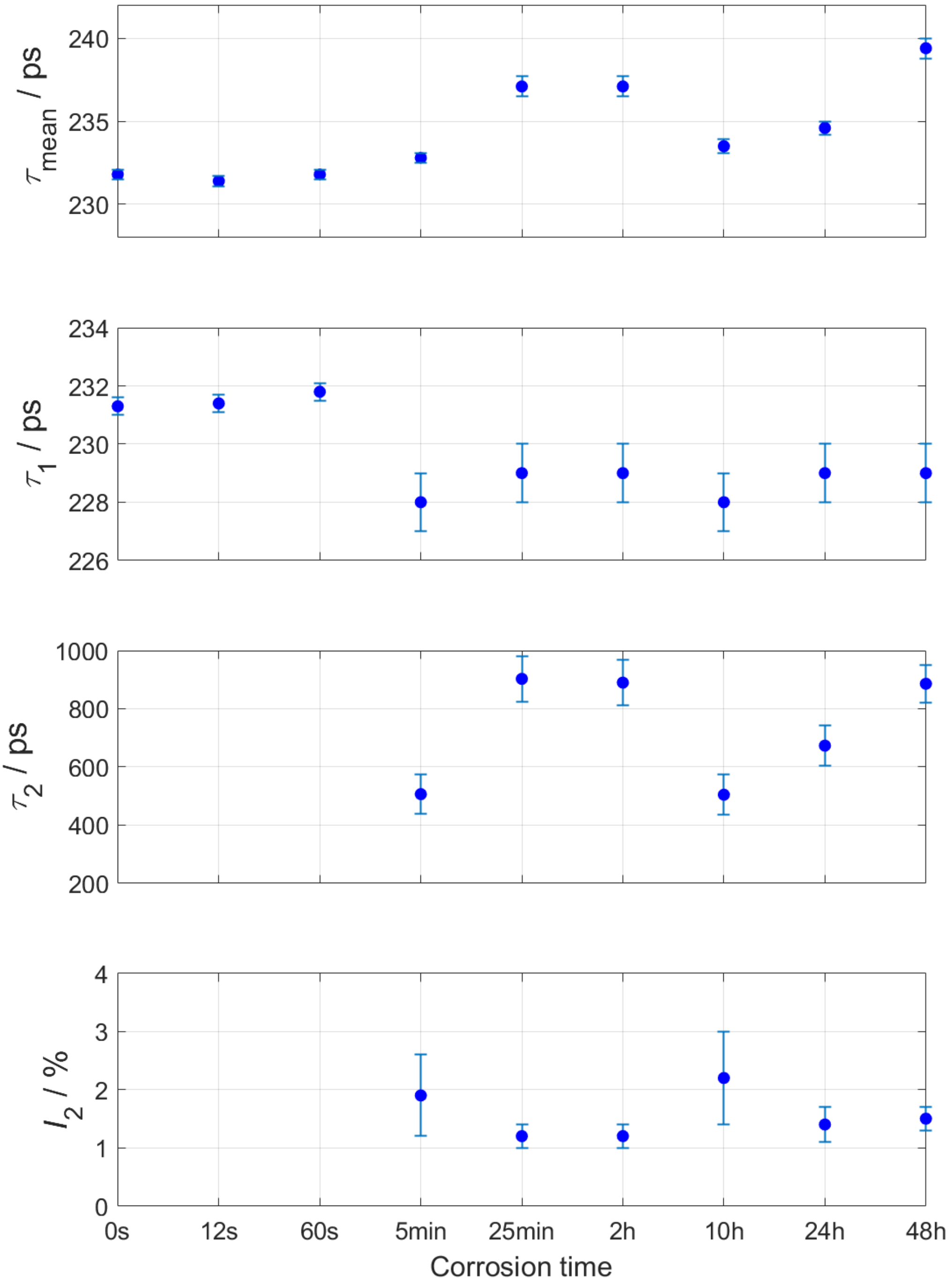

Figure 22: Mean positron lifetime τ_{mean} and component analysis (τ_i,I_i) of the as-received Mg-alloy after in-vitro corrosion by immersion in SBF (see Tab. 5).

The mean positron lifetime τ_{mean} is the most stable and meaningful parameter determined in the fitting procedure. For the as-received Mg-alloy, τ_{mean} is obtained as (231.8 ± 0.3) ps and remained approximately constant after the first initial in-vitro corrosion of 12 s with (231.4 ± 0.3) ps. With increasing corrosion time, τ_{mean} increased steadily up to (237.1 ± 0.6) ps for 25 min and 2 h, respectively. After 10 h of immersion, τ_{mean} decreased to (233.5 ± 0.4) ps and rose again to (239.4 ± 0.6) ps after 48 h.

Considering the component analysis of the positron fits, the mean positron lifetime τ_{mean} can be split up in a reduced bulk positron lifetime τ_1 (201 ± 22) ps and a defect lifetime τ_2 of (254 ± 17) ps with intensities I_1 and I_2 of (41.1 ± 35.8) % and (58.9 ± 35.8) %, respectively. The high estimated error of I_1 and I_2 is caused by the correlation between both intensities. Since τ_{mean} remained approximately constant up to 60 s of immersion, the defect positron lifetime τ_2 was fixed at 254 ps in order to reach a comparable analysis of the spectra. Therefore, a reduced bulk positron lifetime τ_1 (198 ± 4) ps with intensities I_1 and I_2 of (40.3 ± 3.2) % and (59.7 ± 3.2) %, respectively, were determined after 12 s of in-vitro corrosion. After 60 s of immersion, τ_1 as well as I_1 further decreased with (190 ± 4) ps and (34.3 ± 2.3) %, whereas the defect intensity I_2 further increased with (65.7 ± 2.2) %. The defect positron lifetime τ_2 increases significantly with longer immersion time from (506 ± 67) ps after 5 min to (903 ± 79) ps after 25 min and (890 ± 78) ps after 2 h, respectively. Thereby, the intensity I_2 decreased from (1.9 ± 0.7) % after 5 min to (1.2 ± 0.2) % after 25 min and 2 h, respectively. The first positron lifetime component τ_1 remained approximately constant within the error margin with (228 ± 1) ps with a dominant, high intensity of (98.1 ± 0.7) % after 5 min up to 48 h of in-vitro corrosion. The trend of the mean positron lifetime τ_{mean} is predominantly determined by the development of τ_2, since the change in τ_1 is insignificant. After 10 h of in-vitro corrosion, τ_2 decreased again down to (504 ± 70) ps with an increased intensity I_2 of (2.2 ± 0.8) %. For longer immersion times, τ_2 increased again up to (886 ± 65) ps after 48 h. The associated intensity I_2 in the defects decreased and remained nearly constant after 24 h and 48 h.

The development of the mass due to the in-vitro corrosion is listed for both as-received Mg-alloy samples (m_i, $i = 1, 2$) used in the PALS setup in Tab. 6 and is depicted in Fig. 23.

Table 6: Masses of the as-received Mg-alloy positron annihilation sample pair (m_1, m_2, $m_{ges} = m_1+m_2$) after in-vitro corrosion by immersion in SBF estimated from mass change. The error was estimated using the standard deviation of five measurements.

Corrosion time	m_1 [mg]	m_2 [mg]	m_{ges} [mg]
0 s	104.574 ± 0.004	111.726 ± 0.004	216.300 ± 0.003
12 s	104.565 ± 0.003	111.713 ± 0.003	216.278 ± 0.006
60 s	104.553 ± 0.002	111.699 ± 0.002	216.252 ± 0.003
5 min	104.598 ± 0.003	111.726 ± 0.002	216.324 ± 0.004
25 min	104.809 ± 0.001	111.936 ± 0.001	216.745 ± 0.002
2 h	104.827 ± 0.001	112.057 ± 0.002	216.884 ± 0.002
10 h	104.963 ± 0.002	112.070 ± 0.001	217.033 ± 0.003
24 h	105.260 ± 0.006	112.216 ± 0.005	217.476 ± 0.010
48 h	105.135 ± 0.002	112.141 ± 0.002	217.276 ± 0.004

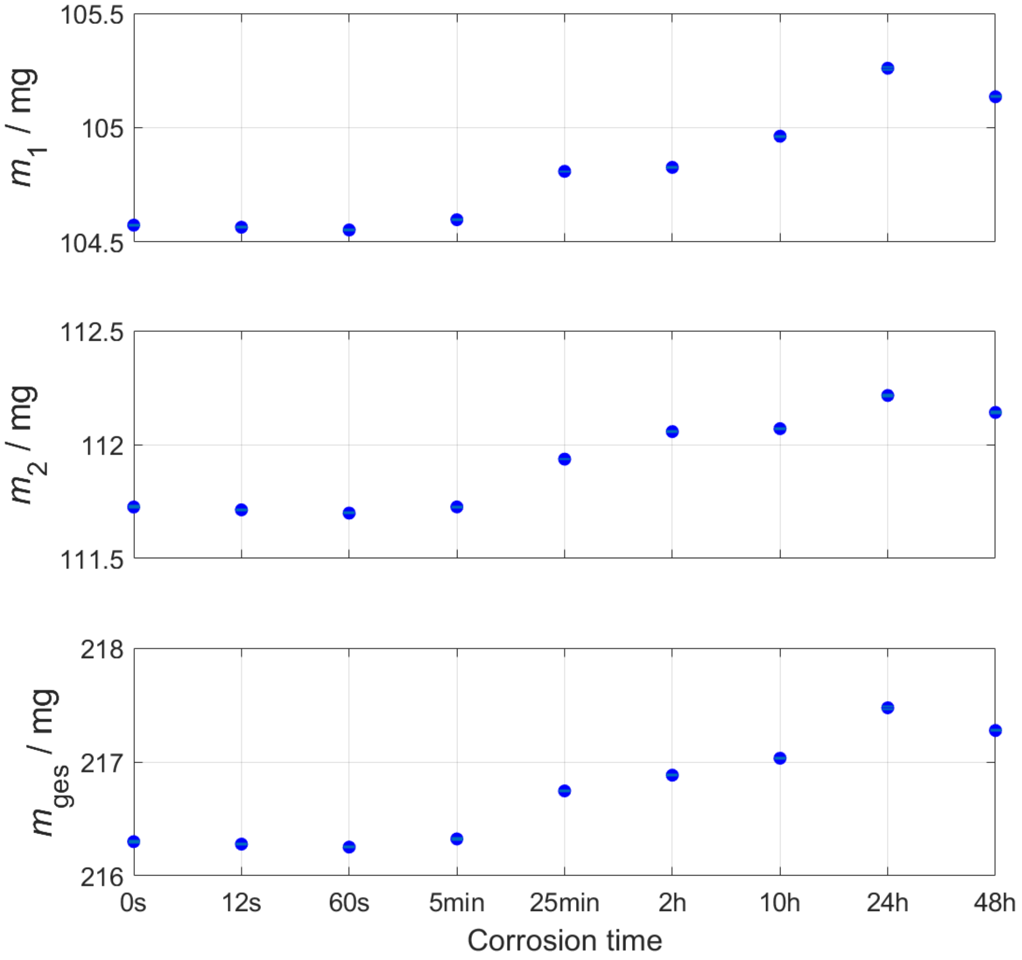

Figure 23: Development of the mass of the as-received Mg-alloy sample pair after in-vitro corrosion by immersion in SBF (see Tab. 6).

For very short immersion times, the total mass m_{ges} reduced from $(216.300 \pm 0.003)\,\mathrm{mg}$ in the as-received condition (0 s) to $(216.252 \pm 0.003)\,\mathrm{mg}$ after 60 s of in-vitro corrosion. Both samples steadily increased their mass for increasing immersion time up to a total mass of $(217.476 \pm 0.010)\,\mathrm{mg}$ after 24 h with the highest mass increase between 5 min and 25 min. After 48 h of immersion, a first reduction of mass is obtained. Since the total mass steadily increased with corrosion time, the development of corrosion products coating the surface is predominant with only weak dissolution of the as-received Mg-alloy.

From the development of the mass, the surface layer thickness of the positron annihilation sample pair (d_i, $i = 1, 2$) was estimated using a very simplified model of the surface bilayer structure. It was presumed, that the change in mass is caused solely by the deposition of $Mg(OH)_2$ as only corrosion product formed on the Mg-alloy surface, and that the underlying Mg matrix is not dissolving. Additionally, it was presumed that there is no initial MgO layer present on the Mg-alloy and other phases incorporated into the surface film are neglected. Therefore, the mass m_i of the as-received Mg-alloy samples after each corrosion step can be written as sum of the mass of the uncorroded Mg, m_{Mg}, and the mass of the corrosion product layer, $m_{Mg(OH)_2}$, as

$$m_i = m_{Mg} + m_{Mg(OH)_2} = \left(\frac{m_0}{M_{Mg}} - x_i\right) + x_i(M_{Mg} + 2M_H + 2M_O) = m_0 + 2x_i(M_H + M_O) \ , \tag{68}$$

where m_0 is the initial mass of the bare Mg and x_i is the number of moles of corroded Mg. M_H, M_O and M_{Mg} denote the mole masses of hydrogen, oxygen and magnesium, respectively. From Eq. (68), the number of moles x_i of corroded Mg was calculated. With x_i, the mass $m_{Mg(OH)_2}$ of the $Mg(OH)_2$ corrosion product layer can be determined as described in (68). The layer thicknesses were then estimated using

$$d = \frac{V_{Mg(OH)_2}}{A} \ , \tag{69}$$

where $V_{Mg(OH)_2}$ is the volume of the corroded surface layer resulting from $m_{Mg(OH)_2}$, and A is the area of the immersed sample. Since the mass of the as-received Mg-alloy samples decreased after the initial corrosion up to 60 s of immersion (see Tab. 6), the mass after

60 s was presumed to be the initial mass m_0. The estimated surface layer thicknesses d_i are listed in Tab. 7. The development of the mean surface layer thickness d_{mean} dependent on immersion time is depicted in Fig. 24.

Table 7: Surface layer thickness of the as-received Mg-alloy sample pair after in-vitro corrosion by immersion in SBF estimated from mass change (acc. to eq. (69)).

Corrosion time	d_1 [µm]	d_2 [µm]	d_{mean} [µm]
5 min	0.28 ± 0.04	0.17 ± 0.03	0.22 ± 0.03
25 min	1.60 ± 0.08	1.47 ± 0.08	1.53 ± 0.07
2 h	1.70 ± 0.09	2.22 ± 0.11	1.96 ± 0.09
10 h	2.54 ± 0.13	2.30 ± 0.11	2.42 ± 0.11
24 h	4.38 ± 0.22	3.20 ± 0.17	3.80 ± 0.19
48 h	3.61 ± 0.17	2.74 ± 0.14	3.17 ± 0.15

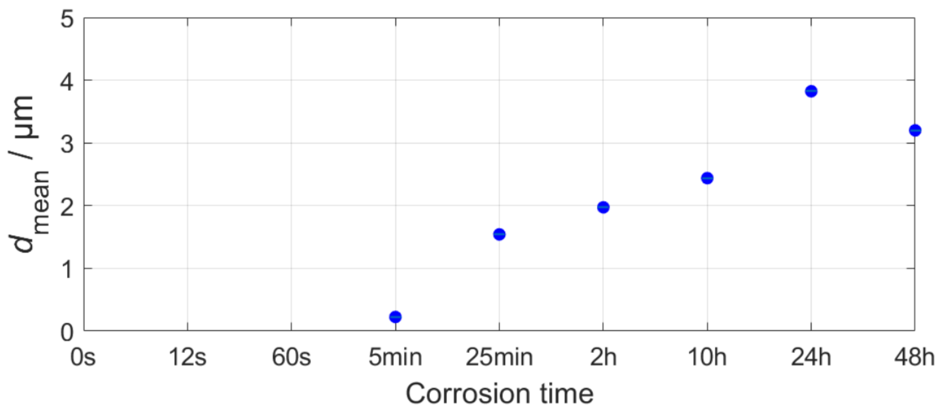

Figure 24: Mean surface layer thickness of the as-received Mg-alloy sample pair after in-vitro corrosion by immersion in SBF estimated from mass change (see Tab. 7).

The mean thickness d_{mean} of the $Mg(OH)_2$ corrosion product layer increases with immersion time from (0.22 ± 0.03) µm to (3.80 ± 0.19) µm. From this estimated surface layer thickness, the intensity I_{d_i} of positrons in the growing corrosion product layer can be estimated using Eq. (65) and (64) as

$$I_{d_i} = 1 - \exp\left(-\frac{\rho_{Mg(OH)_2}}{25\,\mathrm{mg\,cm^{-2}}} d_i\right) \tag{70}$$

with the surface layer thickness d_i, and the density $\rho_{Mg(OH)_2} = 2360\,\mathrm{mg\,cm^{-3}}$[55] of $Mg(OH)_2$. The resulting fractions of positrons annihilating in the surface layer are listed in Tab. 8, and the development of the mean positron intensity $I_{d_{mean}}$ dependent on immersion time is depicted in Fig. 25.

Table 8: Fraction of positrons annihilating in the surface layer of the as-received Mg-alloy sample pair after in-vitro corrosion by immersion in SBF (acc. to eq. (70)).

Corrosion time	I_{d_1} [%]	I_{d_2} [%]	$I_{d_{mean}}$ [%]
5 min	0.26 ± 0.04	0.16 ± 0.03	0.21 ± 0.03
25 min	1.49 ± 0.08	1.38 ± 0.07	1.43 ± 0.07
2 h	1.59 ± 0.08	2.07 ± 0.11	1.83 ± 0.09
10 h	2.37 ± 0.12	2.14 ± 0.10	2.26 ± 0.11
24 h	4.05 ± 0.21	2.98 ± 0.16	3.52 ± 0.18
48 h	3.35 ± 0.16	2.55 ± 0.13	2.95 ± 0.14

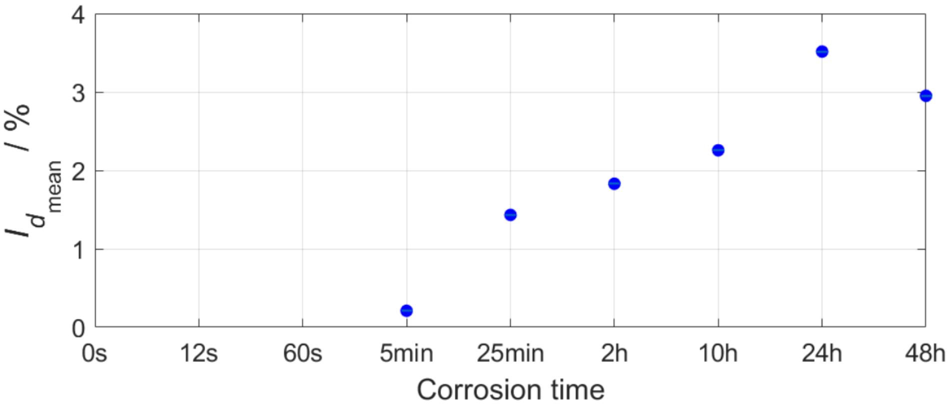

Figure 25: Fraction of positrons annihilating in the surface layer of the as-received Mg-alloy after in-vitro corrosion by immersion in SBF (see Tab. 8).

$I_{d_{mean}}$ estimated in this way increases from $(0.21 \pm 0.03)\,\%$ to $(3.52 \pm 0.18)\,\%$ increasing with immersion time.

4.2 PALS on HPT-deformed Mg-alloy

In Fig. 26, the measured spectrum for the as-received HPT-deformed Mg-alloy as well as the spectra after 25 min, 10 h, and 48 h of immersion are shown. Compared to the as-received Mg-alloy, the form of the spectra changed considerably due to the in-vitro corrosion. The spectra increasingly flattened with increasing immersion time, which is a clear indication of a significant enlargement of open-volume defects with stronger trapping ability and accompanied with an increasing defect concentration in the HPT-deformed Mg-alloy.

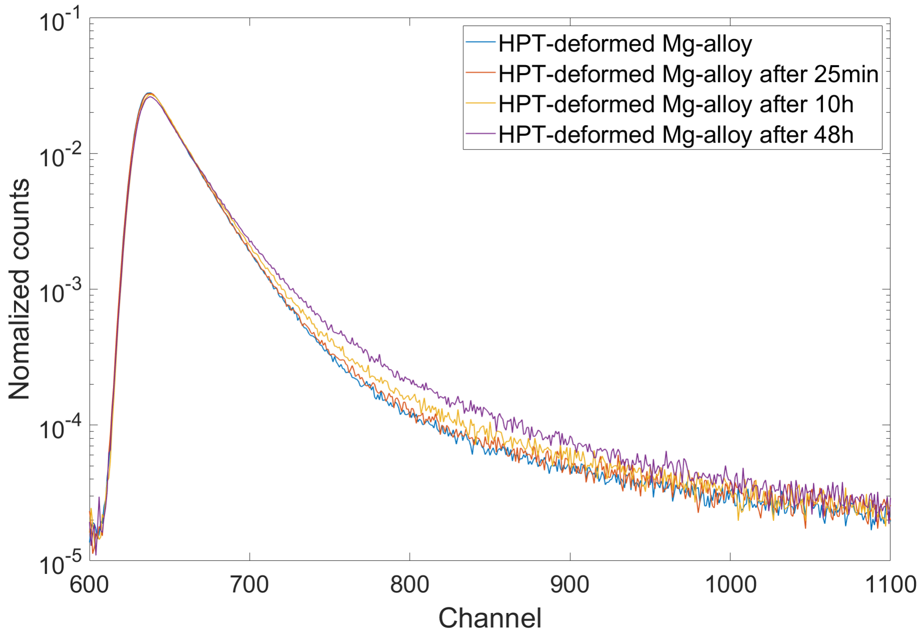

Figure 26: Comparison of PALS spectra of HPT-deformed Mg-alloy in as-received condition and after in-vitro corrosion by immersion in SBF for 25 min, 10 h, and 48 h.

The measured spectra were analyzed applying single-, two-, and three-component positron fitting. The obtained positron lifetimes τ_i and intensities I_i as well as the mean positron lifetime τ_{mean} and the fit quality χ^2 obtained by *PALSfit* are listed in Tab. 9. The development of the lifetime components and intensities dependent on the corrosion time is depicted in Fig. 27.

Table 9: Mean positron lifetime τ_{mean} and component analysis (τ_i,I_i) for in-vitro corrosion of HPT-deformed Mg-alloy after immersion in SBF with a fit quality of χ^2 obtained from numerical spectra analysis by *PALSfit*.

Corrosion time	τ_1 [ps]	I_1 [%]	τ_2 [ps]	I_2 [%]	τ_3 [ps]	I_3 [%]	τ_{mean} [ps]	χ^2
0 s	241.4 ± 0.3	100					241.4 ± 0.3	1.025
12 s	241.4 ± 0.3	100					241.4 ± 0.3	1.047
60 s	239.5 ± 0.5	99.6 ± 0.1	1500 ± 206	0.44 ± 0.06			245.1 ± 0.7	0.998
5 min	239.8 ± 0.4	99.7 ± 0.1	2180 ± 429	0.35 ± 0.04			246.6 ± 1.5	1.101
25 min	240.5 ± 0.4	99.1 ± 0.1	1663 ± 129	0.92 ± 0.06			253.6 ± 1.0	1.019
2 h	241.8 ± 0.4	99.0 ± 0.1	1408 ± 89	1.01 ± 0.07			253.5 ± 0.7	1.062
10 h	242.1 ± 1.1	94.8 ± 0.6	686 ± 82	4.41 ± 0.48	2514 ± 688	0.8 ± 0.2	279.4 ± 3.3	1.033
24 h	241.5 ± 0.8	92.6 ± 0.5	687 ± 47	6.22 ± 0.30	2052 ± 290	1.2 ± 0.3	290.3 ± 1.4	1.152
48 h	239.1 ± 2.1	85.0 ± 1.5	573 ± 52	12.04 ± 1.08	1590 ± 157	3.0 ± 0.6	319.4 ± 1.4	0.937

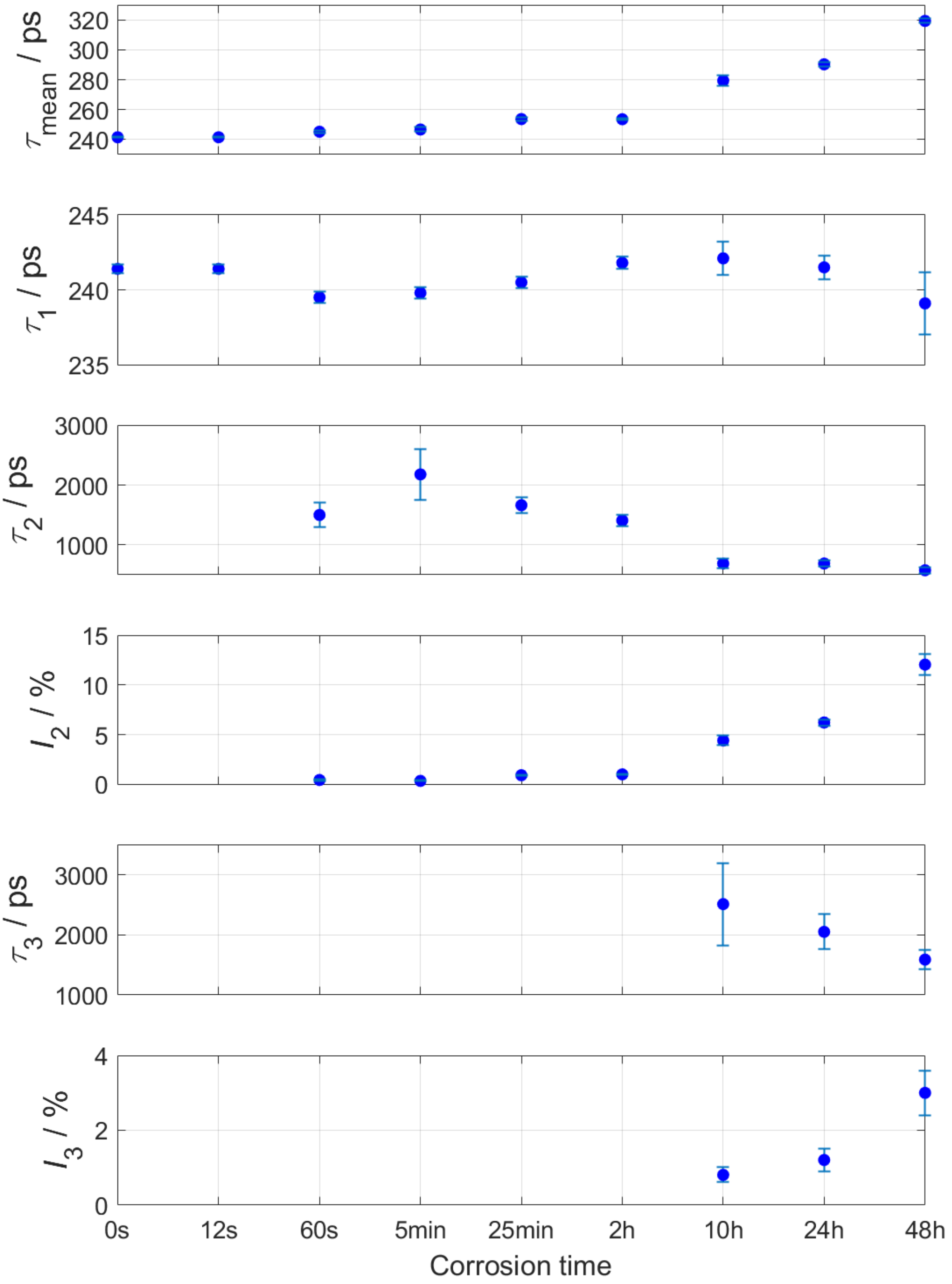

Figure 27: Mean positron lifetime τ_{mean} and component analysis (τ_i,I_i) of the HPT-deformed Mg-alloy after in-vitro corrosion by immersion in SBF (see Tab. 9).

The mean positron lifetime τ_{mean} of the as-received HPT-deformed Mg-alloy as well as after 12 s of immersion was obtained as (241.3 ± 0.3) ps and is significantly higher compared to the extruded alloy. With increasing corrosion time, τ_{mean} increased steadily up to (253.6 ± 1.0) ps after 25 min. After 2 h of immersion, τ_{mean} remained approximately constant before the major onset of τ_{mean} after 10 h. After 48 h, τ_{mean} increased strongly to (319.4 ± 1.4) ps, indicating a severe corrosion damage and development of large open-volume defects.

Compared to as-received Mg-alloy samples, the spectrum after HPT-deformation could be fitted using a single lifetime component τ_1 of (241.4 ± 0.3) ps in the as-received condition (0 s) and after the initial in-vitro corrosion of 12 s. After 60 s of in-vitro corrosion, a long second positron lifetime component τ_2 arises with (1500 ± 206) ps and a small intensity of (0.44 ± 0.06) %. The first positron lifetime τ_1 remained again constant within the error margin up to 48 h of in-vitro corrosion. After 5 min of immersion, τ_2 increased significantly with (2180 ± 429) ps and the corresponding intensity I_2 decreased slightly with (0.35 ± 0.06) %. With increasing immersion time up to 2 h, the second defect positron lifetime τ_2 decreased, whereas the intensity I_2 rapidly increased. After 10 h of in-vitro corrosion by immersion, the defect lifetime can be split up in two defect positron lifetimes τ_2 and τ_3 with (686 ± 82) ps and (2514 ± 688) ps, respectively, and associated intensities I_2 and I_3 of (4.41 ± 0.48) % and (0.8 ± 0.2) %. After 48 h of in-vitro corrosion, the contribution of the first positron lifetime τ_1 reached its lowest intensity with (85.0 ± 1.5) % with $\tau_1 = (239.1 \pm 2.1)$ ps. The first defect positron lifetime τ_2 decreased to (573 ± 52) ps with an increased intensity of (12.04 ± 1.08) %, whereas the second defect positron lifetime τ_3 exhibits a similar trend. The positron lifetime decreased significantly and the corresponding intensity increased.

The development of the mass due to the in-vitro corrosion for both HPT-deformed Mg-alloy samples (m_i, $i = 1, 2$) used in the PALS setup is shown in Tab. 10 and Fig. 28.

Table 10: Masses of the HPT-deformed Mg-alloy positron annihilation sample pair (m_1, m_2, $m_{ges} = m_1 + m_2$) after in-vitro corrosion by immersion in SBF estimated from mass change. The error was estimated using the standard deviation of five measurements.

Corrosion time	m_1 [mg]	m_2 [mg]	m_{ges} [mg]
0 s	51.982 ± 0.004	51.469 ± 0.002	103.360 ± 0.004
12 s	51.869 ± 0.003	51.451 ± 0.001	103.321 ± 0.003
60 s	51.872 ± 0.002	51.448 ± 0.002	103.320 ± 0.004
5 min	51.895 ± 0.002	51.476 ± 0.002	103.371 ± 0.004
25 min	52.064 ± 0.005	51.628 ± 0.001	103.692 ± 0.006
2 h	52.219 ± 0.006	51.869 ± 0.002	104.088 ± 0.006
10 h	51.102 ± 0.127	51.297 ± 0.017	102.399 ± 0.143
24 h	46.955 ± 0.042	48.922 ± 0.059	95.878 ± 0.098
48 h	43.971 ± 0.078	43.952 ± 0.072	87.923 ± 0.145

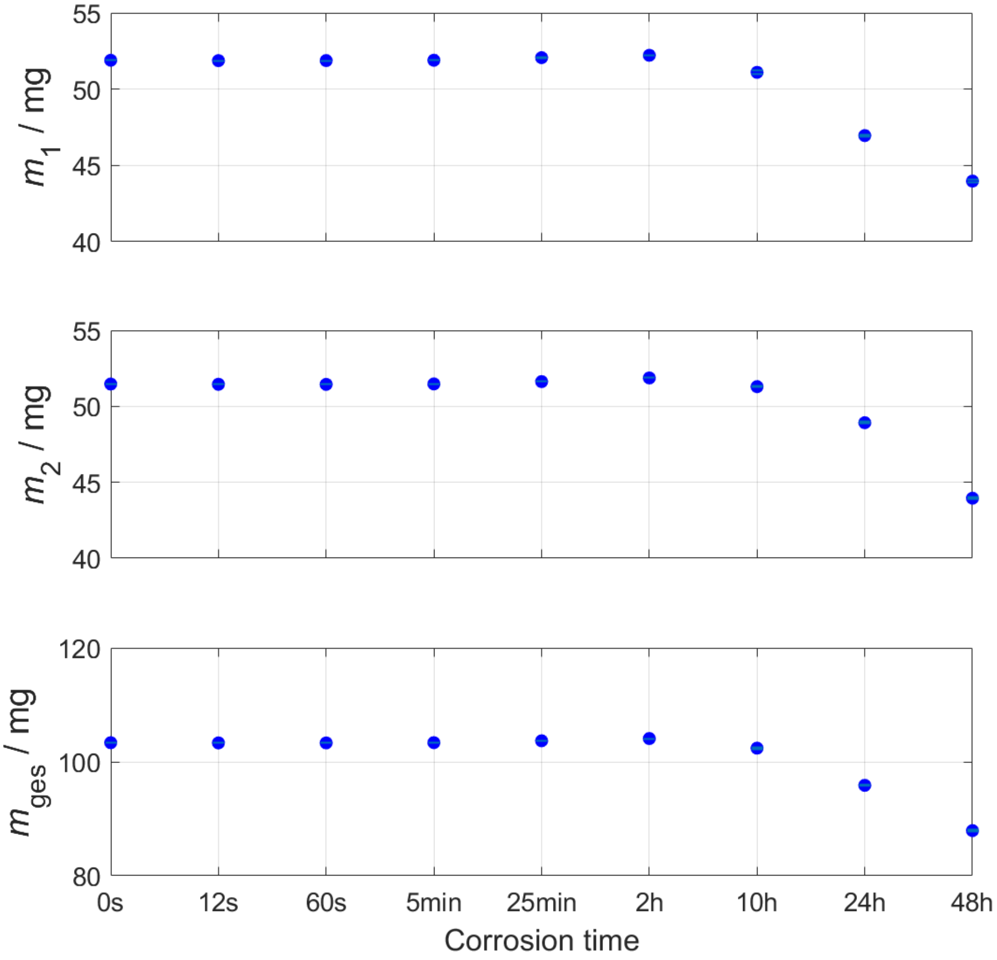

Figure 28: Development of the mass of the HPT-deformed Mg-alloy sample pair after in-vitro corrosion by immersion in SBF (see Tab. 10).

For very short immersion times up to 60 s, the total mass m_{ges} decreased for the HPT-deformed alloy (see Tab. 10) with (103.360 ± 0.004) mg in the as-received condition (0 s) to (103.320 ± 0.004) mg after 60 s of in-vitro corrosion. A similar mass decrease during the initial corrosion steps is obtained for the as-received Mg-alloy (see Tab. 6). The mass for both HPT-deformed samples increased with increasing immersion time up to a total mass of (104.088 ± 0.006) mg after 2 h of immersion. After 10 h of in-vitro corrosion, a rapid decrease of the mass for both samples set in reducing the total mass to (87.923 ± 0.145) mg indicating a strong dissolution of the HPT-deformed Mg-alloy.

From the development of the mass, the surface layer thicknesses (d_i, $i = 1,2$) were estimated using the simplified model of the surface bilayer structure described by Eq. (68) and Eq. (69). The estimated surface layer thicknesses d_i are listed in Tab. 11 and the development of the mean surface layer thickness d_{mean} with immersion time is depicted in Fig. 29. Applying eq. (69) would result in negative values of surface thicknesses for 10 h up to 48 h of immersion. This is due to the loss of mass after long immersion times. Here, the used model fails since it assumes that the increase in mass is solely associated with the growth of a $Mg(OH)_2$ layer whilst neglecting the dissolution of the underlying alloy.

Table 11: Surface layer thickness of the HPT-deformed Mg-alloy sample pair after in-vitro corrosion by immersion in SBF estimated from mass change (acc. to eq. (69)).

Corrosion time	d_1 [µm]	d_2 [µm]	d_{mean} [µm]
5 min	0.16 ± 0.03	0.20 ± 0.04	0.18 ± 0.03
25 min	1.36 ± 0.11	1.27 ± 0.08	1.31 ± 0.09
2 h	2.45 ± 0.16	2.98 ± 0.16	2.71 ± 0.15

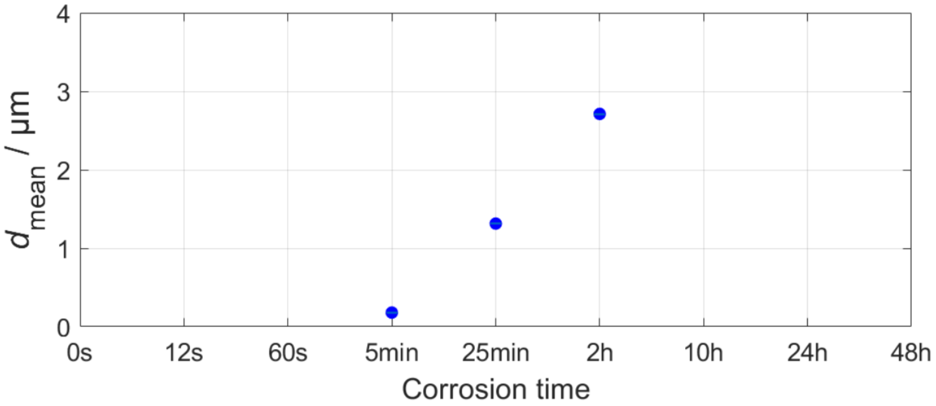

Figure 29: Mean surface layer thickness of the HPT-deformed Mg-alloy sample pair after in-vitro corrosion by immersion in SBF estimated from mass change (see Tab. 11).

The mean $Mg(OH)_2$ corrosion product layer thickness d_{mean} was estimated ranging from $(0.18 \pm 0.03)\,\mu m$ to $(2.71 \pm 0.15)\,\mu m$ increasing with immersion time. Compared to the as-received alloy (see Fig. 24), the thickness d_{mean} of the corrosion product layer increases more rapidly during in-vitro corrosion. From this estimated surface layer thickness, the fraction of positrons annihilating in the growing corrosion product layer I_{d_i} was estimated using Eq. (70). The resulting intensities in the surface layer are listed in Tab. 12 and the development of the mean intensity $I_{d_{mean}}$ with immersion time is depicted in Fig. 30.

Table 12: Fraction of positrons annihilating in the surface layer of the HPT-deformed Mg-alloy sample pair after in-vitro corrosion by immersion in SBF (acc. to eq. (70)).

Corrosion time	I_{d_1} [%]	I_{d_2} [%]	$I_{d_{mean}}$ [%]
5 min	0.15 ± 0.03	0.19 ± 0.04	0.17 ± 0.03
25 min	1.26 ± 0.10	1.18 ± 0.07	1.22 ± 0.08
2 h	2.26 ± 0.15	2.75 ± 0.15	2.51 ± 0.14

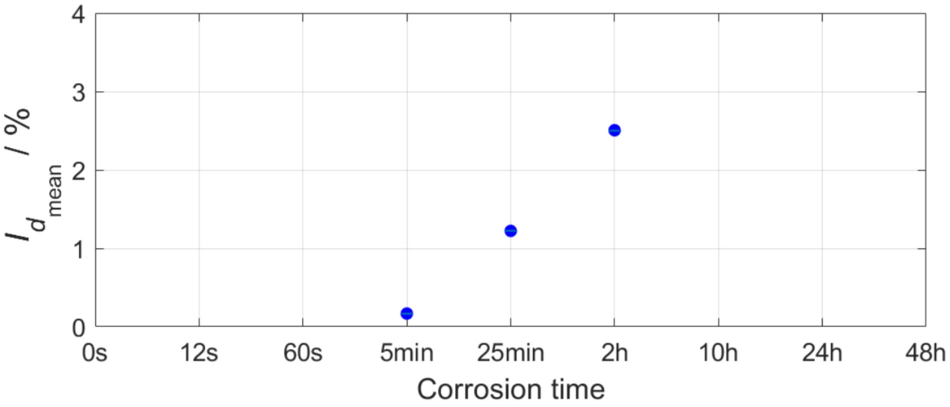

Figure 30: Fraction of positrons annihilating in the surface layer of the HPT-deformed Mg-alloy during in-vitro corrosion immersed in SBF (see Tab. 12).

$I_{d_{mean}}$ estimated in this way increases from (0.17 ± 0.03) % to (2.51 ± 0.14) % increasing with immersion time.

The drastic differences in the development of τ_{mean} and m_i (i = 1,2) with increasing immersion time are associated with obviously different corrosion rates for the extruded and HPT-deformed Mg-alloy (compare Fig. 22 and Fig. 27). The substantial rise of τ_{mean} accompanied with a decreasing mass indicate an increasingly strong corrosion damage of the HPT-deformed Mg-alloy, whereas the slower rise of τ_{mean} for the as-received Mg-alloy indicates a moderate corrosion damage, as can be compared by the photographs of the samples in Fig. 31. During the first hour of in-vitro corrosion, the as-received Mg-alloy changed steadily its appearance from silvery to increasingly dark grey in local areas associated with corroding regions. Differences in the local color of the surface and corroded area may be associated with differently active regions within the alloy as found by Liu et al.[27] for a Mg-1 wt%Ca alloy immersed in SBF. The surface was quickly covered by the corrosion product layer. After 24 h of immersion, loose white corrosion product precipitated on local spots at the surface and especially on the edges, which grew with increasing immersion time and the corroded surface area seemed to brighten up slowly in local areas. Compared to the as-received Mg-alloy, the HPT-deformed Mg-alloy hardly changed its appearance during the first hour of immersion, but excessive hydrogen blistering occurred on the surface. Already after 2 h of in-vitro corrosion, loose white corrosion product formed to a high extent on the surface and on the edges. With increasing immersion time, the precipitated white corrosion product covered the majority of the alloy surface. After 24 h of immersion, the surface was completely covered and a relatively large surface patch detached from the alloy, as shown in Fig. 32. The underlying alloy as well as the detached alloy patch surface were covered in corrosion product indicating that the corrosion already reached deeper into the alloy with corrosion product precipitating in subsurface regions. The edges of the HPT-deformed alloy experienced a high corrosion damage and crumbled partially away.

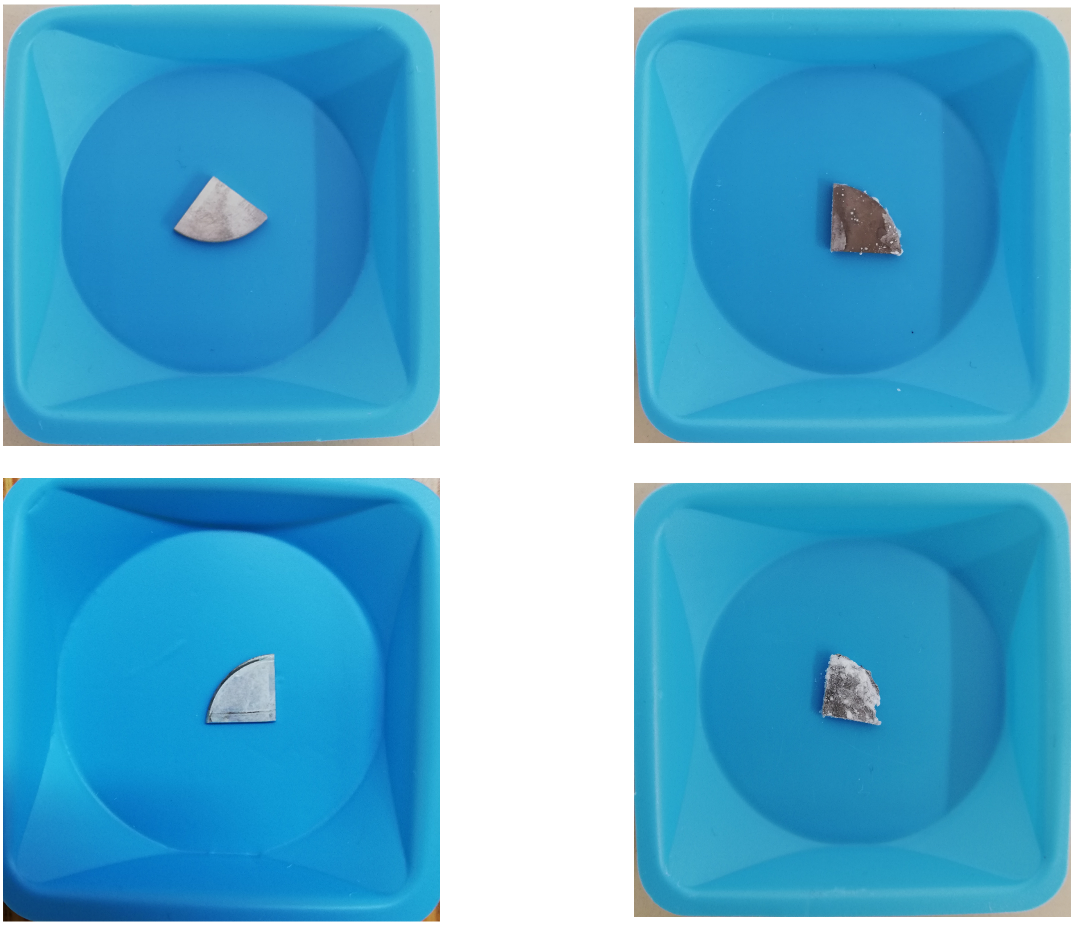

Figure 31: Photographs of the extruded (top) and the HPT-deformed (bottom) Mg-alloy sample in as-received condition and after 48 h of in-vitro corrosion in SBF (radius of the samples ca. 7.5 mm).

Figure 32: Photograph of a detached surface patch of the HPT-deformed Mg-alloy after 24 h of in-vitro corrosion in SBF (radius of the sample ca. 7.5 mm). Left: Patch as detached from the surface. Right: Corrosion products formed underneath the detached patch.

Fig. 33 shows optical microscopic images of extruded Mg-alloy in as-received condition. The surface of the as-received Mg-alloy was already covered with a visible MgO layer and already exhibits noticeable defects across its surface, which may result from the pretreatment. For the HPT-deformed Mg-alloy, the surface was less covered with an air-formed MgO layer (not shown). Fig. 34 shows optical microscopic images of the extruded as well as the HPT-deformed Mg-alloy after 48 h of in-vitro corrosion. Compared to the extruded Mg-alloy in as-received condition, the surface is covered with corrosion product, excessively forming in local areas (green) partially with lamellar or filamentous shape (yellow) (compare Ref. [56]). Small corrosion pits (red) homogeneously formed throughout the whole surface during immersion. Compared to the as-received Mg-alloy, the surface of the HPT-deformed Mg-alloy is more densely covered with thick corrosion product after 48 h of immersion. Locally deep trenches and cracks are visible and edges partially completely dissolved, which indicate a more pronounced and widespread corrosion damage.

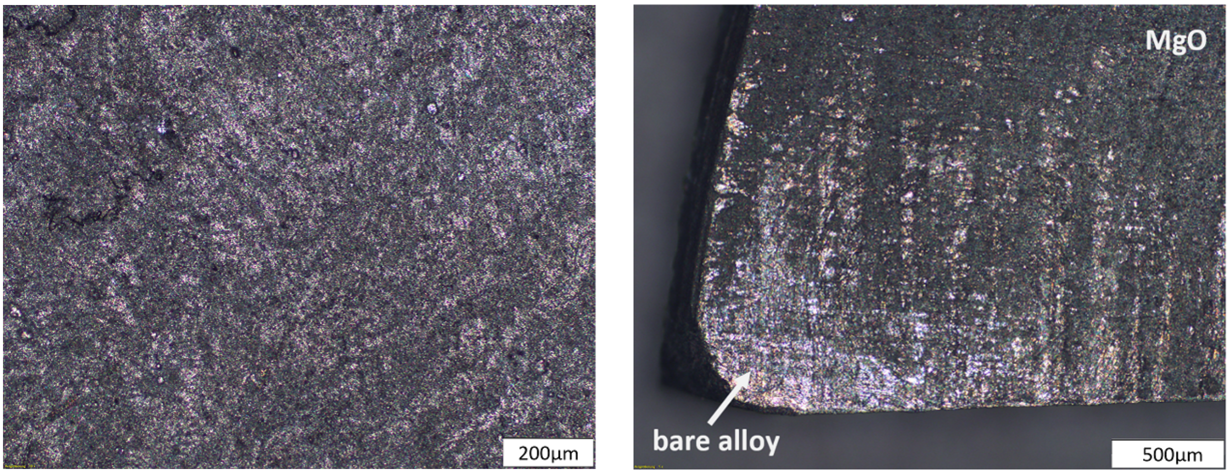

Figure 33: Optical microscopic image of the surface condition for the extruded Mg-alloy in the as-received state.

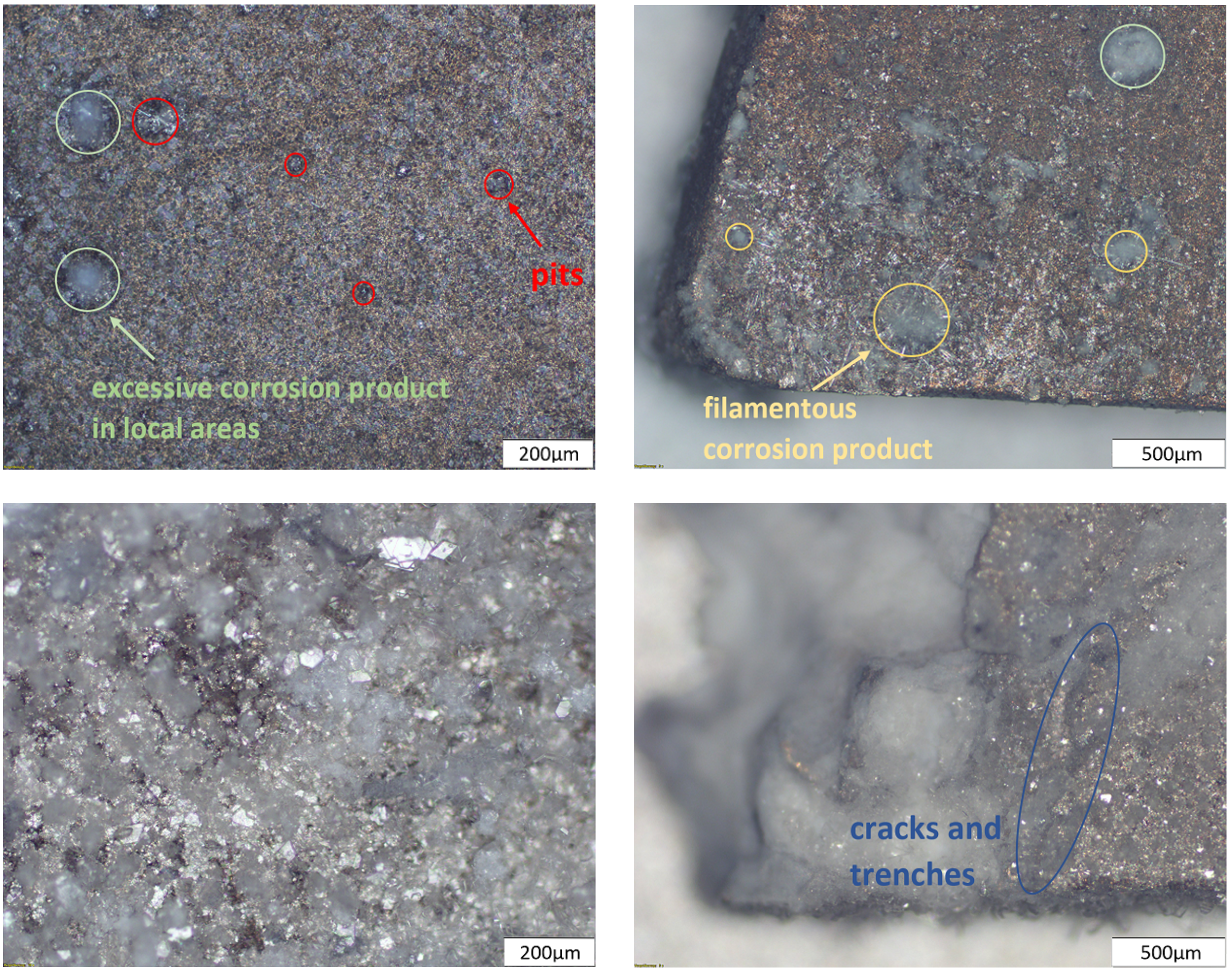

Figure 34: Optical microscopic image of the surface condition for the extruded (top) and HPT-deformed (bottom) Mg-alloy after 48 h of in-vitro corrosion in SBF.

4.3 EIS on as-received Mg-alloy

Nyquist plots and Bode phase plots measured on the as-received Mg-alloy are shown in Fig. 35 and Fig. 37. The associated OCP, determined before initiating each respective measurement after given corrosion time, is shown in Fig. 36.

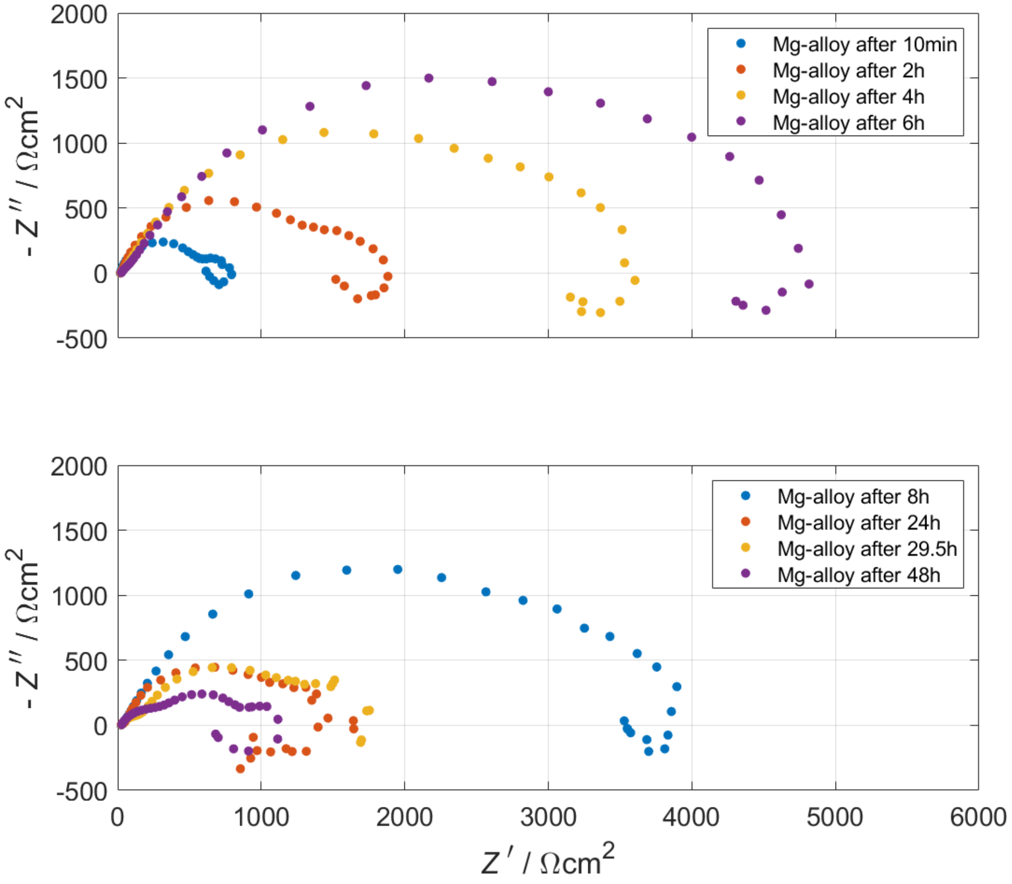

Figure 35: Nyquist plot of as-received Mg-alloy after in-vitro corrosion by immersion in SBF for different times.

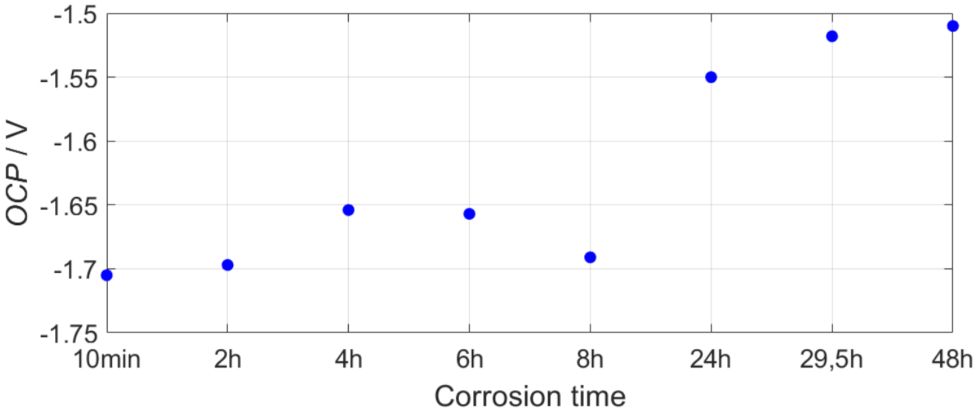

Figure 36: Open circuit potential (OCP) before measurement initiation of electrochemical impedance spectra of as-received Mg-alloy during in-vitro corrosion by immersion in SBF.

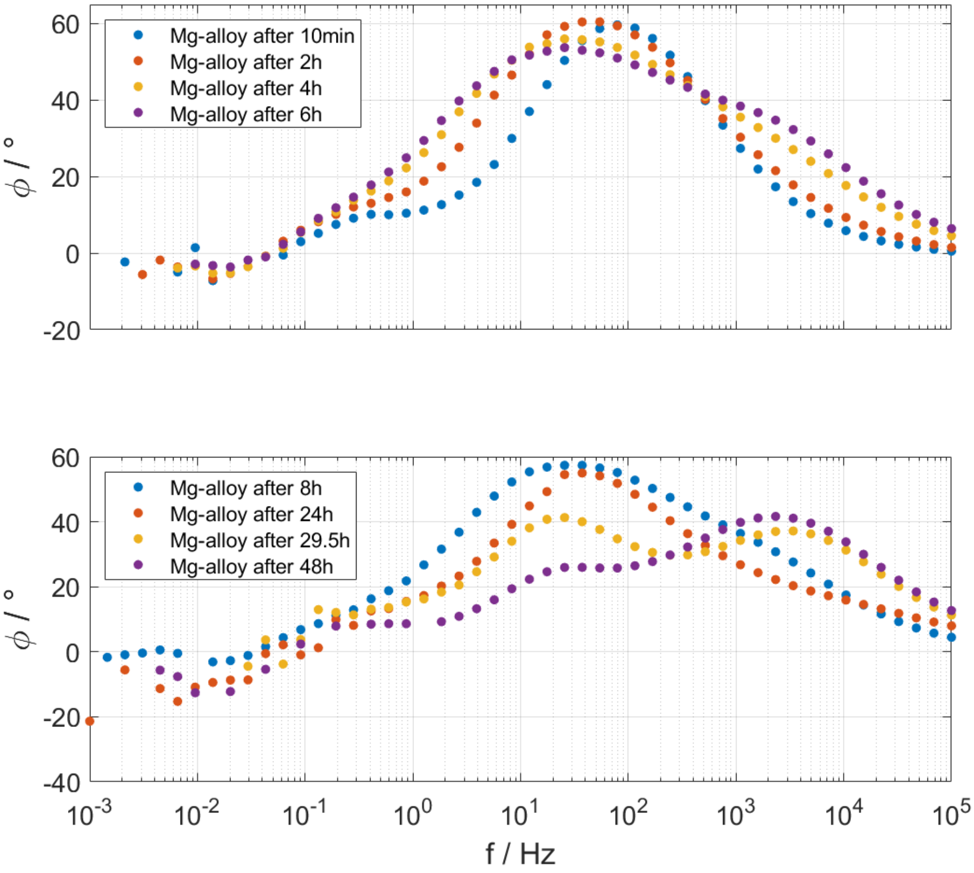

Figure 37: Bode phase of as-received Mg-alloy after in-vitro corrosion by immersion in SBF for different times.

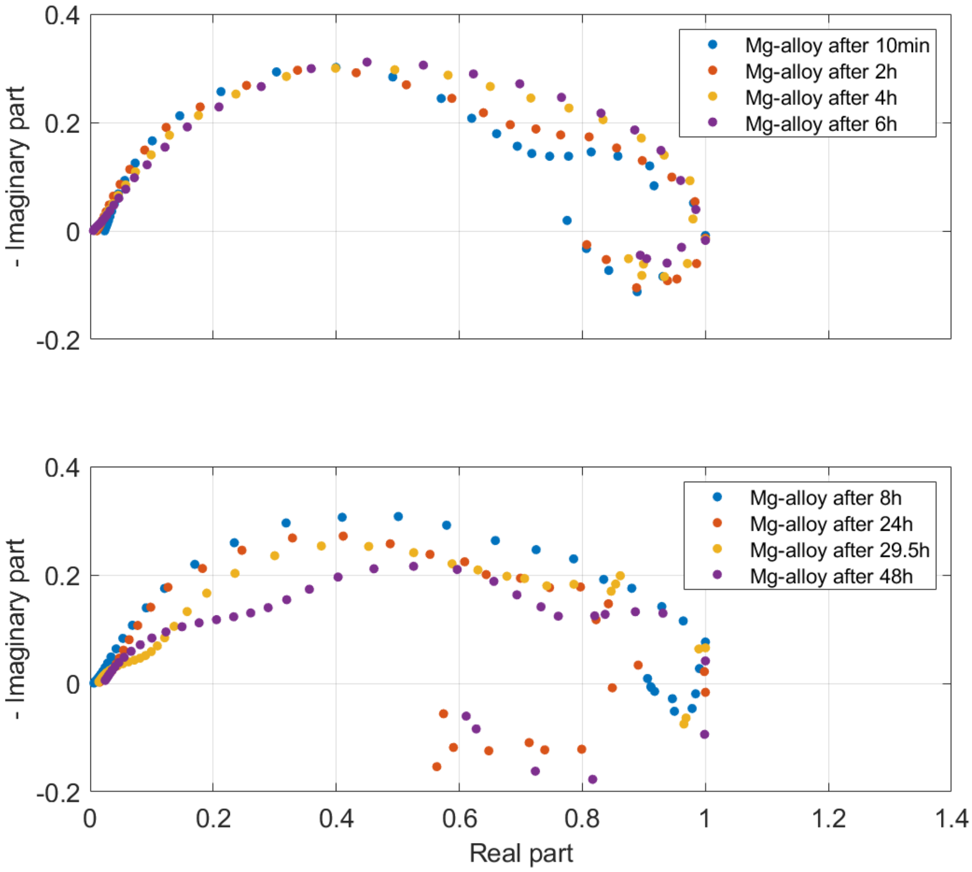

Figure 38: Normalized Nyquist plot of as-received Mg-alloy after in-vitro corrosion by immersion in SBF for different times.

The corrosion potential (OCP) of the immersed sample tends to shift in the anodic direction starting at an open circuit potential of $-1.705\,\mathrm{V/Ag,AgCl}$ after 10 min and reaching $-1.510\,\mathrm{V/Ag,AgCl}$ after 48 h of in-vitro corrosion. Between 4 h and 24 h of immersion, the corrosion potential exhibits a local minimum. Baril et al.[26] argumented, that changes in the corrosion potential are associated with changes in the stability and protectiveness of the corrosion product bilayer. These modifications in the surface bilayer result in a change in pH with increasing immersion time.

The measured EIS spectrum after the initial immersion exhibits the expected two capacitive loops at high and medium frequencies, followed by an inductive loop at low frequencies mainly resulting from the faradaic impedance Z_F.[25] The charge transfer loop at high frequencies is more pronounced than the finite-length diffusional loop at medium frequencies and the inductive loop at low frequencies. With increasing in-vitro corrosion, the size of the high and medium frequency capacitive loops as well as the low frequency inductive loop increased up to 6 h (see Fig. 35, 6 h). Additionally, the shape of the spectra and the characteristic frequencies changed as illustrated by the normalized Nyquist plot shown in Fig. 38 and the Bode Phase plot shown in Fig. 37. The spectra were normalized by dividing the real and imaginary part of the impedance by the maximum value of the real part of each spectrum. The normalized spectra are often used to compare the contributions and changes of the corrosion mechanisms, and to evaluate dependencies and couplings from the EIS setup.[26] The high frequency charge transfer loop flattens with increasing immersion time and the transition between high and medium frequency capacitive loop tends to merge, indicating a developing corrosion mechanism or change in the surface bilayer microstructure. In the Bode Phase plot, a fourth characteristic frequency arises at very high frequencies, and the characteristic frequency of the charge transfer loop shifts to lower frequencies (see Fig. 37, 6 h). After 8 h and 24 h of immersion, the size of the capacitive loops decreased again, whereas the inductive loop increased significantly after 24 h of in-vitro corrosion (see Fig. 35, 8 h and 24 h). The characteristic frequency at very high frequencies may has vanished up to 24 h of immersion (see Fig. 37, 24 h). After 29.5 h of in-vitro corrosion by immersion, an additional small capacitive loop emerges at very high frequencies, which is associated with the charateristic frequency already arising during the first hours of immersion (see Fig. 35, 29.5 h). Upon 48 h of immersion, the emerged third capacitive loop as well as the low frequency inductive loop increased. Both remaining capacitive loops decreased in size, whereby the high frequency loop further flattened.

The measured EIS spectra were analyzed using the schematic representation of the SBF-MgCaZn alloy interface shown in Fig. 14. Therefore, the equivalent circuit derived in 2.3.1 was applied using small adaptions, as shown in Fig. 39. In order to increase the fit quality obtained by NOVA and considering modifications of the alloy surface during in-vitro corrosion, the double layer capacitor C_{dl} was considered as constant phase element (CPE) $CPE_{C_{dl}}$ in the equivalent circuit EC1 used. The consistency and stability of the measured impedance spectra were checked using the Kramers-Kronig relations tool of *NOVA*, which is based on the description by B.A. Boukamp[57]. It has been shown, that these EIS spectra are consistent with the Kramers-Kronig relations by M.E. Orazem et al.[58]. The residues for the measured EIS spectra are distributed randomly around zero, whereby the errors increased significantly in the low frequency range as the measured impedance dispersed to some extent. This indicates stability problems in the low frequency range due to the increasing measurement time per frequency step and the ongoing degradation by in-vitro corrosion, which may impede uncovering trends of the anodic behaviour[59,60].

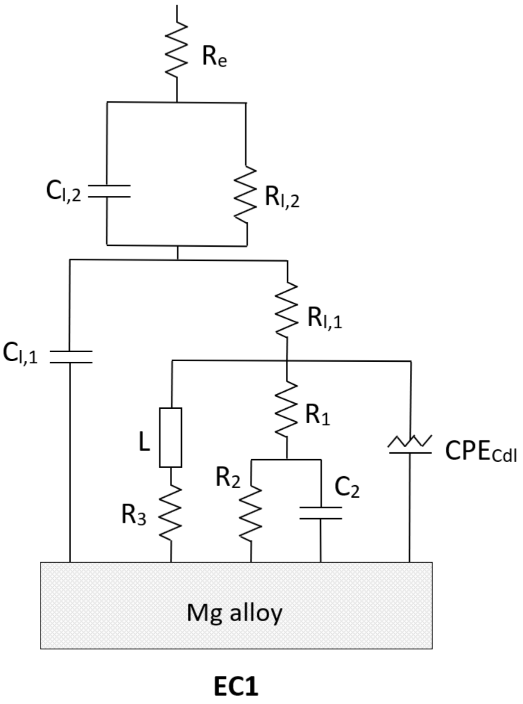

Figure 39: Equivalent circuit EC1 used to fit and simulate measured EIS spectra of as-received Mg-alloy using *NOVA*.

The measured EIS spectra for the as-received Mg-alloy with the corresponding fit associated with the equivalent circuit EC1 are shown in Fig. 40. The resulting fitted elements as well as the fit quality χ^2 obtained with *NOVA* are listed in Tab. 13.

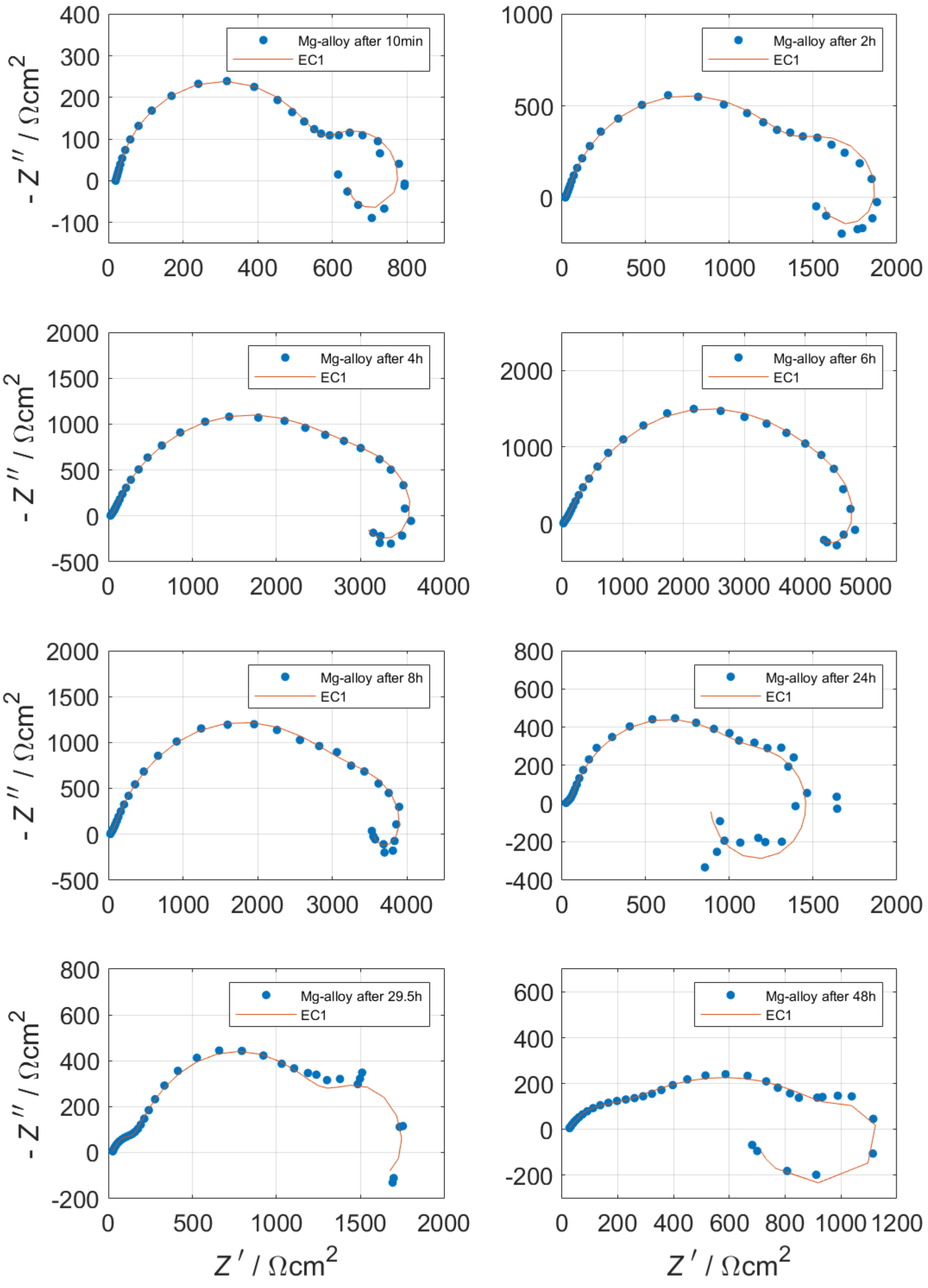

Figure 40: Electrochemical impedance spectra of as-received Mg-alloy after in-vitro corrosion by immersion in SBF for different times. The spectra were fitted with the elements obtained from the equivalent circuit EC1.

Table 13: Fitted elements of the equivalent circuit EC1 (see Fig. 39) for as-received Mg-alloy during in-vitro corrosion by immersion in SBF with a fit quality of χ^2 obtained by *NOVA*.

CT	R_e [Ωcm^2]	$C_{l,2}$ [μF/cm^2]	$R_{l,2}$ [Ωcm^2]	$R_{l,1}$ [Ωcm^2]	$C_{l,1}$ [μF/cm^2]	R_1 [Ωcm^2]
10 min	18,7	19,9	0,9	22,8	10,4	552
2 h	20,6	6,2	2,8	33,5	6,4	1424
4 h	24,0	1,8	6,7	52,7	2,5	3212
6 h	25,8	1,3	8,8	74,6	1,7	4703
8 h	24,2	2,0	6,8	60,8	2,7	3448
24 h	24,2	0,8	9,5	36,8	3,0	1132
29.5 h	24,8	0,7	18,2	118,6	1,2	1236
48 h	27,2	0,6	19,7	163,7	0,9	802

	L [Hcm^2]	$Y_{C_{dl}}$ [μS/cm^2]	$n_{C_{dl}}$	C_2 [mF/cm^2]	R_2 [Ωcm^2]	R_3 [Ωcm^2]	χ^2
10 min	266982	31,8	0,81	2,8	203	2877	0.0292
2 h	73114	40,3	0,78	1,9	476	7123	0.0259
4 h	121699	43,5	0,73	1,5	533	14198	0.0089
6 h	142925	43,5	0.70	3,1	415	19859	0.0088
8 h	172171	37,1	0.75	1,7	618	23915	0.0107
24 h	38679	49,4	0.81	1,0	283	1986	0.2022
29.5 h	41981	23.3	0.76	1,9	467	6651	0.0592
48 h	12736	91,4	0,61	5,4	212	943	0.0439

The used equivalent circuit considers the anodic processes at mainly film-free surface region and the cathodic processes at film-free and corrosion product coated regions as illustrated in Fig. 41. Following the analysis of Liu et al.[27], the development of the anodic and cathodic corrosion behaviour can be estimated using the zero-frequency impedances R_A and R_C, respectively, as

$$R_A = R_{l,2} + R_{l,1} + R_3 \tag{71}$$

and

$$R_C = R_{l,2} + R_{l,1} + R_1 + R_2 \ . \tag{72}$$

Here, both R_C as well as R_A consider the corrosion product bilayer, since both corrosion processes may be interfered by a more or less permeable surface layer on the alloy surface.

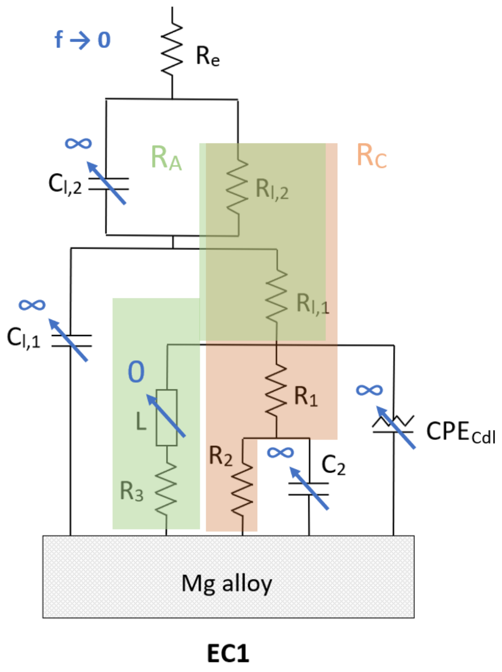

Figure 41: Impedances R_A and R_C estimated using equivalent circuit EC1 for the limit $f \rightarrow 0$.

The overall corrosion behaviour of the as-received Mg-alloy at the corrosion potential (OCP) can be estimated using the zero-frequency impedance R_{ZF}, including elements associated with both anodic (R_A) and cathodic (R_C) corrosion behaviour of the equivalent circuit (see Fig. 41) as

$$R_{ZF} = R_{l,2} + R_{l,1} + \frac{(R_1 + R_2)R_3}{(R_1 + R_2) + R_3} \, . \tag{73}$$

The resulting development of R_A, R_C and R_{ZF} during in-vitro corrosion as well as the ratio of cathodic to anodic zero-frequency impedance R_C/R_A are shown in Fig. 42. The R_C/R_A ratio should give insight in the dominant limiting factors of the corrosion resistance evolving with immersion time.[27]

With increasing immersion time, both R_A and R_C increase significantly with an approximately linear slope. After 8 h of in-vitro corrosion, R_C tends to decrease again and reaches a relatively steady value after 24 h up to 48 h of immersion, whereby R_A increases up to 8 h of immersion and decreases again after 24 h.

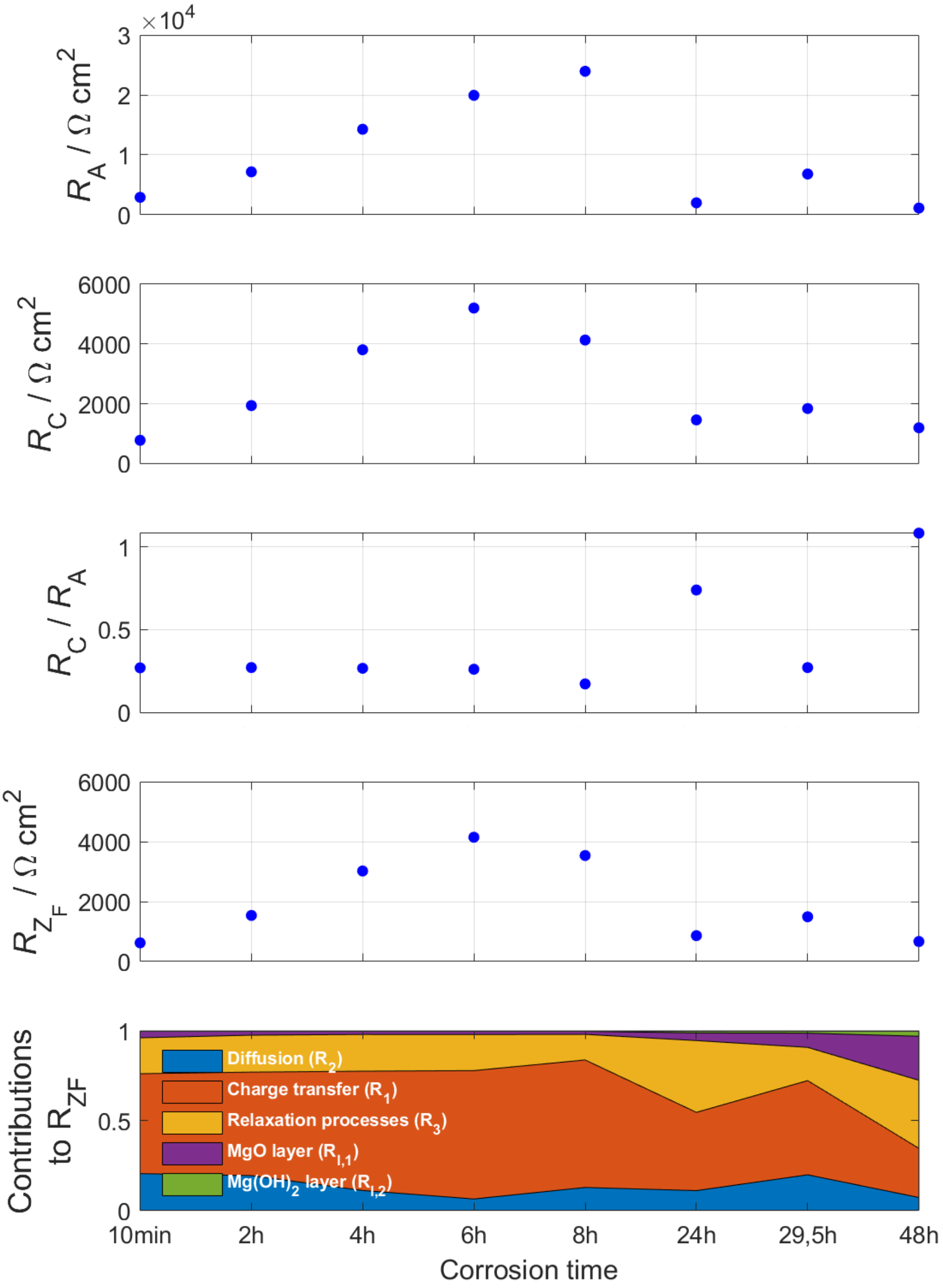

Figure 42: R_C, R_A, R_C/R_A and R_{ZF} of Mg-alloy upon in-vitro corrosion at given time. The resistances were determined according to EC1 in Fig. 39 and eq. (71), (72), and (73). The bottom figure illustrates the contributions from the anodic as well as cathodic corrosion resistance to R_{ZF}.

The R_C/R_A ratio remains approximately constant with a decreasing tendency up to 8 h of in-vitro corrosion. The corrosion rate of the as-received Mg-alloy is limited by a preexisting oxide layer and by a subsequently growing protective corrosion product bilayer on its surface. After 24 h, the R_C/R_A ratio increases due to the rapid change in R_A. The corrosion rate is determined by both anodic and cathodic reaction rates, since R_A and R_C tend to be comparable, whereby a distinct trend for longer immersion times is not visible.

As shown in the bottom part of Fig. 42, the overall zero-frequency corrosion resistance R_{ZF} at OCP is predominantly determined by R_C, especially by the charge transfer resistance R_1 and the resistance R_2 associated with the finite-length diffusion of Mg^{2+} through the porous $\mathrm{Mg(OH)_2}$ surface layer. The contribution associated with the corrosion product bilayer $R_{l,1}$ and $R_{l,2}$ increases with increasing immersion time as well as the resistance contribution associated with the adsorbed intermediate R_3. The inductivity L increases after 2 h up to 8 h of immersion and decreases again for in-vitro corrosion.

Additionally, from the constant phase element ($CPE_{C_{dl}}$) obtained from the fitted EIS spectra, the double layer capacity C_{dl} can be estimated using a modified Brug´s equation for an irreversible uniform charge transfer at a microscopically heterogeneous surface[61,62] as

$$C_{dl} = \left[Y_{C_{dl}} \left(\frac{1}{R_{l,1} + R_{l,2}} + \frac{1}{R_1 + R_2} \right)^{(n_{C_{dl}}-1)} \right]^{\frac{1}{n_{C_{dl}}}} . \tag{74}$$

The overall corrosion product bilayer capacity C_l consisting of an outer, porous $\mathrm{Mg(OH)_2}$ layer and an inner, more dense MgO layer can be approximated (using the bilayer simplification desribed in Sec. 2.3.1) by

$$C_l = \frac{1}{\frac{1}{C_{l,1}} + \frac{1}{C_{l,2}}} . \tag{75}$$

The resulting double layer capacity C_{dl} as well as the corrosion product layer capacity C_l are shown in Fig. 43. It should be noted, that the used equivalent circuit and, therefore, the equations for estimation of R_A, R_C, R_{ZF}, C_{dl}, and C_l differ from the analysis used by Liu et al.[27].

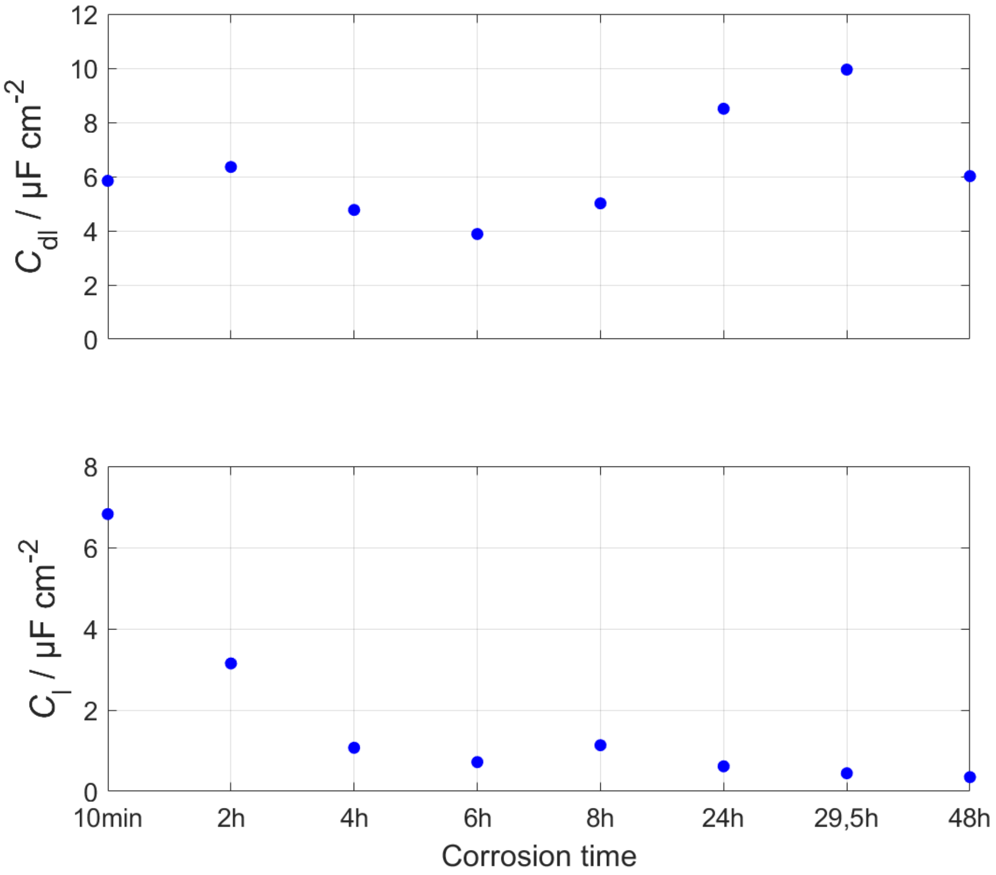

Figure 43: C_{dl} and C_l of as-received Mg-alloy upon in-vitro corrosion by immersion in SBF for given time determined according to eq. (74) and (75), respectively.

The double layer capacity C_{dl} tends to decrease slightly during the first hours of immersion up to 6 h and increasing again for longer immersion times, whereby the overall corrosion product layer capacity C_l was higher than C_{dl} after the initial in-vitro corrosion and decreased rapidly during the first hours of immersion. For longer immersion times, C_l remained approximately constant.

The thickness of the inner, dense MgO surface layer d_{MgO} was estimated using (compare Sec. 2.3.1)

$$d_{MgO} = \frac{\epsilon\epsilon_0 A}{C_{l,1}} x_{PB} \ , \tag{76}$$

with the relative dielectric constant ϵ of MgO ($\epsilon = 10$)[63], the vacuum permittivity ϵ_0, the surface area of the alloy, the surface layer capacity $C_{l,1}$ and the Pilling-Bedworth x_{PB} ratio of MgO ($x_{PB} = 0.8$)[18,64]. Since the actual coverage of the alloy surface is unknown, the Pilling-Bedworth ratio is used to estimate an upper limit for the layer thickness. The actual d_{MgO} is presumably smaller especially for shorter immersion times. The thickness of the outer, porous $Mg(OH)_2$ surface layer $d_{Mg(OH)_2}$ was deduced from (compare Sec. 2.3.1)

$$d_{Mg(OH)_2} = R_{l,2} \kappa A \ , \tag{77}$$

with the film resistance $R_{l,2}$, the coating conductivity κ of the $Mg(OH)_2$ layer and the surface area of the alloy A. The film resistance of the outer layer is used since it influences the impedance for all measured frequencies, and since the growth of the outer surface layer is accompanied by a change in film resistance.[24] The coating conductivity κ was chosen as $\kappa = 2 \cdot 10^{-2}\,\mathrm{S\,m^{-1}}$.[65] The increased surface area during in-vitro corrosion of the outer and inner corrosion product layer as well as the changes in dielectric properties due to changes in film composition were neglected.

With these assumptions, the corrosion product layers were estimated as listed in Tab. 14 and shown in Fig. 44. The initial, inner MgO surface layer is relatively thin with a thickness just below 1 nm, whereas the $Mg(OH)_2$ surface layer is 1.8 µm thick. With increasing immersion time, both corrosion product films increase their thickness with a decline between 6 h and 24 h. The resulting corrosion product layer thicknesses after 48 h of in-vitro corrosion were estimated as 8.2 nm and 39.4 µm for the inner and outer corrosion product layer, respectively.

Table 14: Surface layer thickness of MgO and $Mg(OH)_2$ of the as-received Mg-alloy after in-vitro corrosion for given time determined according to eq. (76) and (77), respectively.

Corrosion time	d_{MgO} [nm]	$d_{Mg(OH)_2}$ [μm]
10 min	0, 7	1, 8
2 h	1, 1	5, 5
4 h	2, 8	13, 4
6 h	4, 3	17, 5
8 h	2, 7	13, 6
24 h	2, 4	19, 1
29.5 h	6, 1	36, 3
48 h	8, 2	39, 4

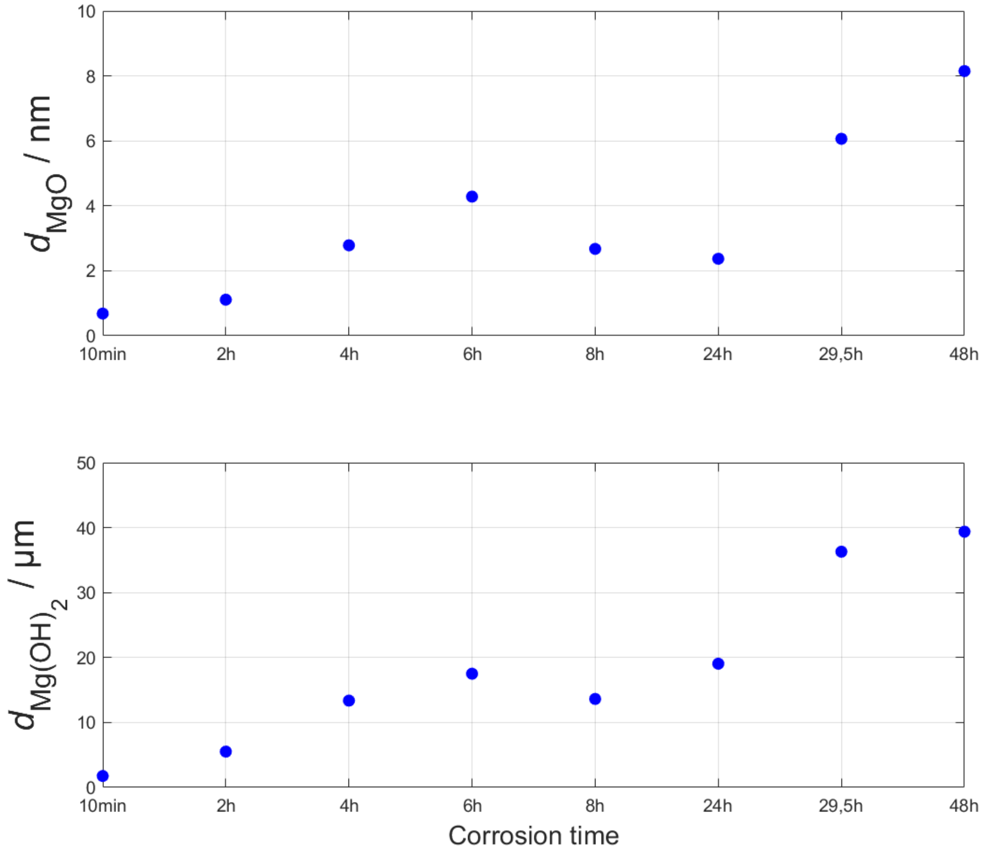

Figure 44: Surface layer thickness of MgO and $Mg(OH)_2$ of as-received Mg-alloy after in-vitro corrosion for given time (see Tab. 14).

4.4 EIS on HPT-deformed Mg-alloy

Nyquist plots and Bode phase plots measured on the HPT-deformed Mg-alloy are shown in Fig. 45 and Fig. 47. The associated OCP, determined before initiating each respective measurement after given corrosion time, is shown in Fig. 46.

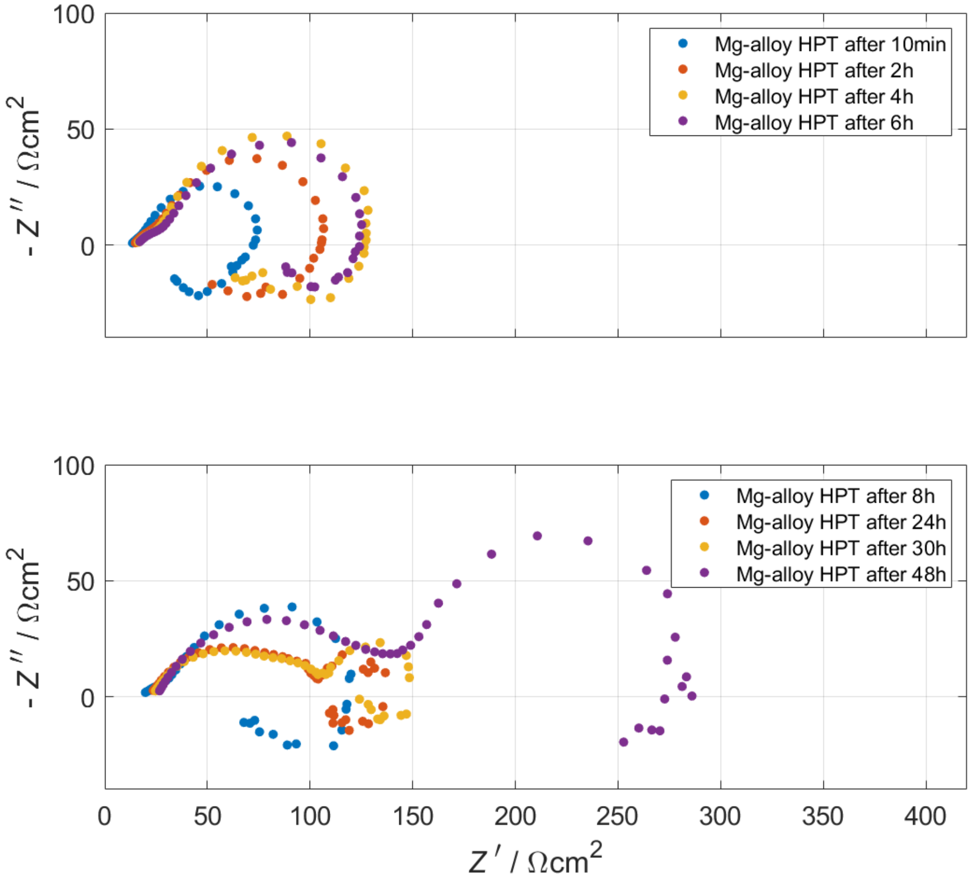

Figure 45: Nyquist plot of HPT-deformed Mg-alloy after in-vitro corrosion by immersion in SBF for different times.

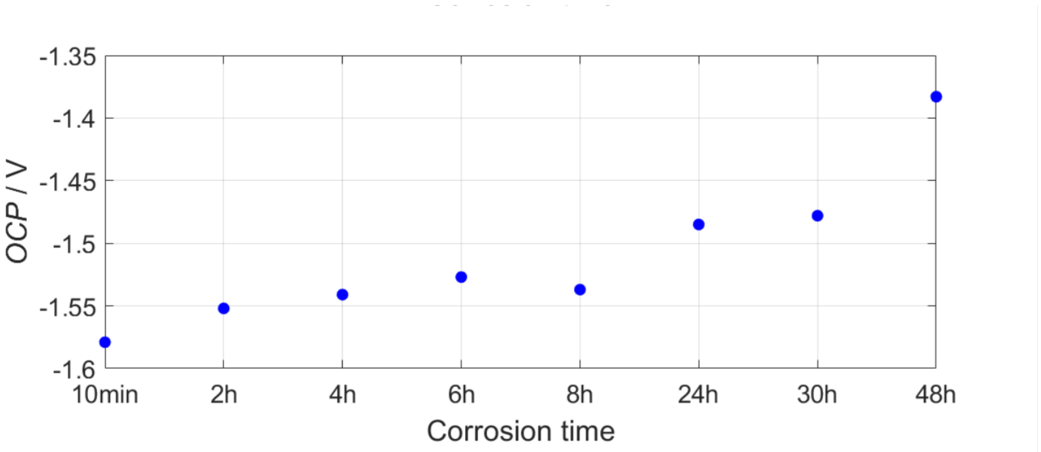

Figure 46: Open circuit potential (OCP) before measurement initiation of electrochemical impedance spectra of HPT-deformed Mg-alloy during in-vitro corrosion by immersion in SBF.

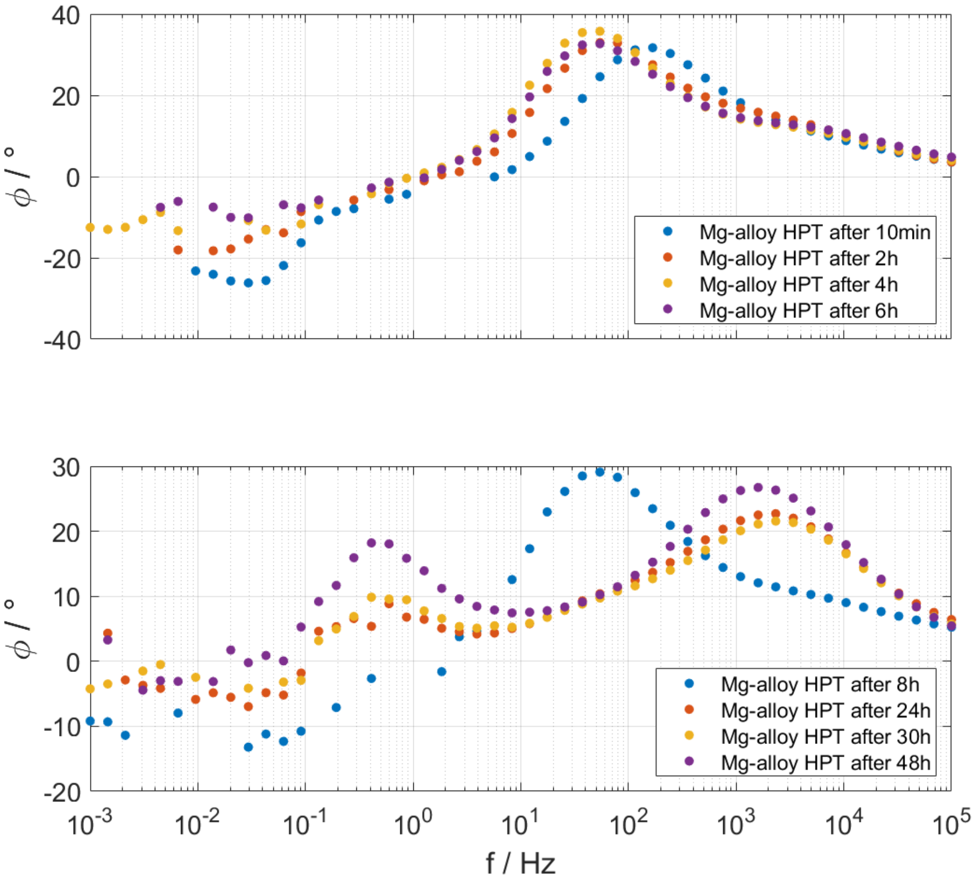

Figure 47: Bode phase of HPT-deformed Mg-alloy after in-vitro corrosion by immersion in SBF for different times.

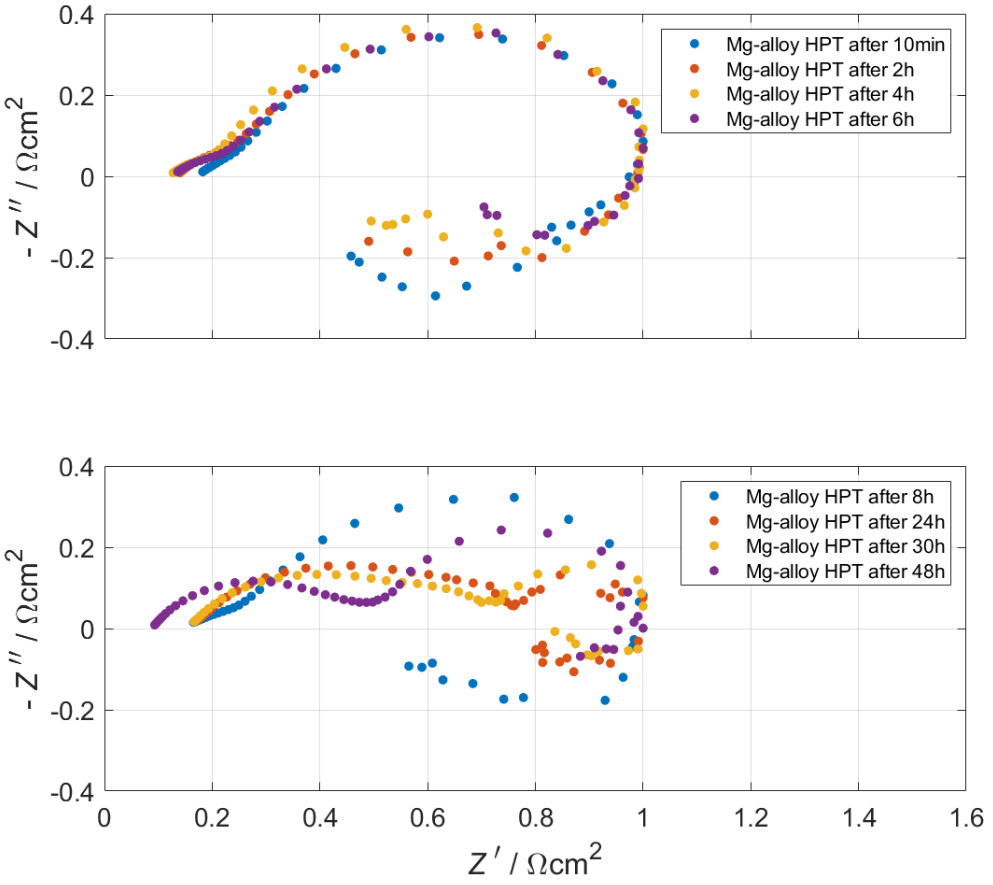

Figure 48: Normalized electrochemical impedance spectra of HPT-deformed Mg-alloy after in-vitro corrosion by immersion in SBF for different times.

The corrosion potential (OCP) of the immersed HPT-deformed Mg-alloy starts at an open circuit potential (OCP) of −1.579 V/Ag,AgCl after 10 min of in-vitro corrosion, which is substantially more positive than for the as received sample (compare Fig. 36 and Fig. 46). With increasing immersion time, the OCP tends to shift gradually in the anodic direction reaching −1.383 V/Ag,AgCl after 48 h of in-vitro corrosion. Compared to the as-received sample, the corrosion potential changes to a smaller extent during the first hours of immersion with the substantial changes occurring for longer immersion times.

The measured EIS spectrum after initial immersion differs fundamentally in terms of form and size from the EIS spectrum obtained for the as-received sample (compare Fig. 35 and Fig. 45, 10 min). The EIS spectrum of the as-received sample exhibits two distinct capacitive loops at medium and high frequencies, as well as an inductive loop at low frequencies. For the HPT-deformed Mg-alloy, the charge transfer loop at high frequencies is barely pronounced and no significant contribution from film effects is visible (see Fig. 45, 10 min). The low frequency inductive loop is comparably larger, but deviates significantly from the ideal semicircle behaviour. This deviation may result from surface inhomogeneities, a high dissolution activity influencing the stability of the measured spectrum, or from coupled reaction sequences.[66]

With increasing in-vitro corrosion the size of the high and medium frequency capacitive loops increase up to 4 h of immersion, whereas the low frequency inductive loop remains approximately constant (see Fig. 45, 4 h). Compared to the as-received sample, the impedance spectra change significantly slower. Other than for the as-received sample (compare Fig. 38), the shape of the normalized spectra for the HPT-deformed Mg-alloy, shown in Fig. 48 mainly changed in the low frequency range decreasing its contribution to the corrosion mechanisms. Small changes are also visible for the high frequency charge transfer loop. In the Bode phase plot shown in Fig. 47, three characteristic frequencies occur clearly visible. After 6 h and 8 h of immersion, respectively, the size of the medium frequency diffusional loop decreased again slightly, whereas the high frequency charge transfer loop as well as the low frequency inductive loop remained approximately constant (see Fig. 45, 6 h and 8 h). The contribution of the low frequency inductive loop to the corrosion mechanisms increased again. After 24 h and 30 h of immersion the charge transfer loop increased significantly in size (see Fig. 45, 24 h and 30 h). The high frequency charge transfer loop is influenced by film effects, since a fourth charateristic frequency emerges at very high frequencies similar to the as-received Mg-alloy. The medium frequency diffusional loop as well as the low frequency inductive loop decreased significantly in size. The flat shape of the high and medium frequency loops indicate high surface inhomogeneities with increasing immersion time. After 48 h of in-vitro corrosion, the influence of film effects further increase, thereby increasing the charge transfer loop. The medium frequency capacitive loop increased significantly in size as well, whereas the low frequency inductive loop is not well pronounced.

The measured EIS spectra were analyzed using the schematic representation of the SBF-MgCaZn alloy interface shown in Fig. 14. For this purpose, the equivalent circuit EC1 used for the HPT-deformed Mg-alloy as well as a slightly adapted equivalent circuit EC2 are shown in Fig. 49. Since the low frequency inductive loop differs from the ideal inductive behaviour, the inductivity L as well as the double layer capacitor C_{dl} were considered as constant phase element (CPE_L) in the equivalent circuit EC2 used. The consistency and stability of the measured impedance spectra were again checked using the Kramers-Kronig relations tool of *NOVA*. The residues for the obtained EIS spectra are distributed randomly around zero, whereby the errors increased significantly in the low frequency range, where the measured impedance dispersed to some extent. Compared to the as-received sample, the residues deviated at higher frequencies, indicating that stability problems set in earlier due to a faster degradation.

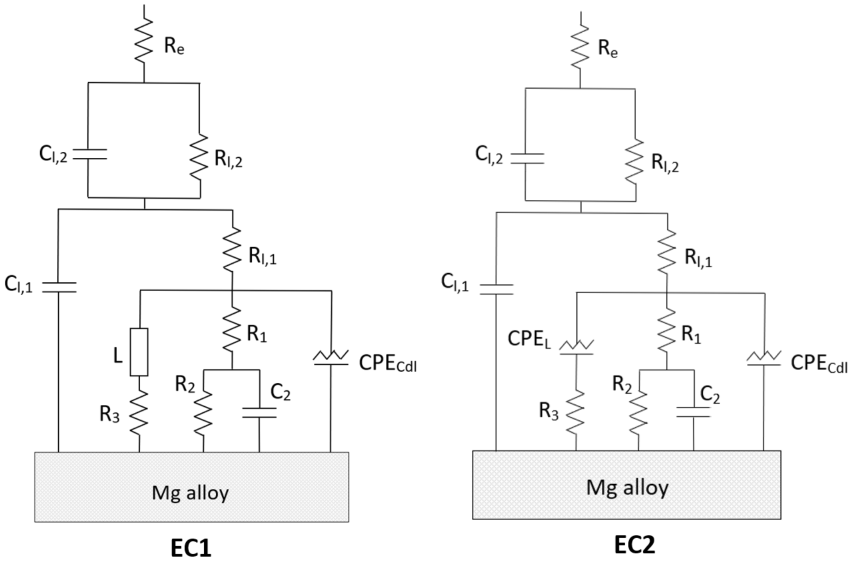

Figure 49: Equivalent circuit EC1 and EC2 used to fit and simulate measured EIS spectra of HPT-deformed Mg-alloy using *NOVA*.

The measured EIS spectra for the HPT-deformed Mg-alloy with the corresponding fit obtained with the equivalent circuit EC1 and EC2 are shown in Fig. 50. The resulting fitted elements as well as the fit quality χ^2 obtained with *NOVA* are listed in Tab. 15 and 16.

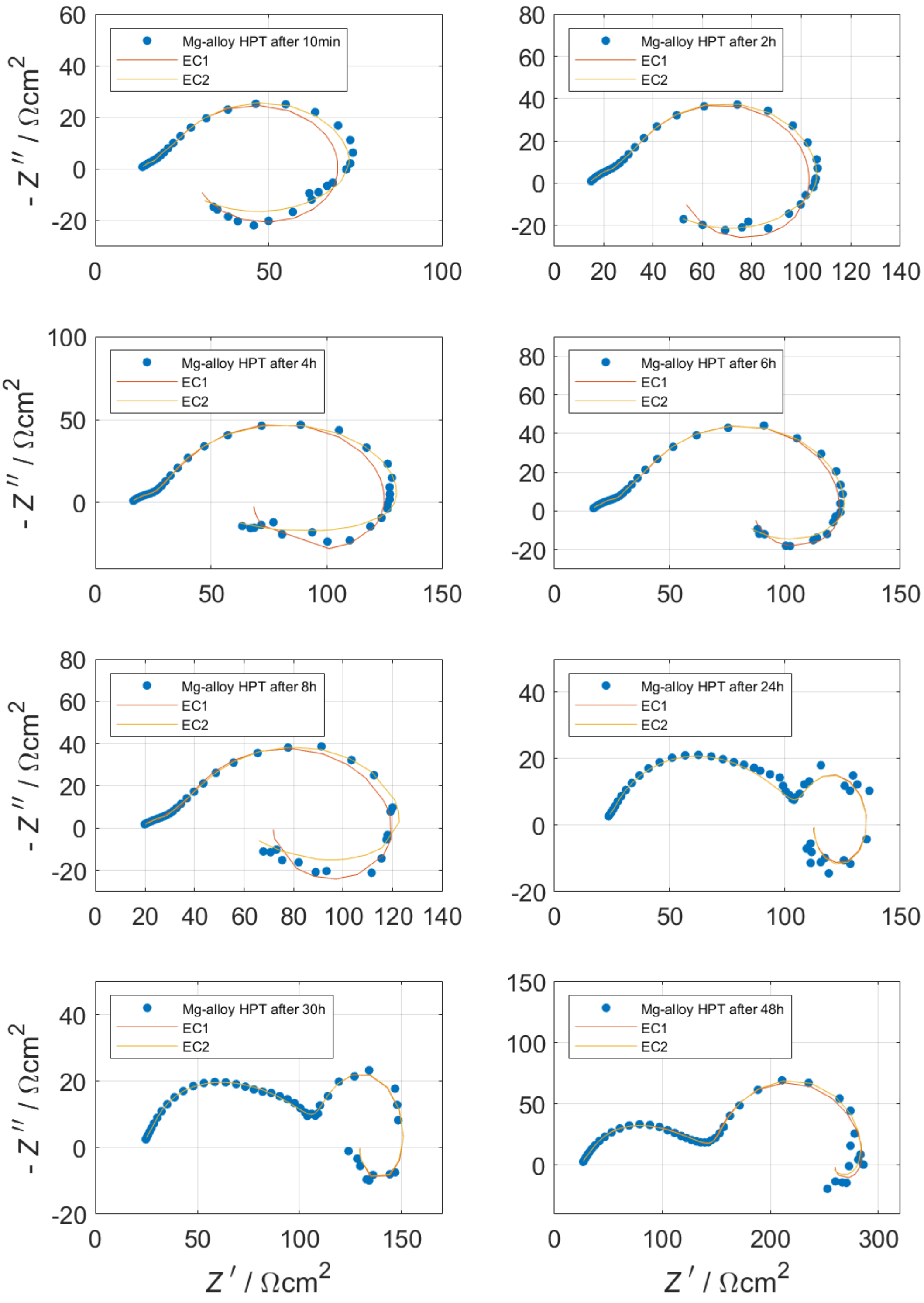

Figure 50: Electrochemical impedance spectra of HPT-deformed Mg-alloy after in-vitro corrosion by immersion in SBF for different times. The spectra were fitted with the elements obtained from the equivalent circuit EC1 and EC2.

Table 15: Fitted elements of the equivalent circuit EC1 (see Fig. 49) for HPT-deformed Mg-alloy during in-vitro corrosion by immersion in SBF with a fit quality of χ^2 obtained by *NOVA*.

CT	R_e [Ωcm^2]	$C_{l,2}$ [μF/cm^2]	$R_{l,2}$ [Ωcm^2]	$R_{l,1}$ [Ωcm^2]	$C_{l,1}$ [μF/cm^2]	R_1 [Ωcm^2]
10 min	13, 0	1, 6	0, 9	5, 2	4, 0	12, 6
2 h	14, 9	3, 3	3, 1	12, 6	9, 3	22, 7
4 h	16, 3	2, 6	3, 8	11, 5	10, 5	30, 0
6 h	16, 9	1, 9	3, 9	11, 6	7, 1	29, 2
8 h	19, 3	12, 6	3, 9	10, 5	6, 1	31, 3
24 h	22, 3	0, 9	2, 6	4, 3	1, 1	81, 5
30 h	24, 0	1, 2	3, 4	15, 3	1, 5	73, 4
48 h	26, 4	1, 5	4, 2	0, 2	1, 3	131, 6

	L [Hcm^2]	$Y_{C_{dl}}$ [μS/cm^2]	$n_{C_{dl}}$	C_2 [μF/cm^2]	R_2 [Ωcm^2]	R_3 [Ωcm^2]	χ^2
10 min	241	6, 8	1, 09	34, 9	38, 0	11, 5	0.1470
2 h	508	16, 0	1, 10	63, 9	49, 8	29, 2	0.0580
4 h	963	19, 4	1, 10	69, 9	63, 1	60, 7	0.1872
6 h	1044	25, 7	1, 04	69, 1	62, 1	134, 5	0.0279
8 h	423	34, 0	0.99	75, 9	53, 9	68, 2	0.1176
24 h	1659	260, 5	0.49	13415, 5	31, 1	321, 6	0.0680
29.5 h	1097	482, 1	0.47	8071, 8	45, 9	323, 0	0,0196
48 h	18197	272, 0	0, 43	2907, 3	135, 9	1647, 7	0.0269

In order to compare the corrosion behaviour of the as-received sample with its HPT-deformed counterpart, the zero-frequency impedances R_A and R_C were estimated using the elements estimated with equivalent circuit EC1. Therefore, Eq. (71) considering the anodic processes at film-free surface regions and (72) considering cathodic processes mainly at corrosion product coated regions were used. The overall corrosion behaviour for the HPT-deformed Mg-alloy was estimated using the zero-frequency impedance R_{ZF}, including elements associated with both anodic and cathodic corrosion behaviour of the equivalent circuit. For this purpose, Eq. (73) was used. The resulting development of R_A, R_C and R_{ZF} during in-vitro corrosion as well as the ratio of cathodic to anodic zero-frequency impedance R_C/R_A are shown in Fig. 51.

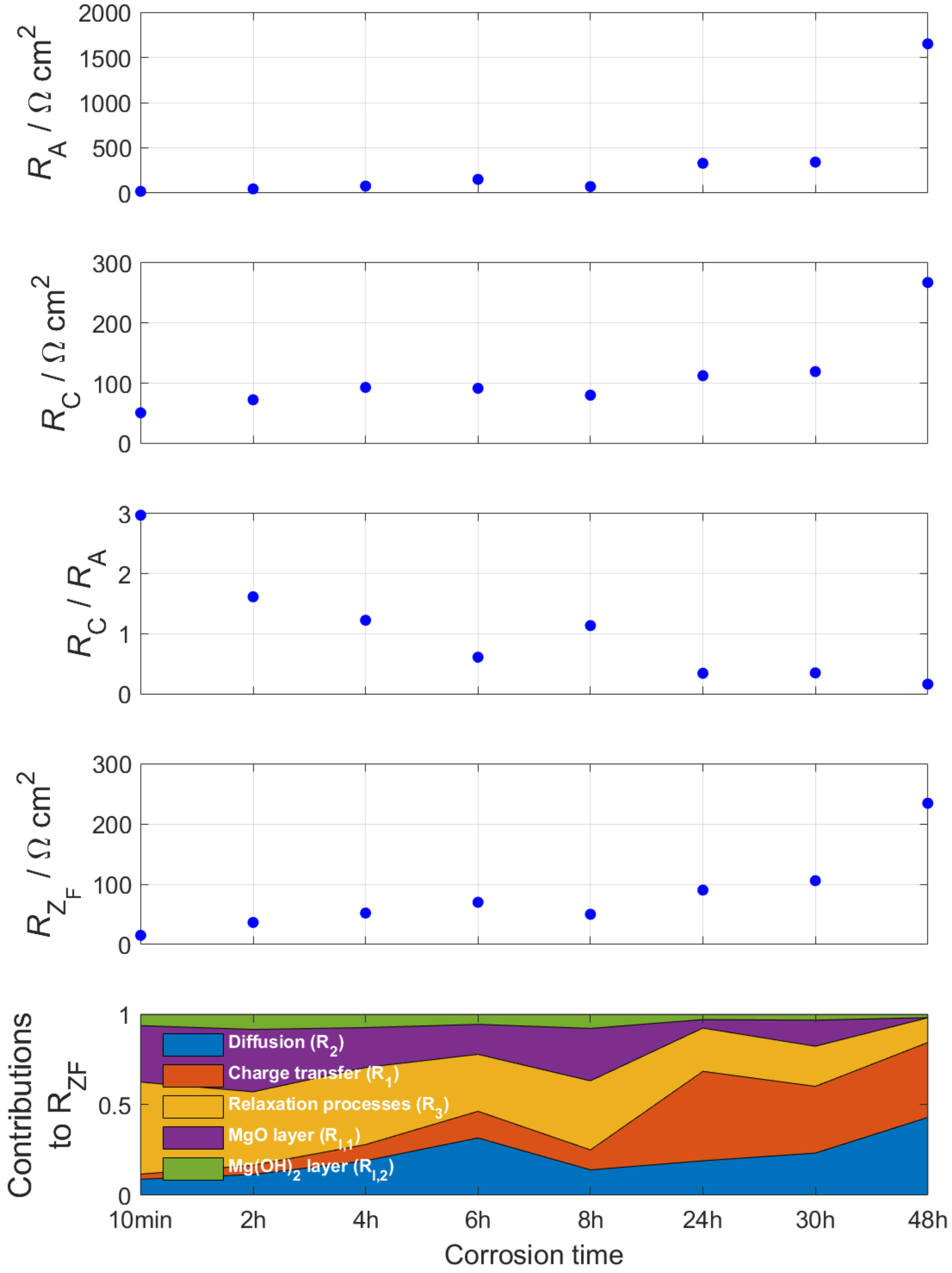

Figure 51: R_C, R_A, R_C/R_A and R_{ZF} of HPT-deformed Mg-alloy upon in-vitro corrosion at given time. The resistances were determined according to EC1 in Fig. 49 and eq. (71), (72), and (73). The bottom figure illustrates the contributions from the anodic as well as cathodic corrosion resistance to R_{ZF}.

Compared to the as-received sample (see Fig. 42), both R_A and R_C increased significantly slower during the in-vitro corrosion. Upon in-vitro corrosion for 24 h up to 48 h, both R_A and R_C increased.

The overall zero-frequency corrosion resistance R_{ZF} at the corrosion potential (OCP) of the HPT-deformed Mg-alloy is influenced to similar parts by both R_A and R_C between 2 h up to 8 h of immersion. The highest contribution stems from the corrosion product bilayer $R_{l,1}$ and $R_{l,2}$ as well as from the resistance associated with the adsorbed intermediates R_3 (see Fig. 51). With increasing immersion time, the contribution arising from the corrosion product bilayer and the adsorbed intermediates decrease, whereas the charge transfer resistance R_1 as well as the diffusional resistance R_2 increase noticeably. Similar to the as-received Mg-alloy, R_{ZF} is determined by R_C in the later stages of in-vitro corrosion.

The R_C/R_A ratio decreases significantly up to 6 h of immersion and remained approximately constant for longer in-vitro corrosion (see Fig. 51). The corrosion rate of the HPT-deformed Mg-alloy is limited by the anodic dissolution rate during the first hours of immersion. For longer immersion times, the limitation is shifted due to the increased protectiveness of the corrosion product surface layer. Compared to the as-received sample, the inductivity L increased progressively with increasing immersion time (see Tab. 15).

From the obtained constant phase element ($CPE_{C_{dl}}$) extracted from the fitted EIS spectra, the double layer capacity C_{dl} can be estimated according to Eq. (74). As can be seen in Tab. 15, $n_{C_{dl}}$ exhibits a value > 1 up to 6 h of immersion, indicating a data overfitting. The used Brug´s equation is solely defined for values of $n_{C_{dl}}$ between zero and unity[62], therefore, no C_{dl} can be estimated.

The results obtained with EC2 do not exhibit such a data overfitting as shown in Tab. 16. The elements fitted with the equivalent circuit show similar trends, whereby the initial in-vitro corrosion significantly differs. These difference may be resulting from the large deviation between the obtained fit with EC1 and the measured spectrum (see Fig. 50, 10 min). The overall corrosion product bilayer capacity C_l consisting of an outer, porous mainly $Mg(OH)_2$ layer and an inner, more dense MgO layer can be estimated using Eq. (75). The resulting double layer capacity C_{dl} as well as the corrosion product layer capacity C_l for both used equivalent circuits EC1 and EC2, respectively, are shown in Fig. 52.

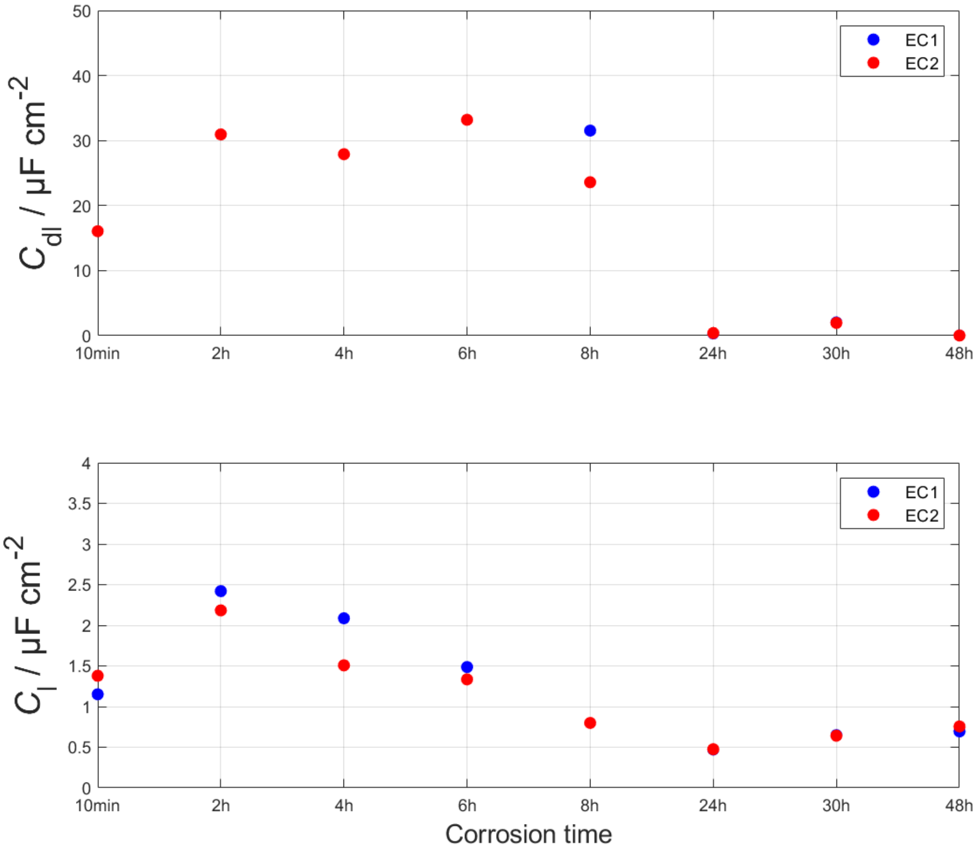

Figure 52: C_{dl} and C_l of HPT-deformed Mg-alloy upon in-vitro corrosion by immersion in SBF for given time determined according to eq. (74) and (75), respectively. C_{dl} obtained by fitting with equivalent circuit EC1 is not defined up to 6 h of immersion since the modified Brug´s equation is valid for $n_{C_{dl}} \in [0,1]$ (compare Tab. 15).

The double layer capacity C_{dl} increased rapidly during the first hours of corrosion up to 2 h and remained approximately constant up to 6 h. The overall corrosion product layer capacity C_l increased after 2 h of immersion and decreases up to 8 h of in-vitro corrosion. The changes in C_l are accompanied by increasing surface film resistances $R_{l,1}$ and $R_{l,2}$. After 24 h up to 48 h of in-vitro corrosion, C_{dl} decreased significantly. C_l further decreased and remained approximately constant with progressing in-vitro corrosion.

Table 16: Fitted elements of the equivalent circuit EC2 (see Fig. 49) for HPT-deformed Mg-alloy during in-vitro corrosion by immersion in SBF with a fit quality of χ^2 obtained by *NOVA*.

CT	R_e [Ωcm^2]	$C_{l,2}$ [μF/cm^2]	$R_{l,2}$ [Ωcm^2]	$R_{l,1}$ [Ωcm^2]	$C_{l,1}$ [μF/cm^2]	R_1 [Ωcm^2]	Y_L [μS/cm^2]
10 min	13,1	2,0	1,0	5,3	4,3	16,6	6,8
2 h	14,8	3,1	2,5	10,9	7,6	27,0	3,3
4 h	16,1	2,1	2,2	8,1	5,3	31,4	3,1
6 h	16,8	1,8	3,3	10,5	5,7	34,1	1,8
8 h	19,0	1,0	3,1	8,1	3,9	44,3	0,5
24 h	22,3	0,8	2,7	5,4	1,1	80,1	0,5
30 h	24,0	1,2	3,3	14,4	1,5	74,8	1,0
48 h	26,5	1,5	5,5	0,2	1,6	137,2	2,9

	n_L	$Y_{C_{dl}}$ [μS/cm^2]	$n_{C_{dl}}$	C_2 [μF/cm^2]	R_2 [Ωcm^2]	R_3 [Ωcm^2]	χ^2
10 min	−0,69	16,5	1,00	32,9	38,1	0,2	0,0684
2 h	−0,67	37,7	0,98	53,4	53,0	6,2	0,0106
4 h	−0,40	104,3	0,84	31,6	86,5	14,8	0,0261
6 h	−0,67	53,1	0,94	56,8	63,6	89,4	0,0151
8 h	−0,49	148,0	0,78	41,5	60,6	33,9	0,0883
24 h	−1,05	262,0	0,49	13340,8	29,8	331,9	0,0678
30 h	−0,96	485,8	0,47	8071,7	47,7	312,0	0,0195
48 h	−0,68	414,8,8	0,38	2884,9	158,0	955,1	0,0244

The thickness of the inner dense MgO surface layer d_{MgO} as well as the thickness of the outer porous Mg(OH)$_2$ surface layer $d_{Mg(OH)_2}$ were again estimated using Eq (76) and (77). With the same assumptions, the corrosion product layers were estimated as listed in Tab. 17 and shown in Fig. 53, using the elements obtained with EC1 and EC2. The resulting initial inner MgO surface layer is again relatively thin with a thickness of 1.8 nm and 1.6 nm for EC1 and EC2, respectively. The outer Mg(OH)$_2$ surface layer is 1.9 µm and 2.0 µm thick. With increasing immersion time, the MgO surface layer remained approximately constant up to 8 h for both equivalent circuits.

The thickness of the outer Mg(OH)$_2$ surface layer increased, whereby the growth was slower for EC2 and seems to level off at a lower thickness up to 30 h of in-vitro corrosion. After 24 h of immersion, the MgO surface layer increased and resulted in a thickness of 6.6 nm and 6.4 nm for EC1 and EC2, respectively. The outer Mg(OH)$_2$ surface layer increased up to 8.5 µm and 10.9 µm after 48 h of immersion. The increased fit quality obtained by using EC2 has little influence on the thickness of the inner dense MgO surface layer d_{MgO} as well as the developing outer Mg(OH)$_2$ surface layer $d_{Mg(OH)_2}$.

Table 17: Surface layer thickness of MgO and Mg(OH)$_2$ of the HPT-deformed Mg-alloy after in-vitro corrosion for given time determined with EC1 and EC2 according to eq. (76) and (77), respectively.

	EC1		EC2	
Corrosion time	d_{MgO} [nm]	$d_{Mg(OH)_2}$ [μm]	d_{MgO} [nm]	$d_{Mg(OH)_2}$ [μm]
10 min	1,8	1,9	1,6	2,0
2 h	0,8	6,1	0,9	5,0
4 h	0,7	7,6	1,8	1,9
6 h	1,0	7,8	1,3	6,6
8 h	1,2	7,8	1,8	6,1
24 h	6,6	5,2	6,4	5,3
29.5 h	4,7	6,8	4,8	6,6
48 h	5,5	8,5	4,6	10,9

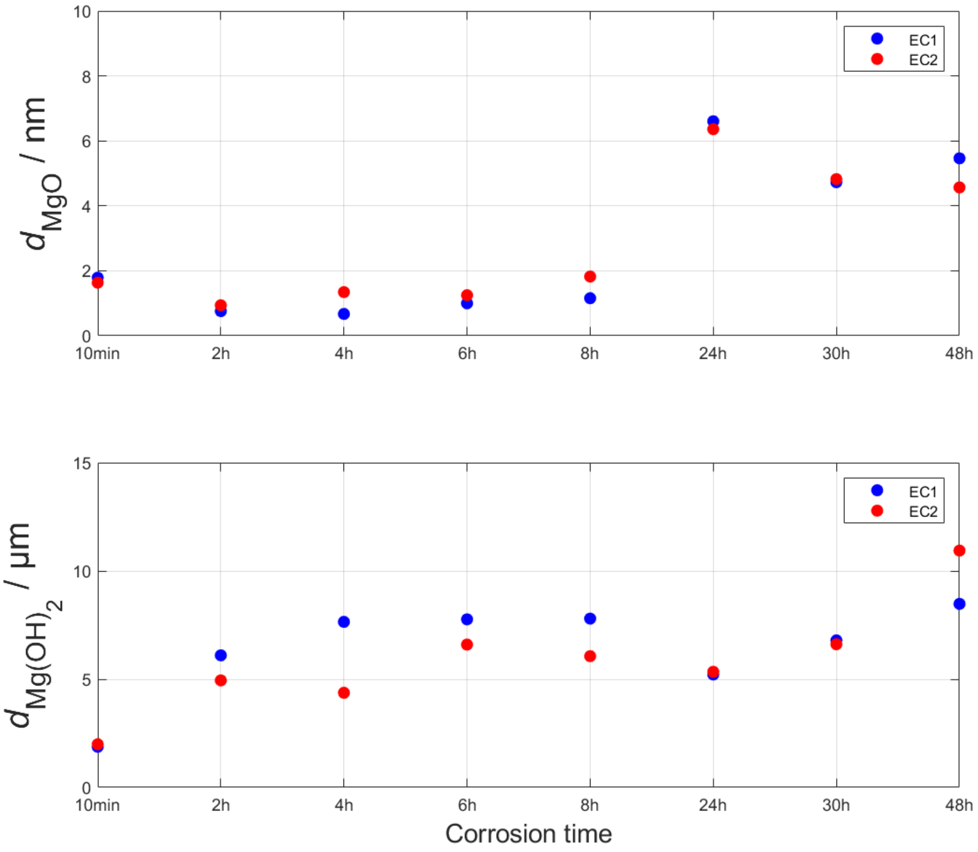

Figure 53: Surface layer thickness of MgO and $Mg(OH)_2$ of HPT-deformed Mg-alloy after in-vitro corrosion for given time (see Tab. 17).

5 Discussion

In the following chapter, the results obtained in Sect. 4 are further interpreted and the underlying significant differences in corrosion performance due to severe plastic deformation are discussed. Therefore, an attempt was made to combine the development of the structural defects obtained by the component analysis of the PALS spectra with the predominant surface reactions progressing with immersion time in SBF obtained by the EIS spectra in order to propose distinct corrosion models for the as-received and the HPT-deformed Mg-alloy.

5.1 Development of structural defects

5.1.1 Initial states

The as-received Mg-alloy exhibits a fine-grained structure with an average grain size of approximately 2 - 3 µm and occasionally with larger grains of 5 µm size. Additionally, the as-received sample exhibited small finely distributed cathodic Mg_2Ca particles as only intermetallic precipitate determined in SEM and EDX measurements by Brunner et al.[67] and consistent with Johnston et al.[68] and Holweg et al.[2]. These second-phase particles exhibit a small fraction of Zn[2,67] and are less noble than the Mg matrix and, therefore, dissolve preferentially increasing the corrosion rate.[68,69]

Additionally, according to Nie et al.[70], the difference in lattice parameter of the Mg_2Ca particles compared to the Mg matrix results in a lattice misfit on the habit plane of 12.1 %. Thereby, when the intermetallic particles reach a critical size ($\approx 1.7\,\mathrm{nm}$) it is expected, that open-volume defects accumulate at the precipitate-matrix interface. The Mg_2Ca particles themselves do not act as attractive sites or traps for positrons, whereas the adjoining misfit open-volume defects can noticeably influence the positron lifetime.[71]

For the **as-received Mg-alloy** a mean positron lifetime $\tau_{mean} = (231.8 \pm 0.3)\,\mathrm{ps}$ was measured (see Tab. 5). The two-component analysis resulted in $\tau_1 = (200 \pm 22)\,\mathrm{ps}$ with $I_1 = (41.1 \pm 35.8)\,\%$ and $\tau_2 = (254 \pm 17)\,\mathrm{ps}$ with $I_2 = (58.9 \pm 35.8)\,\%$. The measured τ_{mean} is close to the bulk positron lifetime of pure magnesium, indicated in Tab. 1, and found in Mg-1 wt%Ca alloys with $(225 \pm 2)\,\mathrm{ps}$ before heat treatment (i.e. before precipitation formation)[71]. For a similar MgCaZn alloy (ZX10) with a higher Zn content used by Cihova et al.[14], the size of the Mg_2Ca precipitates was determined as (80 ± 35) nm with an average spacing of 1250 nm and a volume fraction of $1.1 \cdot 10^{-3}$ for presumed spherically shaped precipitates.

When assuming that the volume fraction of the second phase Mg_2Ca particles is very low, so that the fraction of positrons annihilating in the precipitates is negligible, the annihilation at the precipitate/matrix interface can be estimated using the diffusion-reaction model for small spherical extended defects in precipitate-matrix composites proposed recently by our group[72]. Similar to the general case of trapping at voids exclusively (Eq. 30 and 31 in Ref.[72]), trapping due to diffusion from the matrix is considered. The model predicts a mean positron lifetime of $\tau_m = 225.2$ ps with a trapping intensity of $I_t = 4.0$ % using the parameters $\tau_f = 225$ ps, $\tau_t = 254$ ps, $D = 0.5 \cdot 10^{-4}$, $\alpha = 3 \cdot 10^3\,\mathrm{m\,s^{-1}}$, $R = 610$ nm and $r_0 = 40$ nm. Another positron trapping model proposed by Oberdorfer and Würschum[73] regards point defects and grain boundaries in polycrystalline materials, with which the positron trapping in grain boundaries of the as-received Mg-alloy can be estimated. For the limiting case of negligible trapping inside grains (Eq. 30 and 31 in Ref.[73]), a mean positron lifetime $\tau_m = 232.2$ ps with a trapping intensity $I_t = 62.6$ % and $\tau_m = 230.0$ ps with a trapping intensity $I_b = 47.7$ % were determined for grain sizes of 2 µm and 3 µm, respectively, using the parameters $\tau_f = 225$ ps, $\tau_t = 254$ ps, $D = 0.5 \cdot 10^{-4}$, $\alpha = 3 \cdot 10^3\,\mathrm{m\,s^{-1}}$, $r = 1000$ nm and 1500 nm. When comparing τ_m and I_t for the two different models it can be concluded, that trapping in the Mg_2Ca precipitates and in misfit defects at the interface is indeed not the dominant effect, but rather the positron trapping at grain boundaries. The calculated values for τ_m and I_t deduced from the grain boundary trapping model are in good agreement with the measured mean positron lifetime $\tau_{mean} = (231.8 \pm 0.3)$ ps and the associated intensity $I_2 = (58.9 \pm 35.8)$ % (see Tab. 5). This means, that the model with exclusive trapping at grain boundaries well fits, although some defects are present inside the grains.

After severe plastic deformation of the as-received Mg-alloy, a significant grain refinement with the typical elongated grains of 3 × 1 µm along with an increased number density of grain boundaries occurs.[67] For the **HPT-deformed Mg-alloy** a mean positron lifetime $\tau_{mean} = (241.4 \pm 0.3)$ ps was measured (see Tab. 9). This suggests saturation trapping and annihilation in dislocations, in the deformation-induced misfit defects at grain boundaries, and in the matrix-precipitate interfaces as found in ultra-fine grained Mg-4Y-3RE alloy with

$\approx$ 240 ps[74]. These open-volume defects can not be distinguished since their associated positron lifetimes are similar.

5.1.2 Progressing self-corrosion in SBF

The self-corrosion of ultra-high purity magnesium in simulated body fluid is expected to take place in two distinct stages as found by Lee et al.[22] for pure Mg immersed in Hank's solution. The initial first stage of corrosion is characterized by a uniform, homogeneous formation of solid corrosion products along with a slow hydrogen formation. The formed corrosion products mainly consist of $Mg(OH)_2$ and hydroxyapatite ($Ca_{10}(PO_4)_6(OH)_2$, HA). Impurities such as Fe precipitates lead to localized corrosion, whereby these sites are subsequently passivated by porous HA. In the second stage of corrosion, the corrosion rate rapidly increases due to preferred crystallographic pitting (PCP) along pits and cracks, which are formed during localized corrosion. As the pits propagated during the transition to the second stage, chloride ions diffuse into the pits resulting in the formation of HCl environment and thereby intensively accelerating the corrosion along preferential crystallographic planes.[22,75] For pure Mg with a $\frac{Fe}{Mn}$ ratio of 0.933, the transition from a homogeneous corrosion to an increased formation of pits takes place after $\approx$ 20 h of immersion, whereby the rapid onset of the corrosion rate occurs between 40 and 50 h.[22]

The second phase particles of the as-received Mg-alloy are mainly located discontinuously along grain boundaries, whereas partially small particles can be found inside grains of the alloy matrix.[2,67,76,77] Since the intermetallic particles exhibit a lower corrosion potential, corrosion propagates especially along these precipitates at the grain boundaries. This propagating corrosion at susceptible regions near the second phase particles will result in formation of localized pits. The HPT-treatment of the as-received Mg-alloy results in a more homogeneous and finely dispersed distribution of the Mg_2Ca particles throughout the alloy matrix after deformation.[76,77]

Severe plastic deformation also highly influences the properties of the corrosion product film formed during corrosion. The corrosion product bilayer mainly consists of a thin inner MgO layer and an outer nanoporous filamentous $Mg(OH)_2$ layer as investigated by Unocic et al.[78] and Brady et al.[56]. The pores in the outer layer exhibit a size of approximately 20 - 40 nm. Additionally, $MgCO_3$[56] and HA[22] is probably incorporated into the surface film. The inner layer is more densely packed and adheres very well to the Mg surface compared to the outer layer, which is more loose. With progressing corrosion, the formed corrosion product layer increasingly forms cracks in the inner MgO layer. The HPT-deformation strongly influences the microstructure and stability of the MgO layer. Additionally, the corrosion mainly progresses along structural defects, which are to a high extent introduced by the severe plastic deformation. Even though the HPT-deformed Mg-alloy probably exhibits a better defined oxide layer, the corrosion product film may be increasingly impermeable and less stable in chloride containing solutions.[79]

0 s - 12 s For the initial state of the **as-received Mg-alloy** as well as after 12 s of immersion, the mean positron lifetime τ_{mean} remained approximately constant (see Tab. 5), indicating that the surface is hardly influenced by the slow anodic dissolution. An initially present oxide surface layer probably transforms during the initial corrosion.

For the **HPT-deformed Mg-alloy** the initial state as well as after 12 s of immersion a single positron lifetime component (see Tab. 9) was measured. It is therefore expected, that saturation annihilation dominates the mean positron lifetime τ_{mean} and the influence of initial corrosion of 12 s is negligible. Compared to the as-received Mg-alloy, the mean positron lifetime τ_{mean} of the as-received condition and after the initial corrosion is noticeably higher due to the introduction of a high density of structural defects during the sever plastic deformation.

60 s - 2 h After 60 s of immersion, the mean positron lifetime τ_{mean} of the **as-received Mg-alloy** still remained approximately constant (see Tab. 5), indicating that the in-vitro corrosion did not introduce noticeably open-volume defects influencing the mean positron lifetime. It is expected, that at this stage corrosion products begin to form on the alloy surface and second phase particles start to dissolve. After 5 min up to 2 h of immersion, an increase of τ_{mean} is measured, mainly caused by the progressively increasing defect positron lifetime τ_2. The first positron lifetime τ_1 remained approximately constant after 5 min throughout the whole in-vitro corrosion within the error margin. τ_1 for $t \geq 5$ min may be considered as slightly reduced mean positron lifetime of the initial state, where the (strongly reduced) τ_1 and τ_2, measured for shorter immersion times, can not be distinguished further by the fitting program due to their small difference in positron lifetime. Thus, it is expected that a possible hydrogen ingress into the matrix and the development of structural defects in the bulk are negligible, and the progressing corrosion mainly influences the surface. Since the associated intensity I_2 lies in the range of the intensity $I_{d_{mean}}$ estimated by the mass change of the alloy (see Fig. 54), the second defect component τ_2 is expected to originate from annihilation in the developing corrosion product layer and in new formed structural defects at the interface between corrosion product layer and Mg matrix. A similar approach was used in the corrosion works of Pietrzak et al.[80–83], where a defect positron lifetime component was mainly ascribed to the positron annihilation in the corrosion product layer and partially in a defected near-surface layer. With the chemical removal of the corrosion layer, both the positron lifetime as well as the defect concentration decreased with higher thickness removed. Yang et al.[84] additionally reported defect positron lifetimes of about 550 ps after corrosion of AM60B in NaCl measured with a slow positron beam, which they ascribed to large-size vacancy clusters or voids in the corrosion product layer. The noticeable deviation between I_2 and $I_{d_{mean}}$ may especially be caused by the strong simplification of the bilayer structure whilst neglecting the dissolution of the matrix. The second defect component τ_2 increases progressively up to 2 h of in-vitro corrosion. One possible reason could be the preferential dissolution of the Mg_2Ca particles. Due to the rapid dissolution of the precipitates, voids in the size of the second phase particles presumably formed with increasingly precipitating corrosion products at the site of the particles. The excessively formed corrosion products may fill and passivate the voids. Therefore, positron annihilation occurred to a higher extend locally in the developing voids and the corrosion product formed at these sites.

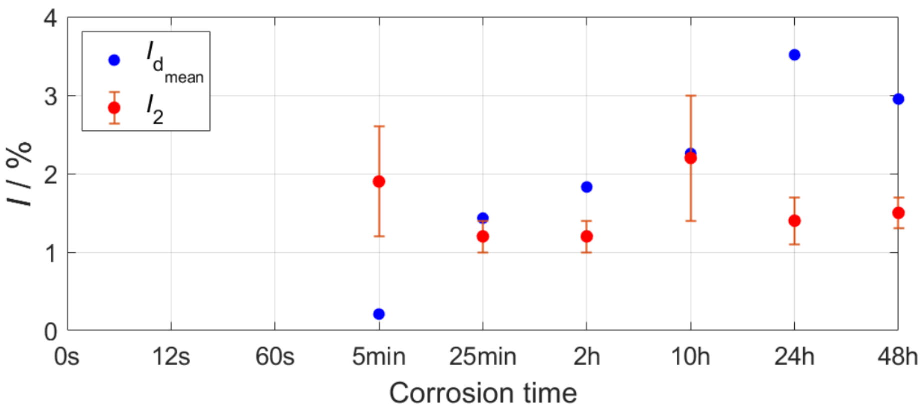

Figure 54: Positron intensity I_2 measured by PALS (see Tab. 7) and $I_{d_{mean}}$ estimated by the mass change according to eq. (70) (see Tab. 11) of the as-received Mg-alloy.

After 60 s of immersion, τ_{mean} for the **HPT-deformed Mg-alloy** increased (see Tab. 9). The two-component analysis resulted in a positron lifetime τ_1 and a defect positron lifetime τ_2. The first positron lifetime τ_1 remained approximately constant throughout the whole in-vitro corrosion within the error margin and may be thought as bulk positron lifetime, i.e. the saturated positron annihilation in the uncorroded region. Since this region is already rich in structural defects, a possible hydrogen ingress into the alloy matrix probably would not influence τ_1 significantly. The second defect positron lifetime τ_2 exhibits longer positron lifetimes, suggesting the formation of Positronium (Ps) inside the corrosion product layer and in voids formed at the corrosion product layer-matrix interface. Compared to the as-received Mg-alloy, it is expected that the second phase Mg_2Ca particles are even more finely distributed and reduced in size due to the severe plastic deformation, resulting in a more homogeneous dissolution and a reduced influence on τ_2 stemming from the formed voids.[76,77] The intensity I_2 associated with τ_2 increased to a higher extent than for the as-received Mg-alloy, indicating a more pronounced progressing formation of corrosion products on the alloy surface. The faster dissolution of the severe plastically deformed alloy may be associated with the higher density of structural defects and especially grain boundaries accompanied by a less protective surface film.

10 h - 48 h The second defect positron lifetime τ_2 and, therefore, the mean positron lifetime τ_{mean} of the **as-received Mg-alloy** decreased after 10 h of immersion (see Tab. 5). Since the voids developed from the rapid dissolution of the second phase particles are expected to be only small in size, their impact on the homogeneous dissolution of the alloy is likewise low. Thus, it is suggested that they quickly vanish in the universal corrosion front causing the decrease of τ_2. The second defect positron lifetime τ_2 then presumably is determined by the positron annihilation in a meanwhile developed corrosion product bilayer covering most of the alloy surface and the defects forming near the surface. With progressing in-vitro corrosion, τ_2 as well as τ_{mean} of the as-received Mg-alloy increase again after 48 h of immersion in SBF. Gao et al.[77] reported that due to internal stress and the second phase particles at grain boundaries, peeling off effects of the corrosion product layer may occur. Cracks and voids resulting from the disrupted corrosion product layer may additionally contribute to τ_2 increasing the defect positron lifetime.

For the **HPT-deformed Mg-alloy**, the second defect positron lifetime τ_2 decreased, whereas the mean positron lifetime τ_{mean} increased significantly up to 48 h of immersion (see Tab. 9). The strong rise in τ_{mean} suggests a massive corrosion of the alloy surface supported by the occurrence of a third measured positron lifetime τ_3. It is expected, that local deep pits have developed and the corrosion has progressed to subjacent regions of the alloy. This severe corrosion damage could enable hydrogen ingress into the alloy matrix forming MgH_2. Krystian et al.[85] as well as Grill et al.[86] reported, that the massive introduction of lattice defects by severe plastic deformation significantly increases the kinetics of the hydrogen absorption. After reduction of grain size from 2600 nm to 300 nm by ECAP, the loading of a ZK60 alloy proceeded almost twice as fast along the introduced grain boundaries compared to the diffusivity in the bulk. As prerequisite an activation process is required, where the corrosion product layer is disrupted and the resulting cracks and voids act as channels to the alloy surface. Since HPT-deformed Mg-alloy exhibits a severe mass loss after 10 h up to 48 h of immersion (see Tab. 10), it is suggested that the loose outer corrosion product layer crumbles off the alloy surface to a high extent due to peeling off effects. The severe corrosion damage leads to an increased formation of cracks in the inner dense corrosion product layer, providing quick paths for the hydrogen into the alloy. The measured second positron lifetime τ_2 could therefore be associated with the formation of cracks in the inner, more dense MgO layer and the formation of voids during the severely progressing corrosion. Since the voids probably reached deep into the alloy, hydrogen probably is ingressed into the matrix causing additional defects such as dislocations surrounding the formed MgH_2. Between 10 h and 24 h, τ_2 remained approximately constant, whereas the intensity I_2 increased. Thus, the size of the voids also remained approximately constant, but occurred at a higher density. After 48 h of immersion, τ_2 decreased with a strong increase in I_2. This decrease could be a consequence of a decrease in size of the voids, whereas their density increases. The long third positron lifetime τ_3 decreased noticeably and its intensity increased up to 48 h of immersion. This lifetime component could be caused by the formation of Ps in the porous corrosion product layer or in larger voids formed inside the alloy.

Corrosion-induced structural defects A schematic representation of the developing structural defects during in-vitro corrosion in SBF is shown in Fig. 55. Positrons may annihilate in the developing porous corrosion product layer, which may exhibit cracks with progressing corrosion time. Near the surface, positrons annihilate in a defect layer, which may exhibit smaller and larger voids. Additionally, after surface activation and/or peeling off effects, hydrogen may diffuse into the alloy matrix forming MgH_2 or remains in near-surface regions. Surrounding the MgH_2, defects, such as dislocations, accumulate influencing the positron lifetime. Positronium (Ps) may be formed in the porous corrosion product layer or in voids inside the defect layer region. The corrosion rate is highly dependent on the structural defects introduced by the severe plastic deformation. The increased grain boundary density accelerates the dissolution of the alloy matrix, whereas the corrosion product layer insufficiently protects the metal.

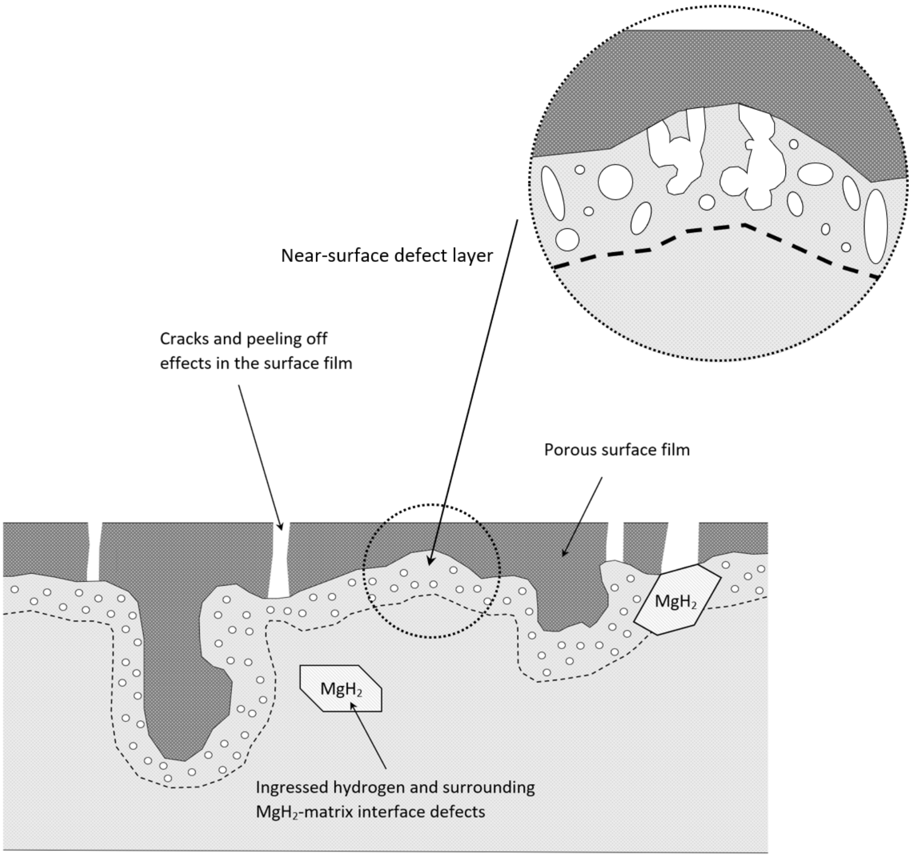

Figure 55: Developing structural defects during in-vitro corrosion in SBF.

5.2 Predominant surface reactions

Compared to the self-corrosion procedure used for the PALS measurements, the quasi-three electrode setup used to record the EIS spectra did significantly accelerate the corrosion of both alloys. This acceleration is caused by the noticeably smaller difference in electrochemical potential of the developing micro-anodes and cathodes during the microgalvanic corrosion, compared to the difference in electrochemical potential between the Pt-CE and the samples used as WE during macrogalvanic corrosion. Thus, the recorded EIS spectra cannot be linked directly with the PALS spectra for similar immersion times in SBF. The quantification of an accelerating factor is difficult, since there is no clearly visible anchor point to link the PALS developments with the EIS spectra recorded.

5.2.1 Initial immersion

Compared to the as-received Mg-alloy, the HPT-deformed Mg-alloy exhibits a more OCP (compare Fig. 36 and 46), indicating a more pronounced oxide layer already formed on the HPT-deformed Mg-alloy prior to immersion as similarly found for ECAP-deformed pure Mg in NaCl by Song et al[79]. Since severe plastic deformation increases the density of structural defects and grain boundaries near the surface, the nucleation and growth of an oxide layer is enhanced in air. Unexpectedly, the corrosion resistance of the HPT-deformed Mg-alloy is still significantly lower than for the as-received Mg-alloy as depicted in the measured EIS spectra.

The EIS spectrum of **as-received Mg-alloy** (see Fig. 35, 10 min) exhibits the expected three distinct loops associated with the anodic and cathodic corrosion mechanisms modeled by the faradaic impedance Z_F as described e.g. by Baril et al.[26], Liu et al.[27] as well as Orazem and Tribollet[25]. At high frequencies, a capacitive loop arises, which is associated with the charge transfer resistance of reaction (3) and (4), accompanied by interfacial surface layer effects. The charge transfer loop is followed by a second capacitive loop, which is associated with the finite-length diffusion of Mg^{2+} through the formed porous $Mg(OH)_2$ surface layer. At low frequencies, an inductive loop occurs, which is associated with the anodic dissolution of the alloy, involving Mg^+ as an adsorbed intermediate in the two step dissolution reaction (see eq. 3 and 4).

The form of the EIS spectrum measured for the **HPT-deformed Mg-alloy** (see Fig. 45, 10 min) differs significantly in terms of shape and size compared to the as-received Mg-alloy. The charge transfer loop at high frequencies is barely pronounced, underlining the lack of protection from the oxide layer exposing a large area of the alloy surface to the solution. The diffusional loop at medium frequencies as well as the inductive loop at low frequencies are comparably more distinct and pronounced. The increased size of the inductive loop suggests an enlarged free area at the surface, which may result from a disrupted and unstable oxide layer.[18,26,79] Since the underlying alloy surface is more exposed to the SBF, high dissolution activity is expected to set in especially at structural defects and at grain boundaries, which occur at a high density. The accompanied formation of adsorbed intermediate Mg^+ during corrosion is followed either by the chemical reaction giving rise for the NDE or by an electrochemical reaction resulting in the formation of Mg^{2+} (see Sec. 2.2.2).[26] The enhanced formation of Mg^{2+} presumably increases the diffusion in the corrosion product layer. The form of the low frequency inductive loop deviates significantly from the ideal semicircle behaviour, which may be attributed to considerable surface inhomogeneities already occurring after the initial immersion.

5.2.2 Progressing corrosion in SBF

10 min - 4 h The increase in size of the charge transfer and diffusional capacitive loops as well as of the low frequency inductive loop after the initial immersion up to 4 h of in-vitro corrosion of the **as-received Mg-alloy** (see Fig. 35, 10 min - 4 h) suggest the growth of corrosion products spreading over the alloy surface, thereby varying the film-free active areas.[26,64] The rapidly forming corrosion product bilayer, mainly consisting of MgO and $Mg(OH)_2$, effectively increases the protection of the underlying alloy surface, which is underlined by the anodic shift of the OCP and the increasing corrosion resistance (see Fig. 36). The transition between the charge transfer and the diffusional loop tends to merge, which may be attributed to precipitating HA above a certain threshold of Ca^+ concentration at local corrosion sites. The precipitated HA presumably is incorporated into the corrosion product bilayer adjacent to the alloy surface or dissolve immediately for shorter immersion times as similarly found for $MgAl_2(SO_4)_4 \cdot {}_2H_2O$ precipitates in AZ91 immersed in Na_2SO_4 by Chen et al.[87]. Brady et al.[56] reported, that $MgCO_3$ may as well be incorporated into the $Mg(OH)_2$ layer. Additionally, with increasing in-vitro corrosion, the charge transfer loop flattens, which may be attributed to local inhomogeneities in the alloy surface. These local inhomogeneities are associated with the incorporated particles as well as the precipitation and growth of the $Mg(OH)_2$ layer setting in mainly at local sites.[28,61]

Compared to the as-received Mg-alloy, the corrosion resistance for the **HPT-deformed Mg-alloy** increased significantly slower and to a less extent (see Fig. 45, 10 min - 4 h). The charge transfer loop is still weakly pronounced indicating that, even though the dissolution activity may be significantly higher due to the higher density of grain boundaries and structural defects near the alloy surface, the excessively formed corrosion products do not increase the protectiveness of the surface bilayer effectively. This is supported by an only small shift in OCP (see Fig. 46). Song et al.[79] argued, that the faster formed porous $Mg(OH)_2$ layer does not prevent the alloy matrix from the electrolyte and its corrosive ions. The higher dissolution activity due to the induced structural defects by severe plastic deformation leads to an extensive hydrogen formation once the water reaches the alloy surface. The largely formed hydrogen presumably cause cracks, disruptions, and delamination in the $Mg(OH)_2$ layer, providing channels for the electrolyte increasing the film-free area and, thus, accelerating or at least maintaining a high dissolution of the underlying alloy. Similar to the as-received Mg-alloy, HA and $MgCO_3$ are probably incorporated to a high extent into the corrosion product layer.

6 h - 24 h The size of the charge transfer, diffusional and inductive loop further increased for the **as-received Mg-alloy** up to 6 h of immersion (see Fig. 35, 6 h), whereas the OCP (see Fig. 36) remained approximately constant after 4 h with an increasing corrosion resistance. After 8 h of immersion, the size of the charge transfer loop started to decrease, whereas the diffusional and inductive loop significantly increased up to 24 h of immersion, indicating the onset of local disruptions of the surface product bilayer in form of cracks and microvoids reducing the corrosion resistance. Hence, these surface layer defects presumably lead to peeled off regions exposing more film-free active area of the alloy to SBF.[27,76,79] With increasing damage and delamination in the corrosion product layers, the corrosion resistance is weakened and the anodic activity enhanced giving rise to a more enhanced localized pitting corrosion. These localized corrosion sites are expected to passivate rapidly, since the OCP tends to increase after 24 h. Thus, it is suggested that the onset of localized corrosion results in an excessive formation of corrosion products especially at these local sites. The growing corrosion product bilayer, on the one hand, increases the protectiveness of the underlying alloy surface but, on the other hand, with increasing immersion time, the bilayer is increasingly disrupted by the formation of cracks and voids especially in the protective oxide layer. At the resulting film-free areas, the dissolution activity is enhanced significantly and the corrosion resistance weakened.

For the **HPT-deformed Mg-alloy**, the corrosion resistance (see Fig. 45, 8 h) as well as the OCP (see Fig. 46), 10 min - 4 h) remained approximately constant up to 8 h of immersion. The charge transfer loop further increased slightly. Thus, the dissolution activity remains relatively high compared to the as-received Mg-alloy without visible enhancement of the protectiveness of the corrosion product layer. After 24 h of immersion, a significant rise in the charge transfer loop occurs accompanied with an increasing stability of the corrosion product layer resulting in a deceleration of the dissolution activity and an increasing corrosion resistance. The increased protectiveness of the corrosion product layer resulted in an anodic shift of the OCP and is manifested in a rapid increase of the estimated inner MgO layer thickness. A possible explanation could be, that the increased protectiveness is caused by a high amount of HA, which precipitates during severe dissolution and which spreads throughout the surface. For the HPT-deformed Mg-alloy, the formed corrosion product layer is assumed to be more compact compared to the locally formed HA precipitates in and near corrosion pits on the as-received Mg-alloy.[22,27,77,88] The faster and more homogeneous corrosion of the HPT-deformed Mg-alloy significantly increases the pH as well as the Ca^{2+} concentration in the surrounding solution, resulting in an enhanced formation of HA covering most of the surface. With increasing corrosion time, the increasing compactness of the formed corrosion product layer may reduce peeling off as well as pitting regions on the surface. The decreasing disruptions of the surface bilayer probably leads to the substantially enhanced passivation of the underlying alloy surface.[22,77,88] The reduced dissolution of the severe plastic deformed alloy surface reduces the finite-length diffusion of Mg^{2+} in the growing $Mg(OH)_2$ layer.

29.5/30 h - 48 h After 29.5 h of immersion, an additional distinct capacitive loop emerged in the spectrum of the **as-received Mg-alloy** (see Fig. 35, 29.5 h) at very high frequencies, which is associated with growing loose porous $Mg(OH)_2$ layer. Since the corrosion resistance tends to further decrease and the low frequency inductive loop increases significantly in size, it is expected that the localized corrosion resulting from the progressing disruption of the surface film and rapid passivating is further enhanced with immersion time in SBF.[79] Accompanied with the higher dissolution activity of the alloy surface at film-free areas, the corrosion product film further grows as indicated by the increase in size of the third capacitive loop at very high frequencies and the further anodic shift of OCP after 48 h of in-vitro corrosion (see Fig. 36). The charge transfer loop further flattens with increasing immersion time, which may result from the increasing surface inhomogeneities.

After 30 h of immersion, the local corrosion of the **HPT-deformed Mg-alloy** (see Fig. 45, 30 h) further reduced, which is associated with the decreasing inductive loop and the growing HA layer. The corrosion resistance further increased, which is accompanied by an anodic shift of the OCP (see Fig. 46). After 48 h of immersion, the corrosion resistance increased rapidly, which is accompanied by the largest shift of the OCP. Since the progressively growing corrosion product layer has hardly any visible influence on the stability and permeability during the first hours of immersion, it can be assumed that the disrupted corrosion product layer lacks in stability and delaminates partially off the surface. The corrosion product layer may exhibit a high porosity, since the defect positron lifetime τ_2 (see Fig. 9) ascribed to the corrosion product layer is significantly longer than for the as-received Mg-alloy. With increasing immersion time, the compactness of the corrosion product bilayer is enhanced by the formation of a more stable HA layer, which presumably covers the whole surface and buffering the pH adjacent to the alloy surface.[27] Since the more stable HA layer probably decreases the susceptibility for pitting corrosion and disruptions in the corrosion product layer, the corrosion resistance significantly increases, thereby reducing the dissolution activity.

5.2.3 Contributions to the corrosion resistance and development of the corrosion product bilayer

The estimated zero-frequency resistance R_{ZF} (see Fig. 42) at the corrosion potential obtained by EC1 increased significantly with immersion time and is predominantly determined by R_C associated with the cathodic corrosion behaviour. The highest contributions to R_{ZF} stems from the charge transfer resistance associated with the anodic dissolution reactions and from the diffusion of Mg^{2+} through the porous $Mg(OH)_2$ layer. Thus, the corrosion rate of the **as-received Mg-alloy** is limited by the growing corrosion product bilayer protecting the alloy surface. As the peeling off effects set in, the contribution from the charge transfer resistance decreased, which accelerates the dissolution activity and enhances the diffusion in the corrosion product bilayer, thereby reducing the diffusion contribution to the corrosion resistance. The corrosion resistance after 24 h of immersion is determined under mixed control, since R_A and R_C are comparable.[27] The onset of localized corrosion reduces the surface layer capacity C_l, which is associated with decreasing surface layer thicknesses d_{MgO} and $d_{Mg(OH)_2}$, and increases the double layer capacity C_{dl}, which is associated with a higher fraction of adsorbed intermediates on the alloy surface (see Fig. 43). The scale of the estimated double layer capacity is comparable to the fitted found by Liu et al.[27] for a Mg1 wt%Ca alloy immersed. They determined a progressively decreasing double layer capacitance C_{dl} of $10.8\,\mu F\,cm^{-2}$ down to $1.49\,\mu F\,cm^{-2}$ for comparable immersion times. With increasing immersion time, C_l further increases due to the growth of the corrosion product bilayer, whereby C_{dl} is further increased. Thus, the progressing growth of the surface bilayer is indeed accompanied by a larger fraction of voids and cracks in the MgO layer, increasing the dissolution activity and reducing the corrosion resistance. The contribution of the charge transfer is significantly lower and the diffusion enhanced. The scale of the estimated inner MgO as well as the outer $Mg(OH)_2$ layer are comparable to the calculated thicknesses found by Gomes et al.[64] for pure Mg immersed in Na_2SO_4. They determined a slightly increasing MgO surface layer with a thickness of 5.4 nm up to approximately 7 nm and a decreasing total corrosion product layer with a thickness of 29 nm down to approximately 21 nm for comparable immersion times (see Fig. 14).

Compared to the as-received Mg-alloy, the highest contribution to R_{ZF} (see Fig. 51) obtained with EC1 for the **HPT-deformed Mg-alloy** originates from the preexisting MgO layer and the high fraction of adsorbed intermediates for short immersion times. The contribution from the charge transfer resistance and the diffusion resistance is comparably small resulting in a low corrosion resistance. The corrosion resistance after the initial immersion is determined under mixed control, since the resistance associated with the adsorbed intermediates plays an essential role and the oxide layer is more defined than for the as-received Mg-alloy. With increasing immersion time, the charge transfer resistance contribution increases progressively, whereas the contribution from the surface product bilayer decreases. This underlines the disturbance of the protective film resulting from the high dissolution activity, which is associated with the significantly increasing double layer capacity C_{dl} and the decreasing estimated layer thicknesses d_{MgO} and $d_{Mg(OH)_2}$ (see Fig. 53). After 24 h, the charge transfer resistance contribution increased rapidly and the corrosion resistance is predominantly determined by R_C associated with the cathodic corrosion behaviour. The corrosion resistance increases in the later stages of immersion, which decelerates the dissolution activity resulting in a more stable corrosion product bilayer. The decreasing disruption and delamination decrease the corrosion product capacity C_l as well as C_{dl}, which is associated with an increased surface film thickness d_{MgO} and a reduced fraction of adsorbed intermediate Mg^{2+} on the alloy surface.

Unfortunately, there was no visible change in the EIS spectra neither for the extruded nor the HPT-deformed Mg-alloy, which could clearly be ascribed to the diffusion of hydrogen into the alloy matrix. Thus, even though the diffusion of hydrogen into the alloy is activated by the permeable and unstable corrosion product layer and the higher dissolution activity, it is still a minor corrosion mechanism.

6 Conclusion

The effects of grain refinement on the degradation of a bioresorbable MgCaZn alloy (ZX00) in Simulated Body Fluid was studied by Positron Annihilation Lifetime and Electrochemical Impedance Spectroscopy. The following main conclusions were drawn from the obtained results:

I The **as-received Mg-alloy** exhibited a fine grain structure with small, finely distributed Mg_2Ca particles. During the first hours of immersion in SBF, this as-received Mg-alloy shows a high corrosion resistance resulting in hardly any corrosion damage at the surface. With increasing immersion time, the second phase particles preferentially dissolved, which left behind voids in the size of the dissolved particles. The formed voids at the sites of the particles are presumably filled with precipitated corrosion products before quickly vanishing in the homogeneous corrosion front. The high corrosion resistance in the early stages of immersion is associated with a more stable corrosion product bilayer, which efficiently protected the Mg-alloy from dissolving. In the later stages of corrosion, the corrosion product bilayer, covering the whole surface, was disrupted and peeled off. The increase in film-free area on the Mg-alloy noticeably enhanced the anodic dissolution activity in local areas and thereby reduced the corrosion resistance.

II **HPT-deformation of the as-received Mg-alloy** resulted in a grain refinement with the typical elongated grains. The reduced grain size accompanied by an increased number density of grain boundaries highly weakened the corrosion resistance. Both positron annihilation and impedance spectroscopy yield evidence for a much higher corrosion damage compared to the as-received Mg-alloy. During the first hours of immersion, corrosion preferentially occured at the homogeneous distributed second phase particles and in regions near grain boundaries. This preferential dissolution resulted in a highly porous corrosion product bilayer and voids formed at the corrosion product-matrix interface. With progressing corrosion in SBF, local deep pits developed and the corrosion progressed to subjacent regions in the alloy. The corrosion product bilayer increasingly exhibited cracks/voids and peeled off regions, which presumably acted along with the severe corrosion pits as quick paths for hydrogen to diffuse into the alloy. The ingressed hydrogen probably gave rise to extended MgH_2-matrix interface defects. The weakened corrosion resistance after HPT-deformation was associated with an unstable and permeable corrosion product bilayer. Even though the severe plastically deformed Mg-alloy exhibited a more pronounced oxide layer formed on air than the as-received Mg-alloy, the higher density of grain boundaries and structural defects enhanced the dissolution activity of the alloy resulting in cracks, disruptions, and peeling off regions in the corrosion product bilayer. With progressing corrosion in SBF, the precipitation and growth of a hydroxyapatite (HA) layer covering the surface was more favorable due to the increasing pH and Ca^{2+} concentration in the adjacent SBF. The more compact and stable HA layer presumably reduced peeling off effects and passivated susceptible regions on the alloy surface, thereby increasing the corrosion resistance and slowing down the dissolution activity in the latter stages of in-vitro corrosion.

Combining the complementary techniques of Positron Annihilation and Impedance Spectroscopy has proven to be very powerful for the investigation of the corrosion performance of Mg-based alloys. Insights in the progressing defect structure and the predominate surface reactions during corrosion could provide versatile tools in the development of tailored bioresorbable Mg-based implants.

References

[1] G. Manivasagam and S. Suwas. Biodegradable Mg and Mg based alloys for biomedical implants. *Mater. Sci. Technol.*, **30** (2014) 515. doi:10.1179/1743284713Y.0000000500.

[2] P. Holweg, L. Berger, M. Cihova, N. Donohue, B. Clement, U. Schwarze, N. G. Sommer, G. Hohenberger, J. J. van den Beucken, F. Seibert, A. Leithner, J. F. Löffler and A.-M. Weinberg. A lean magnesium–zinc–calcium alloy ZX00 used for bone fracture stabilization in a large growing-animal model. *Acta Biomater.*, **113** (2020) 646. doi:10.1016/j.actbio.2020.06.013.

[3] H. Ibrahim, A. D. Klarner, B. Poorganji, D. Dean, A. A. Luo and M. Elahinia. Microstructural, mechanical and corrosion characteristics of heat-treated Mg-1.2Zn-0.5Ca (wt%) alloy for use as resorbable bone fixation material. *J. Mech. Behav. Biomed. Mater.*, **69** (2017) 203. doi:10.1016/j.jmbbm.2017.01.005.

[4] S. Lovald and S. M. Kurtz. Applications of Polyetheretherketone in Trauma, Arthroscopy, and Cranial Defect Repair. In *PEEK Biomaterials Handbook*, Plastics Design Library, chapter 15, pages 243–260. William Andrew Publishing, Oxford (2012). doi:10.1016/B978-1-4377-4463-7.10015-6.

[5] C. S. Manolagas and R. L. Jilka. Bone Marrow, Cytokines, and Bone Remodeling — Emerging Insights into the Pathophysiology of Osteoporosis. *N. Engl. J. Med.*, **332** (1995) 305. doi:10.1056/NEJM199502023320506.

[6] H. Zhang, C. G. Lewis, M. S. Aronow and G. A. Gronowicz. The effects of patient age on human osteoblasts' response to Ti–6Al–4V implants in vitro. *J. Orthop. Res.*, **22** (2004) 30. doi:10.1016/S0736-0266(03)00155-4.

[7] P. Augat, U. Simon, A. Liedert and L. Claes. Mechanics and Mechano-Biology of Fracture Healing in Normal and Osteoporotic Bone. *Osteoporosis international*, **16** (2005) 36. doi:10.1007/s00198-004-1728-9.

[8] Z. Khatoon, C. D. McTiernan, E. J. Suuronen, T.-F. Mah and E. I. Alarcon. Bacterial biofilm formation on implantable devices and approaches to its treatment and prevention. *Heliyon*, **4** (2018) e01067. doi:10.1016/j.heliyon.2018.e01067.

[9] N. Ikeo, M. Nishioka and T. Mukai. Fabrication of biodegradable materials with high strength by grain refinement of Mg–0.3at.% Ca alloys. *Mater.Lett.*, **223** (2018) 65. doi:10.1016/j.matlet.2018.03.188.

[10] N. Li and Y. Zheng. Novel Magnesium Alloys Developed for Biomedical Application: A Review. *J. Mater. Sci. Technol.*, **29** (2013) 489. doi:10.1016/j.jmst.2013.02.005.

[11] N. Grün, P. Holweg, S. Tangl, J. Eichler, L. Berger, J. van den Beucken, J. Löffler, T. Klestil and A. Weinberg. Comparison of a resorbable magnesium implant in small and large growing-animal models. *Acta Biomater.*, **78** (2018) 378. doi:10.1016/j.actbio.2018.07.044.

[12] J. Vormann. Magnesium: nutrition and metabolism. *Mol. Aspects Med.*, **24** (2003) 27. doi:10.1016/S0098-2997(02)00089-4.

[13] H. Zreiqat, C. R. Howlett, A. Zannettino, P. Evans, G. Schulze-Tanzil, C. Knabe and M. Shakibaei. Mechanisms of magnesium-stimulated adhesion of osteoblastic cells to commonly used orthopaedic implants. *J. Biomed. Mater. Res.*, **62** (2002) 175. doi:10.1002/jbm.10270.

[14] M. Cihova, E. Martinelli, P. Schmutz, A. Myrissa, R. Schäublin, A. Weinberg, P. Uggowitzer and J. Löffler. The role of zinc in the biocorrosion behavior of resorbable Mg–Zn–Ca alloys. *Acta Biomater.*, **100** (2019) 398. doi:10.1016/j.actbio.2019.09.021.

[15] W. Schmickler and E. Santos. *Interfacial Electrochemistry.* Springer Berlin Heidelberg, Berlin, Heidelberg (2010). doi:10.1007/978-3-642-04937-8.

[16] C. H. Hamann and W. Vielstich. *Elektrochemie 4. Auflage.* Wiley VCH Verlag GmbH, Weinheim (2005).

[17] A. A. Isse and A. Gennaro. Absolute Potential of the Standard Hydrogen Electrode and the Problem of Interconversion of Potentials in Different Solvents. *J. Phys. Chem. B*, **114** (2010) 7894. doi:10.1021/jp100402x.

[18] G. Song. Corrosion electrochemistry of magnesium (Mg) and its alloys. In *Corrosion of Magnesium Alloys*, Woodhead Publishing Series in Metals and Surface Engineering, pages 3 – 65. Woodhead Publishing (2011). doi:10.1533/9780857091413.1.3.

[19] G. Song. Preface. In *Corrosion of Magnesium Alloys*, Woodhead Publishing Series in Metals and Surface Engineering, pages xix – xxiii. Woodhead Publishing (2011). doi:10.1016/B978-1-84569-708-2.50021-4.

[20] G. Song and A. Atrens. Understanding Magnesium Corrosion—A Framework for Improved Alloy Performance. *Adv. Eng. Mater.*, **5** (2003) 837. doi:10.1002/adem.200310405.

[21] G. Song and A. Atrens. Corrosion Mechanisms of Magnesium Alloys. *Adv. Eng. Mater.*, **1** (1999) 11. doi:10.1002/(SICI)1527-2648(199909)1:1<11::AID-ADEM11>3.0.CO;2-N.

[22] J.-Y. Lee, G. Han, Y.-C. Kim, J. Byun, J. i. Jang, H.-K. Seok and S.-J. Yang. Effects of impurities on the biodegradation behavior of pure magnesium. *Met. Mater. Int.*, **15** (2009) 955. doi:10.1007/s12540-009-0955-1.

[23] M. E. Orazem and B. Tribollet. *Front Matter: A Brief Introduction to Impedance Spectroscopy*, pages i–xlvii. John Wiley & Sons, Ltd (2017). doi:10.1002/9781119363682.fmatter.

[24] M. E. Orazem and B. Tribollet. *Equivalent Circuit Analogs*, chapter 9, pages 191–206. John Wiley & Sons, Ltd (2017). doi:10.1002/9781119363682.ch9.

[25] M. Orazem, N. Pebere and B. Tribollet. *Kinetic Models*, chapter 10, pages 163–181. John Wiley Sons, Ltd (2008). doi:10.1002/9780470381588.ch10.

[26] G. Baril, G. Galicia, C. Deslouis, N. Pébère, B. Tribollet and V. Vivier. An Impedance Investigation of the Mechanism of Pure Magnesium Corrosion in Sodium Sulfate Solutions. *J. Electrochem. Soc.*, **154** (2007) C108. doi:10.1149/1.2401056.

[27] Y. Liu, M. Curioni and Z. Liu. Correlation between electrochemical impedance measurements and corrosion rates of Mg-1Ca alloy in simulated body fluid. *Electrochim. Acta*, **264** (2018) 101. doi:10.1016/j.electacta.2018.01.121.

[28] A. King, N. Birbilis and J. Scully. Accurate Electrochemical Measurement of Magnesium Corrosion Rates; a Combined Impedance, Mass-Loss and Hydrogen Collection Study. *Electrochim. Acta*, **121** (2014) 394. doi:10.1016/j.electacta.2013.12.124.

[29] M. Orazem, N. Pebere and B. Tribollet. *Diffusion Impedance*, chapter 11, pages 183–210. John Wiley Sons, Ltd (2008). doi:10.1002/9780470381588.ch11.

[30] C. Szeles and K. G. Lynn. *In digital Encyclopedia of Applied Physics*, chapter Positron-Annihilation Spectroscopy, pages 607–632. Wiley-VCH Verlag GmbH & Co. KGaA (Ed.) (2003). doi:10.1002/3527600434.eap355.

[31] P. J. Schultz and K. G. Lynn. Interaction of positron beams with surfaces, thin films, and interfaces. *Rev. Mod. Phys.*, **60** (1988) 701. doi:10.1103/RevModPhys.60.701.

[32] P. Hautojärvi and A. Vehanen. *Positrons in Solids*, chapter Introduction to Positron Annihilation, pages 1–23. Springer Berlin Heidelberg (1979). doi:10.1007/978-3-642-81316-0_1.

[33] L. Resch. *Positronium formation on thin layers and laser excitation of positronium.* Master's thesis, Graz University of Technology (2016).

[34] R. West. *Hautojärvi P. (eds) Positrons in Solids*, chapter Positron Studies of Lattice Defects in Metals, pages 89–144. Springer Berlin Heidelberg (1979). doi:10.1007/978-3-642-81316-0_3.

[35] M. Leitner. *Synthesis and Positron Annihilation Lifetime Spectroscopy of Nanoporous Platinum.* Master's thesis, Graz University of Technology (2015).

[36] G. Klinser. *Operando Studies of Charging Processes in Battery Cathodes by Magnetometry and Positron Annihilation.* Ph.D. thesis, Graz University of Technology (2019).

[37] G. Schatz and A. Weidinger. *Nukleare Festkörperphysik*, chapter Positronenvernichtung, pages 211–225. Vieweg&Teubner Verlag (1992). doi:10.1007/978-3-322-93989-0_-9.

[38] R. M. Nieminen and M. J. Manninen. *Positrons in Solids*, chapter Positrons in Imperfect Solids: Theory, pages 145–195. Springer Berlin Heidelberg (1979). doi:10.1007/978-3-642-81316-0_4.

[39] P. J. Hautojärvi, J. Johansson, A. Vehanen, J. Yli-kauppila, J. Hillairet and P. Tzanétakis. Trapping of positrons at vacancies in magnesium. *Appl. Phys. A*, **27** (1982) 49. doi:10.1007/BF01197546.

[40] L. C. Smedskjaer, M. Manninen and M. J. Fluss. An alternative interpretation of positron annihilation in dislocations. *J. Phys. F: Met. Phys.*, **10** (1980) 2237. doi:10.1088/0305-4608/10/10/019.

[41] J. del Río, C. Gómez and M. Ruano. Positron trapping mechanism in plastically deformed magnesium. *Philos. Mag.*, **92** (2012) 535. doi:10.1080/14786435.2011.622307.

[42] J. Čížek, M. Janeček, O.Srba, R. Kužel, Z. Barnovska, I. Procházka and S. Dobatkin. Evolution of defects in copper deformed by high-pressure torsion. *Acta Mater.*, **59** (2011) 2322. doi:10.1016/j.actamat.2010.12.028.

[43] J. Čížek, I. Procházka, B. Smola, I. Stulíková, R. Kužel, Z. Matěj, V. Cherkaska, R. Islamgaliev and O. Kulyasova. Microstructure and thermal stability of ultra fine grained Mg-based alloys prepared by high-pressure torsion. *Mater. Sci. Eng. A*, **462** (2007) 121. doi:10.1016/j.msea.2006.01.177. International Symposium on Physics of Materials, 2005.

[44] J. Čížek, I. Procházka, B. Smola, I. Stulíková, R. Kužel, Z. Matěj, V. Cherkaska, O. Kulyasova and R. Islamgaliev. Microstructure and Thermal Stability of Ultra Fine Grained Mg and Mg-Gd Alloys Prepared by High-Pressure Torsion. *Mater. Sci. Forum*, **482** (2005) 183. doi:10.4028/www.scientific.net/MSF.482.183.

[45] J. Dryzek, E. Dryzek, T. Suzuki and R. Yu. Subsurface Zone in Pure Magnesium Studied by Positron Lifetime Spectroscopy. *Tribol. Lett.*, **20** (2005) 91. doi:10.1007/s11249-005-7796-y.

[46] J. M. C. Robles, E. Ogando and F. Plazaola. Positron lifetime calculation for the elements of the periodic table. *J. Phys.: Condens. Matter*, **19** (2007) 176222. doi:10.1088/0953-8984/19/17/176222.

[47] C. Macchi, C. Maurizio, R. Checchetto, S. Mariazzi, L. Ravelli, W. Egger, P. Mengucci, N. Bazzanella, A. Miotello, A. Somoza and R. Brusa. Niobium aggregation and vacancylike defect evolution in nanostructured Nb-doped Mg: Their role in the kinetics of the hydride-to-metal phase transformation. *Phys. Rev. B*, **85** (2012) 214117. doi:10.1103/PhysRevB.85.214117.

[48] M. J. Puska and R. M. Nieminen. Theory of positrons in solids and on solid surfaces. *Rev. Mod. Phys.*, **66** (1994) 841. doi:10.1103/revmodphys.66.841.

[49] J. Dryzek. Positron annihilation studies of recrystallization in the subsurface zone induced by friction in magnesium—effect of the inhomogeneity on measured positron annihilation characteristics. *Appl. Phys. A*, **114** (2014) 465. doi:10.1007/s00339-013-7667-6.

[50] E. A. Badawi, M. Abdel-Rahman and S. Mahmoud. Investigation of defects (migration and formation) in metals by positron annihilation lifetime. *Appl. Surf. Sci.*, **149** (1999) 211. doi:10.1016/S0169-4332(99)00203-2.

[51] A. Poznak, D. Freiberg and P. Sanders. Chapter 10 - Automotive Wrought Aluminium Alloys. In R. N. Lumley, editor, *Fundamentals of Aluminium Metallurgy*, Woodhead Publishing Series in Metals and Surface Engineering, pages 333 – 386. Woodhead Publishing (2018). doi:10.1016/B978-0-08-102063-0.00010-2.

[52] W. Puff. Ausgewählte Themen der Technischen Physik: Festkörperspektroskopie mit Positronen. Skript zur Vorlesung (2013/2014).

[53] P. Kirkegaard, J. Olsen, M. Eldrup and N. Pedersen. *PALSfit: A computer program for analysing positron lifetime spectra*. Number 1652(EN) in Denmark. Forskningscenter Risoe. Risoe-R. Danmarks Tekniske Universitet, Risø Nationallaboratoriet for Bæredygtig Energi (2009).

[54] O. Poupard, A. Aït-Mokhtar and P. Dumargue. Impedance spectroscopy in reinforced concrete: Procedure for monitoring steel corrosion Part I Development of the experimental device. *J. Mater. Sci.*, **38** (2003) 2845. doi:10.1023/A:1024428317968.

[55] D. A. Kramer. *Magnesium Compounds. In Kirk-Othmer Encyclopedia of Chemical Technology, (Ed.).* American Cancer Society (2004). doi:10.1002/0471238961.1301071410010311.a01.pub3.

[56] M. Brady, G. Rother, L. Anovitz, K. Littrell, K. Unocic, H. Elsentriecy, G. Song, J. Thomson, N. Gallego and B. Davis. Film Breakdown and Nano-Porous $Mg(OH)_2$ Formation from Corrosion of Magnesium Alloys in Salt Solutions. *J. Electrochem. Soc.*, **162** (2015) C140. doi:10.1149/2.0171504jes.

[57] B. A. Boukamp. A Linear Kronig-Kramers Transform Test for Immittance Data Validation. *J. Electrochem. Soc.*, **142** (1995) 1885. doi:10.1149/1.2044210.

[58] M. Orazem, N. Pébère and B. Tribollet. Enhanced Graphical Representation of Electrochemical Impedance Data. *J. Electrochem. Soc.*, **153** (2006) B129. doi:10.1149/1.2168377.

[59] D. Klotz. Negative capacitance or inductive loop? – A general assessment of a common low frequency impedance feature. *Electrochem. Commun.*, **98** (2019) 58. doi:10.1016/j.elecom.2018.11.017.

[60] N. Kirkland, N. Birbilis and M. Staiger. Assessing the corrosion of biodegradable magnesium implants: A critical review of current methodologies and their limitations. *Acta Biomater.*, **8** (2012) 925. doi:10.1016/j.actbio.2011.11.014.

[61] M. E. Orazem and B. Tribollet. *Constant-Phase Elements*, chapter 14, pages 395–419. John Wiley Sons, Ltd (2017). doi:10.1002/9781119363682.ch14.

[62] G. J. Brug, A. L. G. van den Eeden, M. Sluyters-Rehbach and J. Sluyters. The analysis of electrode impedances complicated by the presence of a constant phase element. *J. Electroanal. Chem. Interfacial Electrochem.*, **176** (1984) 275. doi:10.1016/S0022-0728(84)80324-1.

[63] N. Damak, A. Kallel and Z. Fakhfakh. Space charge characterization of MgO by coupling cavity resonator and mirror method. *Ann. Chim. Sci. Mat.*, **23** (1998) 255. doi:10.1016/S0151-9107(98)80068-8.

[64] M. P. Gomes, I. Costa, N. Pébère, J. L. Rossi, B. Tribollet and V. Vivier. On the corrosion mechanism of Mg investigated by electrochemical impedance spectroscopy. *Electrochim. Acta*, **306** (2019) 61. doi:10.1016/j.electacta.2019.03.080.

[65] J. Gasc, F. Brunet, N. Bagdassar and V. Morales-Florez. Electrical conductivity of polycrystalline $Mg(OH)_2$ at 2 GPa: Effect of grain boundary hydration-dehydration. *Phys. Chem. Miner.*, **38** (2011) 543. doi:10.1007/s00269-011-0426-3.

[66] P. Agarwal, M. Orazem and L. H. Garcia-Rubio. Measurement Models for Electrochemical Impedance Spectroscopy. *J. Electrochem. Soc.*, **139** (1992) 1917. doi:10.1149/1.2069522.

[67] P. E. Brunner. et al. to be published (2020/2021).

[68] S. Johnston, Z. Shi, C. Hoe, P. Uggowitzer, M. Cihova, J. Löffler, M. Dargusch and A. Atrens. The influence of two common sterilization techniques on the corrosion of Mg and its alloys for biomedical applications. *J. Biomed. Mater. Res. B*, **106** (2017) 1907. doi:10.1002/jbm.b.34004.

[69] A. Südholz, N. Kirkland, R. Buchheit and N. Birbilis. Electrochemical Properties of Intermetallic Phases and Common Impurity Elements in Magnesium Alloys. *Electrochem. Solid-State Lett.*, **14** (2011) C5. doi:10.1149/1.3523229.

[70] J. Nie and B. Muddle. Precipitation hardening of Mg-Ca(-Zn) alloys. *Scr. Mater.*, **37** (1997) 1475. doi:10.1016/S1359-6462(97)00294-7.

[71] Y. Ortega and J. del Rio. Study of Mg–Ca alloys by positron annihilation technique. *Scr. Mater.*, **52** (2005) 181. doi:10.1016/j.scriptamat.2004.09.033.

[72] R. Würschum, L. Resch and G. Klinser. Diffusion-reaction model for positron trapping and annihilation at spherical extended defects and in precipitate-matrix composites. *Phys. Rev. B*, **97** (2018) 224108. doi:10.1103/PhysRevB.97.224108.

[73] B. Oberdorfer and R. Würschum. Positron trapping model for point defects and grain boundaries in polycrystalline materials. *Phys. Rev. B*, **79** (2009) 184103. doi:10.1103/PhysRevB.79.184103.

[74] P. Minárik, J. Veselý, J. Čížek, M. Zemková, T. Vlasák, T. Krajňák, J. Kubásek, R. Král, D. Hofman and J. Stráská. Effect of secondary phase particles on thermal stability of ultra-fine grained Mg-4Y-3RE alloy prepared by equal channel angular pressing. *Mater. Charact.*, **140** (2018) 207. doi:10.1016/j.matchar.2018.04.006.

[75] G. Han, J.-Y. Lee, Y.-C. Kim, J. H. Park, D.-I. Kim, H.-S. Han, S.-J. Yang and H.-K. Seok. Preferred crystallographic pitting corrosion of pure magnesium in Hanks' solution. *Corros. Sci.*, **63** (2012) 316. doi:10.1016/j.corsci.2012.06.011.

[76] C. Zhang, S. Zhu, L. Wang, R. Guo, G. Yue and S. Guan. Microstructures and degradation mechanism in simulated body fluid of biomedical Mg–Zn–Ca alloy processed by high pressure torsion. *Mater. Des.*, **96** (2016) 54. doi:10.1016/j.matdes.2016.01.072.

[77] J. Gao, S. Guan, Z. Ren, Y. Sun, S. Zhu and B. Wang. Homogeneous corrosion of high pressure torsion treated Mg–Zn–Ca alloy in simulated body fluid. *Mater. Lett.*, **65** (2011) 691. doi:10.1016/j.matlet.2010.11.015.

[78] K. A. Unocic, H. H. Elsentriecy, M. P. Brady, H. M. Meyer, G. Song, M. Fayek, R. A. Meisner and B. Davis. Transmission Electron Microscopy Study of Aqueous Film Formation and Evolution on Magnesium Alloys. *J. Electrochem. Soc.*, **161** (2014) C302. doi:10.1149/2.024406jes.

[79] D. Song, A. Ma, J. Jiang, P. Lin, D. Yang and J. Fan. Corrosion behavior of equal-channel-angular-pressed pure magnesium in NaCl aqueous solution. *Corros. Sci.*, **52** (2010) 481. doi:10.1016/j.corsci.2009.10.004.

[80] R. Pietrzak and R. Szatanik. Effect of magnetic field on the corrosion of iron and St20 steel as studied by positron annihilation. *Phys. Status Solidi B*, **247** (2010) 1822. doi:10.1002/pssb.200945124.

[81] R. Pietrzak, W. Smiatek and R. Szatanik. Positron Annihilation in Corroded Steels St20 and St3S. *Acta Phys. Pol. A*, **110** (2006) 667. doi:10.12693/APhysPolA.110.667.

[82] R. Pietrzak, R. Szatanik and M. Szuszkiewicz. Measurements of Positrons Lifetimes in Corroded Nickel. *Acta Phys. Pol. A*, **95** (1999) 647. doi:10.12693/APhysPolA.95.647.

[83] R. Pietrzak and R. Szatanik. Investigation of corrosion defects in titanium by positron annihilation. *Nukleonika*, **60** (2015) 755. doi:10.1515/nuka-2015-0136.

[84] W. Yang, Z. Zhu, J. Wang, Y. Wu, T. Zhai and G. Song. Slow positron beam study of corrosion behavior of AM60B magnesium alloy in NaCl solution. *Corros. Sci.*, **106** (2016) 271. doi:10.1016/j.corsci.2016.02.012.

[85] M. Krystian, M. Zehetbauer, H. Kropik, B. Mingler and G. Krexner. Hydrogen storage properties of bulk nanostructured ZK60 Mg alloy processed by Equal Channel Angular Pressing. *J. Alloys Compd.*, **509** (2011) 449. doi:10.1016/j.jallcom.2011.01.029. XVII International Symposium on Metastable, Amorphous and Nanostructured Materials.

[86] A. Grill, J.Horky, A. Panigrahi, G. Krexner and M. Zehetbauer. Long-term hydrogen storage in Mg and ZK60 after Severe Plastic Deformation. *Int. J. Hydrogen Energy*, **40** (2015) 17144. doi:10.1016/j.ijhydene.2015.05.145. Special issue on 1st International Conference on Hydrogen Storage, Embrittlement and Applications (Hy-SEA 2014), 26-30 October 2014, Rio de Janeiro, Brazil.

[87] J. Chen, J. Wang, E. Han, J. Dong and W. Ke. AC impedance spectroscopy study of the corrosion behavior of an AZ91 magnesium alloy in 0.1 M sodium sulfate solution. *Electrochim. Acta*, **52** (2007) 3299. doi:10.1016/j.electacta.2006.10.007.

[88] Y. Jeong and W. Kim. Enhancement of mechanical properties and corrosion resistance of Mg–Ca alloys through microstructural refinement by indirect extrusion. *Corros. Sci.*, **82** (2014) 392. doi:10.1016/j.corsci.2014.01.041.

Acknowledgement

Univ.-Prof. Dr. Roland Würschum, Institute of Materials Physics, TU Graz
for his individual supervision of this thesis and the opportunity to learn from his outstanding experience and know-how in a pleasant environment.

Dipl.-Ing. Dr.techn. Eva-Maria Steyskal, Institute of Materials Physics, TU Graz
for offering me the opportunity to take the first steps together in such an exciting research topic. I would also like to thank her for co-supervising my thesis and the scientific support she provided as well as her understanding and open-minded personality.

Dipl.-Ing. Philipp Emanuel Brunner, Institute of Materials Physics, TU Graz
for his commitment, patience and critical discussions throughout the course of this thesis. I am very grateful for his support in the laboratory and during the data analysis and interpretation, especially for the time during the quarantine.

Assoz. Prof.in Priv.-Doz.in Dr.in med. Annelie-Martina Weinberg,
Department of Orthopaedics and Traumatology, Medical University of Graz
for the provision of the alloy sample materials.

Dr. Oliver Renk, Erich Schmid Institute of Materials Science,
Austrian Academy of Science
for HPT-treatment at the ESI facilities and the rough sample preparation.

Colleagues at the Institute of Materials Physics, TU Graz
for the warm welcome and relaxed atmosphere in a great working environment at the institute. I really appreciate the open attitudes and the constructive discussions throughout the course of this thesis. I would like to especially thank Markus for his support and the great time in and out of the office.

Family and friends
for teaching me to work hard for my goals and giving me the freedom I needed, whilst still supporting me within all their possibilities. I would also like to especially thank Franziska for showing so much consideration and support during the course of my thesis, making every day special with her kind and loving personality.